Jet Charge in pp and Pb-Pb collisions measured with the ALICE experiment at the LHC

By

J Samuel Colburn

A thesis submitted to
the University of Birmingham
for the degree of
DOCTOR OF PHILOSOPHY

Nuclear Physics Research Group
School of Physics and Astronomy
College of Engineering and Physical Sciences
University of Birmingham
September 2023

UNIVERSITY OF
BIRMINGHAM

University of Birmingham Research Archive

e-theses repository

This unpublished thesis/dissertation is copyright of the author and/or third parties. The intellectual property rights of the author or third parties in respect of this work are as defined by The Copyright Designs and Patents Act 1988 or as modified by any successor legislation.

Any use made of information contained in this thesis/dissertation must be in accordance with that legislation and must be properly acknowledged. Further distribution or reproduction in any format is prohibited without the permission of the copyright holder.

© Copyright by JONATHAN SAMUEL COLBURN, 2023

All Rights Reserved

ABSTRACT

Jet charge is the momentum-weighted sum of a jet's electric charges. The value of a jet's given jet charge is influenced by the parton that initiated the jet. This influence shifts the net charge towards the charge of that progenitor parton. This property offers a way to study the energy-loss from the QGP. Generating templates for the jet charge distribution for a given progenitor parton using Monte Carlo (MC) data and then fitting these templates to real data allows jet yields to be extracted. Two different techniques were investigated for identifying the progenitor parton of the jet. The first of the techniques employs the structure of the MC data and framework. The second of these techniques selects the parton based on the constituent of the jet with the largest momentum.

The yields of jets produced from distinct types of parton have been measured in pp and Pb-Pb data at $\sqrt{s_{NN}} =$ in order to investigate the effects of the QGP on quark and gluon jets. It has been suggested that gluons will interact more strongly with the QGP when compared to quarks. Thus, gluon jets are expected to be more heavily suppressed by the QGP. The background subtraction in the Pb-Pb data was conducted using the constituent subtraction method. Suppression of gluon jets is found at medium centrality collisions (i.e. in the centrality range 40-80%); however, in the most central collisions, it is likely that the background-dominated environment prevents the jet charge distribution templates from being accurately fitted to the experimental data. In order to conclusively demonstrate gluon suppression by the QGP using measurements of the jet charge observable, a better method of handling the effects of jet charge in the most central collisions must be developed. This thesis presents the first measurements of jet charge at ALICE using Run 2 data.

DEDICATION

Dedicated to my family and teachers who have helped me grow and fostered my love for learning.

ACKNOWLEDGEMENTS

I acknowledge the fantastic work done by my supervisors, who have managed to supervise me during the COVID-19 pandemic as they had to deal with all the university's teaching system changes. Additionally, I would like to thank all the fantastic work done by the ALICE collaboration, particularly the jet physics working group, who have a fantastic grasp and were happy to help out with emails from the start to finish of my PhD.

Finally, I would like to thank my wonderful father, who was brave enough to proofread my work.

Contents

List of Figures

List of Tables

Chapter One

Introduction

1.1 Early Universe

In the beginning, the Universe was created from the Big Bang, and the initial stages of the Universe can be described as different cosmological epochs. The first of these epochs is known as the grand unification epoch. This epoch is defined by the coalescence of all four fundamental forces: the electromagnetic force, the weak nuclear force, the strong nuclear force and gravity. However, gravity is omitted from the discussion in this work due to it's insignificant effect on the subatomic scale. During this time, the universe expanded and cooled, and after $t < 10^{-36}$ seconds, the first of these forces decoupled. This force was the strong nuclear force, with the weak nuclear force and the electromagnetic force remaining coupled as the electroweak force. After $t < 10^{-32}$ seconds, the electromagnetic and the weak nuclear forces decoupled. During this time, even though the forces had decoupled, the universe was still very different from how it is now. The extreme temperature and density of the universe at this time prevented quarks from condensing into hadrons. This time is known as the quark epoch, where matter existed as a hot mixture of fundamental particles. This state of matter is known as the quark-gluon plasma (QGP). After this epoch, as the universe continued to decrease in temperature, the process of hadronic freeze-out began, causing quarks to form into hadrons, then nuclei and eventually atoms, leading to the current state of the universe.

The densities and temperatures of the quark epoch are at the limits of what is reproducible with current high-energy particle accelerators. Therefore, these accelerators are used to probe the nature of physics during this cosmological epoch by recreating the QGP. The work presented in this thesis strives to supply further insight into the nature of the QGP.

1.2 The Standard Model

The Standard Model is the current best theoretical model to describe all ordinary matter. It describes the universe in terms of fundamental particles and forces of nature. These particles fall into two overarching categories, namely, fermions and bosons.

Fermions are particles which have a half-integer spin and form the majority of the matter that is observed in everyday situations. The most common groups of fermions are quarks and leptons. There are six flavours of quarks: up, down, strange, charm, top and bottom. Similarly, there are six flavours of leptons: electrons, electron-neutrinos, muons, muon-neutrinos, taus and tau-neutrinos. These particles are separated into three generations in increasing mass, as shown in figure 1.1 [1].

The quark model, which forms the basis of the strongly interacting fermions in the Standard Model, was developed to better understand the nature of matter as the number of newly discovered particles increased. An increasing number of particles discovered suggested that these particles were not fundamental but instead composed of several sub-atomic particles. Thus, the quark model was independently proposed in 1964 by both Gell-Mann [2] and

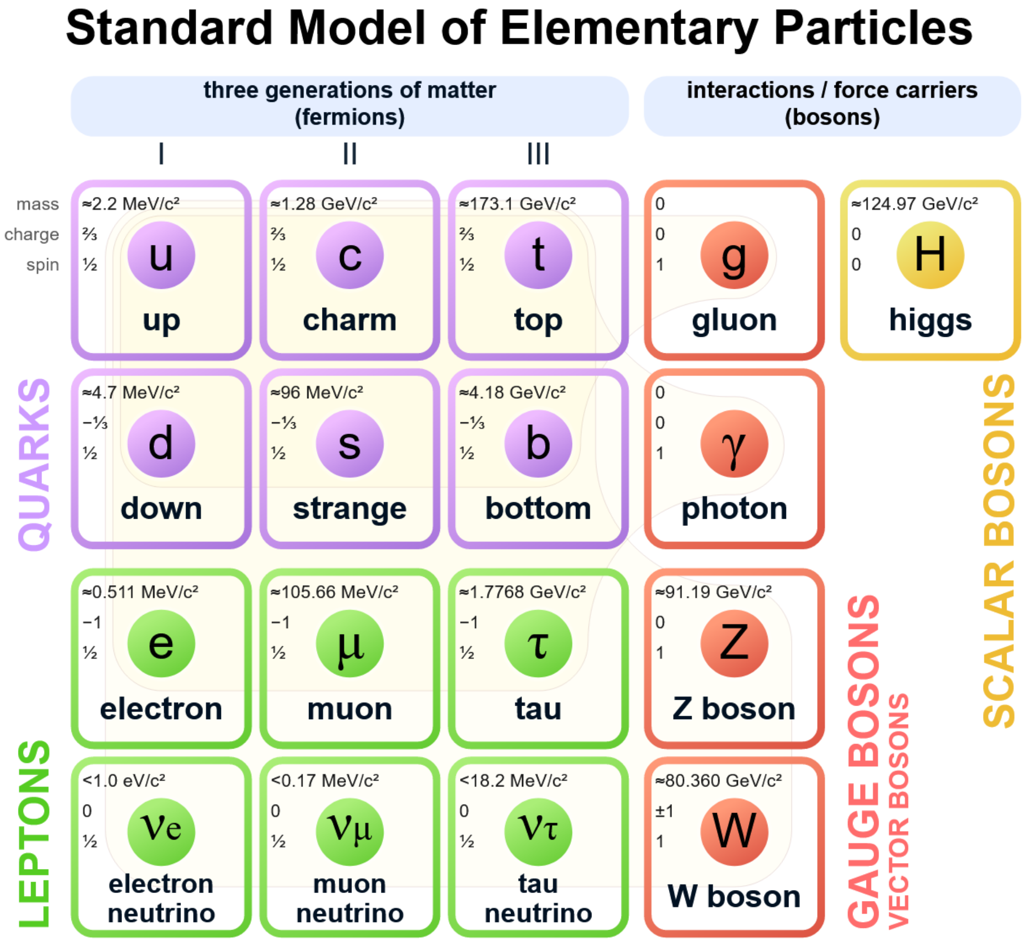

Figure 1.1: The diagram shows the particles which make up the standard model. It demonstrates how matter is split into fermionic and bosonic matter and shows the further division of fermions into three generations laid out in vertical columns. The three generations are characterised by increasing mass. Figure taken from Ref [1].

Zweig [3], proposing that these discovered particles are made up of fundamental particles known as quarks. The particles composed of these quarks are known as hadrons. These hadrons are created of either a quark - antiquark pair and known as mesons, or three quarks, and known as baryons. The different groups of particle classification are presented in figure 1.2 as a flow chart for clarity.

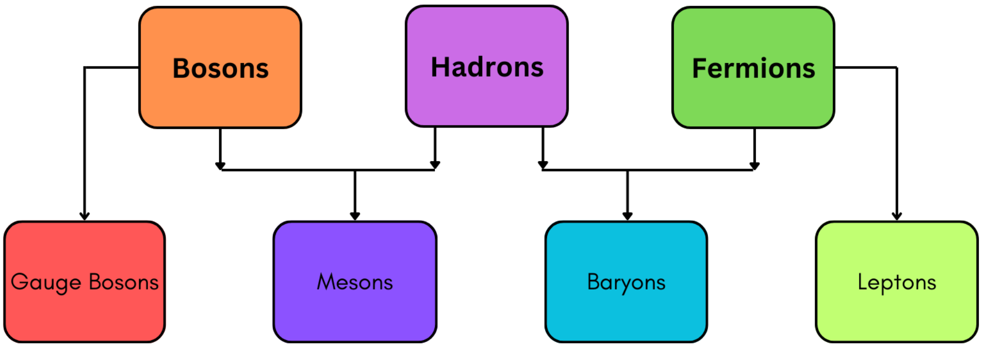

Figure 1.2: The figure shows a flow chart of the distinct groups of particle classification and how each classification relates to the broader group.

On the other hand, bosons are particles with integer spins. Bosons include the four fundamental-force carriers. Photons (γ) are the force carrier of the electromagnetic force. The $W^{\pm}$ and Z bosons are the force carriers of the weak nuclear force. Finally, gluons are the force carrier of the strong nuclear force.

The exchange of each of these force-carrying bosons between particles is what gives rise to the fundamental forces. Each of these forces has a corresponding field theory associated with it. The field theory that describes the electromagnetic force is quantum electrodynamics (QED). The weak force is described by the electroweak theory [4] [5] [6]. The strong nuclear force is described using quantum chromodynamics (QCD) [7] [8] [9]. QCD has yet to develop the same level of experimental and theoretical validation as QED. This is due to the self-interacting nature of gluons and the large coupling constant. The work presented in this thesis, as well as the broader wealth of analysis performed on the data collected by the ALICE detector as a whole, is focused on improving the validation of QCD.

The relative strengths of the fundamental forces correspond to coupling constants. Gravity is the weakest, followed by electromagnetism, the weak nuclear force and finally, the strong nuclear force. The relative strength and scales can be seen in table 1.1.

Table 1.1: The table shows the approximate relative strengths of the coupling constants for each force at the subatomic scale

Force	Coupling Constant	Range [m]	Relative Strength
Gravity	α_g	Infinite	10^{-39}
Weak	α_w	10^{-17}	10^{-6}
Electromagnetic	α	Infinite	1/137
Strong	α_s	10^{-15}	1

Each of these forces varies in how easily their manifestations are observed. The electromagnetic force is the most easily observable since it has a range that is noticeable at the macroscopic scale and thus dominates in the macroscopic world. This scale occurs because the force carrier of the electromagnetic force, the photon, has an unlimited range. This is because a real photon is massless and travels at the speed of light; it thus, does not have a finite lifetime. Conversely, the strong and weak nuclear forces have a limited range and are, thus, harder to observe.

The weak force operates on a scale of 10^{-17} m. This is due to the mass of its gauge bosons. The two bosons mediating the weak force, the $W^{\pm}$ and the Z^0 have a mass of 80.327 GeV/c^2 and 91.1876 GeV/c^2, respectively [10]. The mass of these bosons limits the effective range of the forces due to the Heisenberg uncertainty principle, as the principle states that an increased mass leads to a reduced lifetime for a virtual particle $\Delta t = \frac{\hbar}{2\Delta E}$. Thus, there is a limited range to the weak force.

The strong nuclear force is also limited in range. However, unlike the weak force, this is not due to the mass of the force carrier, as gluons are massless like photons. Instead, the limited range is because gluons carry a colour charge. Colour charge is the fundamental property introduced by QCD to describe the nature of the nuclear strong force. The nature of the colour charge itself is what leads to the limited range of the strong nuclear force.

The existence of colour charge was initially theorised due to the discovery of the Ω^- baryon. This is because the Ω^- is comprised of three strange quarks in a spin-aligned ground state. This configuration would violate the Pauli exclusion principle; thus, a new quantum number, "colour charge", was proposed by Gell-Man and Fritzsch [11] distinguishing between these states and thus not violating the exclusion principle. Both gluons and quarks have a colour charge and are governed by the nuclear strong force. Collectively gluons and quarks are known as partons. The property of colour has some unique aspects that affect how it functions. Firstly, quarks can have one of three separate colour charges, red, green or blue. These colours can be thought of as independent states. Anti-quarks have anti-colour charge, these are referred to as anti-red, anti-blue, and anti-green. Gluons have both a colour and anti-colour charge.

While QED describes the interaction of charged particles through a chargeless force carrier, QCD describes the interaction of colour-charged particles through a colour-charged force carrier. The colour-charged nature of the force carrier is responsible for the majority of the differences in how these forces interact. Specifically, gluons are composed of two colour charges, a colour-anticolour pair. This allows a gluon to interact with itself, giving rise to many of the properties of QCD.

A defining characteristic of colour charge, distinct from other quantum numbers, is that it leads to confinement in the strong force. Confinement prevents a single colour charge from being observed in isolation. Instead, colour charges are only found in colour-anticolour pairs or triplets. A straightforward way of conceptualising which colour pairs are valid is by considering combinations which sum to "white". A valid triplet combination is having all three colours (or anticolours) in the same particle as is observed in baryons. A valid pair of colours is a pair that self-negates, e.g., red and anti-red, as seen in mesons. It is possible to overcome confinement with sufficiently high temperatures and densities. In these extreme conditions, matter is believed to undergo a phase transition into an unbound hot plasma of quarks and gluons, the QGP. Investigating the properties of the QGP is one of the primary purposes of the ALICE experiment at the large hadron collider (LHC) at CERN (Geneva, Switzerland).

1.3 Strong Nuclear Force

The strong nuclear force is responsible for holding together mesons and baryons. Understanding the strong nuclear force is critical to understanding QCD. The strong force potential, V_s, is written as [12] [13],

$$V_s(r) = -\frac{4\alpha_s}{3r} + kr, \tag{1.1}$$

where α_s is the coupling constant, r is the distance between colour charged partons, and k is a constant. The first term of the potential is inversely proportional with respect to distance. This inverse proportionality is analogous to what would be seen in the electromagnetic potential. The second term is linear and thus analogous to Hooke's law as the force increases with separation. At large enough distances, $r \gg 1$ fm, the linear term dominates, and it becomes more energetically favourable to form a new quark-antiquark pair. Each original quark and antiquark are now linked to these new quarks with a gluon flux tube. This process is shown graphically in figure 1.3.

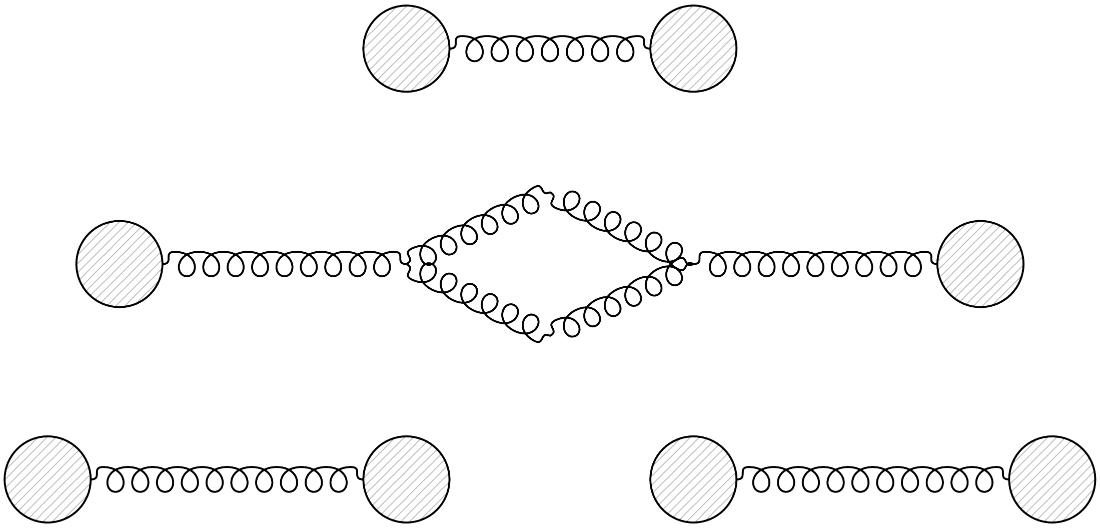

Figure 1.3: The diagram shows the concept of colour confinement. As separation increases between two quarks, the gluon flux increases until two new quarks are created. This results in the creation of two new quarks after significant separation.

This results in quarks only existing in quark antiquark pairs or triplets of the correct colour charge. This is known as confinement and prevents free colour charge from being observed as the quarks cannot be separated. This poses significant issues with studying the nature of colour charge as it prevents single colour charges from being directly observed.

1.3.1 Strong Coupling Constant

The strong coupling constant defines the strength of the strong nuclear force. The coupling constant α_s, despite its name, is not constant. α_s is a function of the four-momentum transferred in the interaction q. At leading order α_s is defined as

$$\alpha_s(q^2) = \frac{\alpha(\mu^2)}{1 + \alpha(\mu^2)\beta_0\tau}, \tag{1.2}$$

where q is the four-momentum, $\alpha(\mu^2)$ is the constant at a known measured value and $\tau =$

$\ln(\frac{q^2}{\mu^2})$. Finally, β_0 is a constant and is given by,

$$\beta_0 = \frac{1}{12\pi}(11n_c - 2n_q), \tag{1.3}$$

where n_q is the number of quark flavours, and n_c is the number of colours. In QCD, the number of quark flavours is six, and the number of colours is three; therefore, $\beta_0 = \frac{7}{4\pi}$. By defining a QCD scaling constant

$$\Omega^2_{QCD} = \mu^2 e^{\frac{-4\pi}{\beta_0 \alpha_s(\mu)^2}}, \tag{1.4}$$

it becomes possible to write equation 1.2 as,

$$\alpha_s(Q) = \frac{4\pi}{\beta_0 \ln \frac{Q^2}{\Omega^2_{QCD}}}. \tag{1.5}$$

As the distance between partons decreases, $Q^2 >> \Omega^2_{QCD}$, this results in α_s becoming insignificant. Where Q is four momentum ofa collision. This effect dominates over the increase from the $\frac{1}{r}$ term in equation 1.1. Thus, at small r, the potential $V_s \to 0$ instead of approaching infinity. At these small distances, QCD can be calculated using perturbation theory. At larger distances, perturbation theory is not usable, thus, numerical methods and techniques such as lattice QCD must be used in this regime [14].

Due to its energy dependence, the strong coupling constant is given the name the running coupling. Its variable nature is corroborated through measurements preformed by several experiments at various accelerators over the years, including HERA at the e-p collider or more recently at the LHC by CMS [15] and the ATLAS experiments [16] at the LHC, which have measured values of α_s as a function of the momentum transfer of an interaction, shown in figure 1.4.

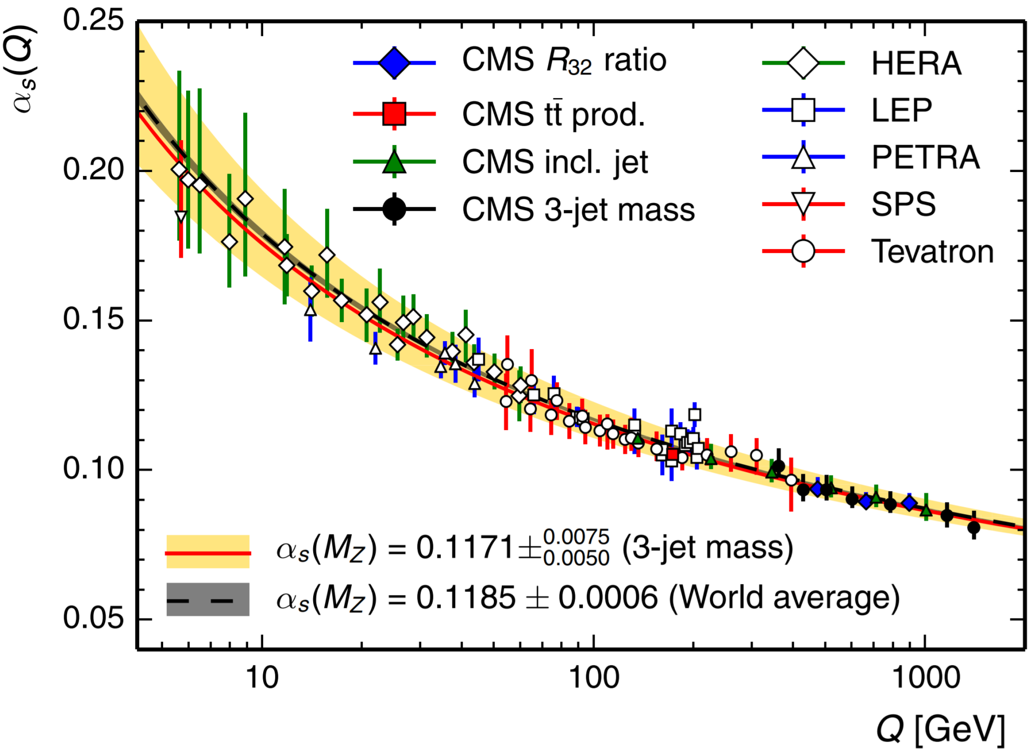

Figure 1.4: The figure shows measurements from multiple collider experiments showing the dependence of the strong coupling constant on the energy of collisions. The x-axis Q is the four momentum of the collision. The strong coupling constant α_s in this case is measured as a function of an invariant mass M_z between 445 - 3270 GeV. Figure taken from Ref [15].

1.3.2 Asymptotic Freedom

The variation in the strength of the coupling constants in both QED and QCD arises due to screening. The screening is a consequence of the creation of particle-antiparticle pairs in the space between particles. These fluctuations are known as quantum vacuum fluctuations and are a consequence of the uncertainty principle. The presence of a charged particle will polarise the particles created from these fluctuations.

In QED, the electrical charge of these particles screens the particle from a theoretical test charge, thus reducing the effective observed charge. This effect increases with the distance between the charged particle and the test charge since, as the distance increases, the number of polarised particle-antiparticle pairs also increases.

In QCD, the process is analogous. A test colour charge is screened from the colour charge of a particle due to the colour charge present in these quantum fluctuations. However, due to the self-interaction of gluons, there is a secondary effect produced by gluon loops that are created and shown in the Feynman diagram in figure 1.5. These gluon loops have the effect of increasing the effective colour charge as distance increases. This effect dominates over the colour charge shielding at large distances. As $q^2 \to \infty$, then, $\alpha_s \to 0$. At this limit, the strong nuclear force is negligible, and the colour charge is unbound. Hence, QCD is known as an asymptotically free theory [17]. While this method could allow the observation of colour charge, it is not the experimental method pursued to achieve deconfinement with particle accelerators at this time. This is because the energies required to achieve this would be impracticably high; significantly higher than what is achievable with current collider energies.

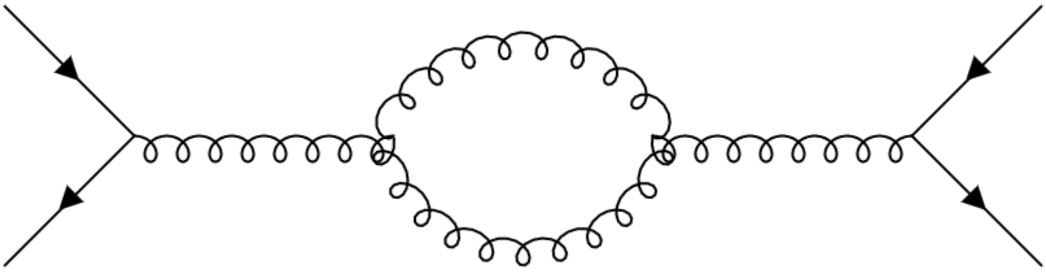

Figure 1.5: The figure shows the first-order Feynman diagram of gluon self-interaction between two quarks.

1.3.3 Debye Screening

Asymptotic freedom suggests an energy level for deconfinement which is far larger than what is currently achievable. However, the energies required for deconfinement are observed to be lower that asymptotic freedom would suggest. This is a result of Debye screening [18]. Debye screening occurs when colour charges are screened by the polarised colour charges between them in dense systems. The consequence of Debye screening is that the colour charges only interact within a characteristic screening length r_D. The effects of Debye screening in QCD are defined as,

$$V_{QCD} = -\frac{\alpha_s}{r} \exp\left(\frac{-r}{r_D}\right), \tag{1.6}$$

where r_D is the distance over which colour charges are no longer able to interact. This is known as the screening length. Next, r_D is inversely proportional to the temperature and density of the system. As r_D decreases, at the critical temperature, it becomes smaller than the binding radius of valence quarks. This limit is when the phase transition into the QGP occurs. The system is no longer a system of bound hadrons but is instead a fluid composed of strongly interacting but deconfined quarks and gluons. The energies required to achieve this critical temperature are significantly lower than the energies required for asymptotic freedom. These conditions are achievable in modern particle accelerators. The critical temperature, T_c, required to achieve deconfinement due to Debye screening can be calculated theoretically. This is investigated using lattice QCD. Lattice QCD calculations predicts the value of $T_c = 150 - 170$ MeV [19] [20].

1.3.4 QGP

Once the energies required for deconfinement due to Debye screening have been reached in a collision, then QGP is formed. In this state of matter, quarks and gluons are free instead of being confined to hadrons. Debye screening results in the phase transition occurring before asymptotic freedom $\alpha_s > 0$, and thus, the medium remains strongly interacting. This state of matter provides an excellent opportunity to study the behaviour of strongly interacting but deconfined colour-charged partons. The QGP has been produced using heavy-ion collisions in particle accelerators. These heavy-ion collisions have used both gold (Au-Au) and lead (Pb-Pb) ions. heavy-ions are used because the high density created in these collisions is required for the extreme temperatures and densities required to form QGP.

The first evidence of the production of QGP occurred in 1994 as CERN's heavy-ion programme entered its second phase. The Super Proton Synchrotron accelerated lead ions to collide with a fixed target in an attempt to produce QGP. The experiments set up to analyse the data from these collisions resulted in the first observations that suggested the presence of a new quark-deconfined state of matter. The key signatures were strangeness enhancement [21] and charmonium suppression [22]. These phenomena were the first observed evidence of QGP and provided the basis for later work.

The experiments that followed took place at the Relativistic Heavy Ion Collider (RHIC) at the Brookhaven National Laboratory (BNL) using its four experiments, namely; PHOBOS [23], BRAHMS [24], STAR [25] and PHENIX [26]. The Au-Au runs began in 2000 with $\sqrt{s_{NN}} = 130$ GeV (Note: $\sqrt{s_{NN}}$ refers to the centre of mass energy per nucleon). Initial results were in agreement with the findings from SPS. RHIC continued to add significantly to furthering the knowledge of the properties of the QGP, showing that the QGP is an almost perfect fluid [27] and is opaque to high momentum hadrons [28] [29] [30] [31] [32].

The current frontier of heavy-ion collider physics is being explored at the Large Hadron Collider (LHC) at CERN. ALICE [33] is the only one of the detectors at the LHC that is specifically designed to study heavy-ion collisions. The first heavy-ion collisions at ALICE started in 2010 with a centre of mass energy of $\sqrt{S_{NN}} = 2.76$ TeV, marking a significant increase in energy. This was then followed by the start of the LHC Run 2 in 2015 when the centre of mass energy was increased to $\sqrt{S_{NN}} = 5.02$ TeV. The data analysed in this thesis are from this Run 2 period. The increased energy in these collisions increases the probability of larger momentum scatterings. An increase in the number of high-momentum scatters increases the number of jets available to probe the QGP. This is because a jet is a particle shower resulting from a high momentum parton scatter. Thus, at these high energies, jets become a meaningful tool with which to explore the nature of the QGP.

The QGP does not form instantaneously, and due to its extremely hot and dense nature, it only exists for a very short amount of time. The timeline of the formation of QGP in collisions is shown in figure 1.6 [34]. It is thought that the QGP takes approximately $t = 1$ fm/c to form after the initial collision [35]. Once the medium begins to expand and cool hadronic freeze-out occurs, returning the particles to a hadronic state in approximately 10 fm/c [36].

1.3.5 Centrality

Due to the extended size of lead nuclei, the degree of overlap between nuclei varies from collision to collision. Collisions vary between "Central" head-on collisions and peripheral collisions with only the edge of each nuclei overlapping. Centrality is a variable introduced to define the degree with which each colliding nuclei overlap [37]. The more central a collision, the greater the degree of overlap between nuclei. This is defined as a percentage of overlap; the lower the percentage, the more head-on the collisions. The centrality of a collision is an

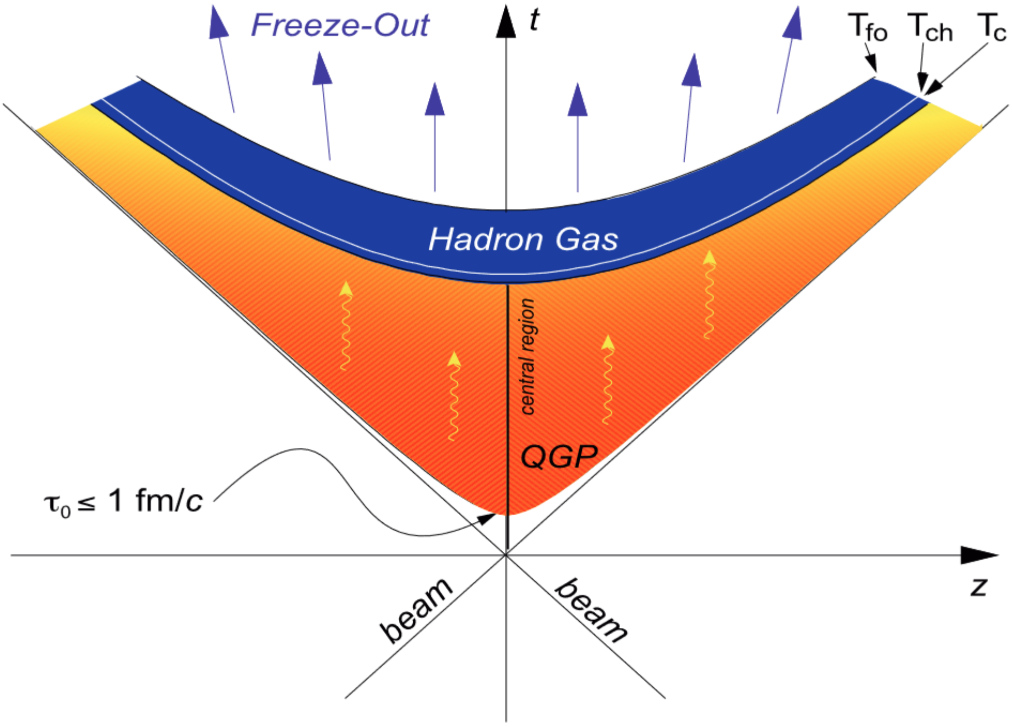

Figure 1.6: The figure shows a light cone diagram showing the evolution of the QGP in a heavy-ion collision. The QGP forms after 1 fm/c, and hadronic freeze-out occurs once the medium has reached a critical temperature T_c. The critical freeze-out temperature, T_{ch}, is where hadron species ratios are fixed and inelastic collisions cease and T_{fo} is a kinetic freeze-out temperature where elastic collisions cease as well. Particles only reach the detector after cooling below the kinetic freeze-out temperature. Figure taken from [34].

important parameter to consider for collisions, as a more central collision leads to a larger volume to study. Thus, the more central a collision, the larger and more long-lived the QGP.

1.3.6 Energy Loss from the QGP

The energy lost from high momentum partons as they traverse the QGP is a key piece of evidence when investigating the creation of the QGP. Partons that traverse through the medium are expected to interact with the QGP and lose energy. In QCD, this energy loss is by the emission of gluons. This is analogous to QED, where the energy loss would be made via the emissions of photons. Depending on the formalism, it is possible that this energy is carried away by many low transverse momentum gluons or fewer high transverse momentum gluons.

The theorised energy loss has been observed experimentally by comparing pp collisions (where no QGP is produced) to Pb-Pb collisions. In these cases, there is an observed suppression of high p_T hadrons in heavy-ion collisions [38] [39]. High p_T hadrons can be used to investigate the effects the QGP is having on high p_T partons in the initial stage of the collision as these hadrons originate from partons that are scattered through large angles transverse to the beam. These hard scatters are the origin of jets.

The first experimental evidence to motivate the energy loss from the QGP was observed in the suppression of high momentum hadrons in Pb-Pb collisions when compared to pp collisions [40] [41] [42] [39]. These high-momentum hadrons can be used as a proxy to the high-momentum parton that is scattered in the initial collision, which forms a jet. The ratio between p_T charged hadrons in Pb-Pb collisions and pp collisions can be used as a measurement of this suppression and is known as the nuclear modification factor R_{AA}. Without the effects of the QGP, the expected yield of high p_T hadrons in Pb-Pb collisions would be expected to be a superposition of multiple pp collisions. Therefore, the yields in pp collisions are scaled by the binary number of nucleon collisions in a heavy-ion event leading to $R_{AA} = 1$ representing no effects by the medium. The energy loss due to the medium is shown in figure 1.7, which shows the R_{AA} for both the ALICE and CMS detectors for both Pb-Pb and p-Pb collisions [43]. The figure shows little deviation from unity in p-Pb collisions at high p_T, and a significant deviation from unity is shown in Pb-Pb collisions. As p-Pb collisions are not expected to form a QGP, the deviation from Pb-Pb collisions can be inferred to be a QGP effect. The suppression is an effect of the QGP affected by the centrality of a given collision with figure 1.7 using only the $0-5\%$ most central collisions. It is important to note from the figure that R_{AA} is p_T dependent. Lower p_T particles have a smaller R_{AA} and thus are more affected by the medium.

1.4 Jets in the QGP

Studying the nature of the QGP requires the use of specific techniques. These techniques are required because of the limited lifetime of the QGP when it is formed in heavy-ion collisions. This limited lifetime means that it is not possible to measure partons in the QGP directly. Instead, information about partons must be extracted from the final state hadrons which the detector measures. These hadrons retain some information about the QGP as the partons which hadronised into the final state particles originated from within the QGP. Thus, these partons have interacted with the QGP and can be investigated to probe the QGP's properties. Because of this, properties of the QGP are often investigated by comparison between heavy-ion collisions, which produce QGP, and pp collisions which do not produce QGP.

The probe for the QGP used in this thesis are jets. Jets are highly collimated showers

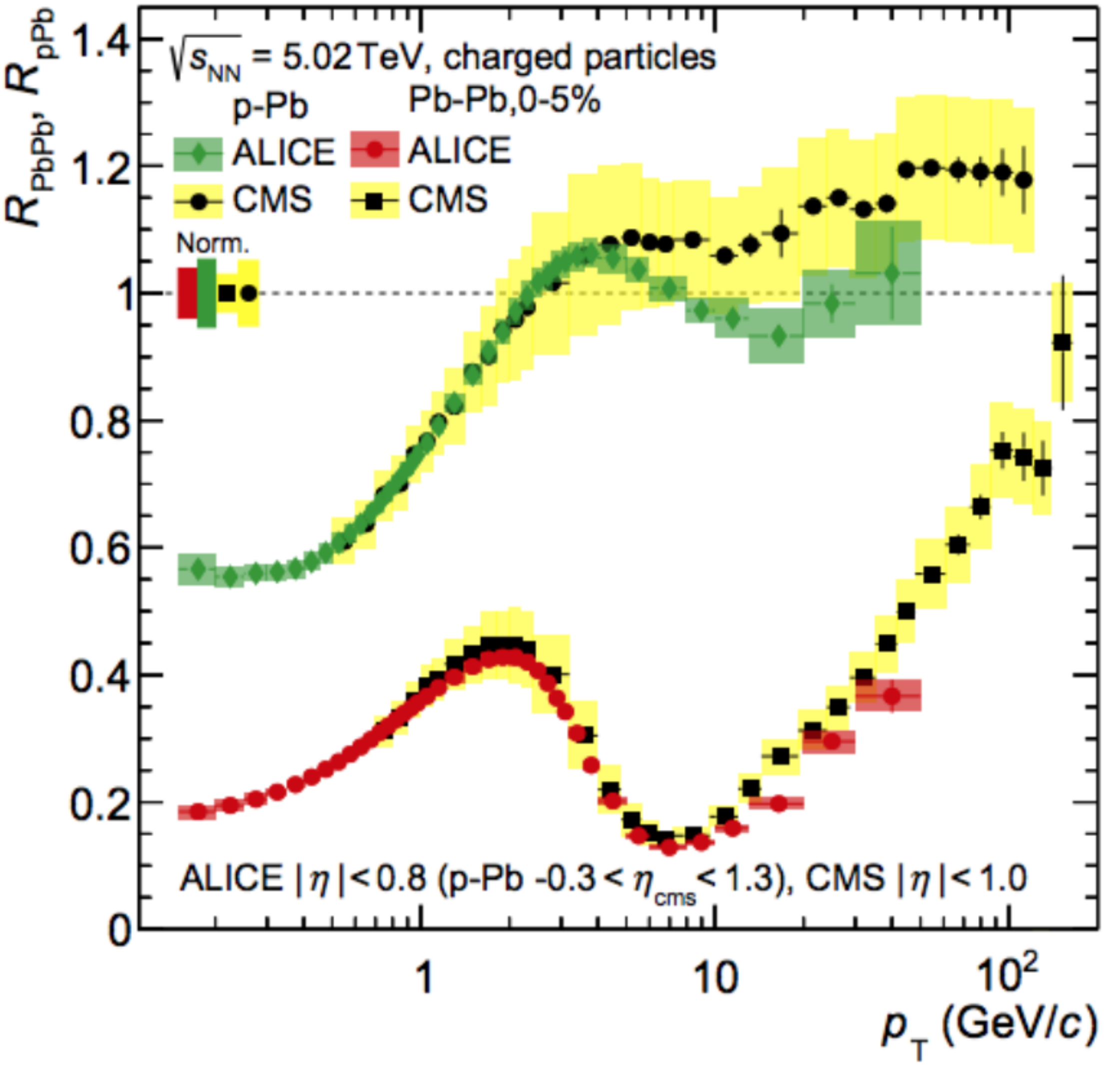

Figure 1.7: The figure shows the nuclear modification factor R_{AA} for both the ALICE detector (in green and red) and the CMS detector (In black). The R_{AA} varies based on the p_T of the charged hadrons. This is because the mechanisms for the production of charged hadrons with $p_T <$ 3 GeV/c are different from the mechanism for higher momentum hard scatter hadrons, thus, are affected differently by the medium. These higher momentum-charged hadrons show a significant quenching effect [43].

of hadrons produced from a single collision with a large momentum transfer (hard scatter). Jets provide a powerful insight into the QGP. The hard scatters that result in jets occur during the initial collision. Thus, they are affected by the QGP as they traverse through it. Since jets originate from a single high-momentum parton, it is the interaction between this parton and the medium of the QGP which will affect the nature of jets seen in Pb-Pb compared to pp collisions. This process leads to a deficit of high p_T hadrons known as jet quenching.

One of the main challenges with this approach to investigating the properties of the QGP using jets is the presence of the underlying event in Pb-Pb. This is because the multiplicity of Pb-Pb collisions is significantly higher than those of pp collisions, meaning it is difficult to separate the jet from particles not in the jet. Thus, one of the main challenges is finding ways to mitigate the effects of these background particles while not influencing the properties of the jet.

The variables that are used to categorise the properties of jets are known as jet shapes. Jet shapes are variables constructed from the properties of the jet and its constituent hadrons to characterise features of the jet. Jet shapes can vary in complexity, the simplest being properties such as the jet's transverse momentum or the total energy of the jet, and the more complex jet shapes can be constructed from multiple of these simpler properties.

1.4.1 Jet Charge

The jet shape that is the focus of this analysis is known as jet charge. The jet charge is the momentum-weighted sum of the electrical charge of the jet constituents and is mathematically defined as,

$$Q^k = \frac{1}{(p_T^{\mathrm{jet}})^k} \sum_{i \in \mathrm{jet}} q_i (p_T^i)^k, \tag{1.7}$$

where Q^k is the jet charge, p_T^{jet} and p_T^i are the transverse momenta of the jet and track, respectively, and q_i is the electrical charge of the jet constituent. The power factor, k, defines a jet's sensitivity to high-momentum tracks. Setting $k = 0.5$ is recommended as it provides the greatest sensitivity to the charge of the jet's original parton [44].

The parameter was first suggested by Field and Feynman in 1978 as a technique for measuring the charge of a quark [45]. Jet charge was first measured in deep inelastic scattering experiments at Fermilab [46] [47], CERN [48] [49] [50] [51] and Cornell [52].

It has been suggested that jet charge can be used to predict the type of parton which created the jet. This is because the electrical charge of the jet's progenitor parton is related to the jet charge measured in the final state particles. Measuring jet charge distributions from different flavours of partons makes it possible to see how these partons are influencing the jet charge. Additionally, by studying jet charge distributions in pp and Pb-Pb collisions, it becomes possible to measure the effect the QGP has on the jet charge. By analysing these effects, it is possible to see how the QGP is affecting the proportion of quark-initiated jets (quark-like jets) and gluon-initiated jets (gluon-like jets). Recent measurements suggest that the relative fraction of quark-like and gluon-like jets could be affected by the presence of QGP [53] [54]. Theoretical calculations of the interaction of QGP with quarks and gluons predict stronger interactions with gluons compared to quarks. Thus, this will result in a reduced fraction of gluon jets in Pb-Pb collisions when compared to pp collisions due to the energy loss from this interaction [55].

Previous recent investigations into jet charge at the LHC have been conducted by CMS [56] [57]. These analyses were motivated by recent theoretical predictions on jet charge [58]

[55] [59]. These analyses attempt to characterise jet charge as well as to show a suppression of gluon-like jets in Pb-Pb collisions. The jet charge distributions measured in this analysis can be seen in figure 1.8. These figures provide some observations for jet charge distributions. Firstly, the jet charge distributions from different flavours show significant overlap in range. Secondly, the distributions are gluon dominated. The jet charge distributions shown are first extracted from Monte-Carlo data and then fitted to the data from CMS in order to match the MC yields to the observed yields. Fitting these yields should allow extraction of some of the differences between Pb-Pb data and the pp MC.

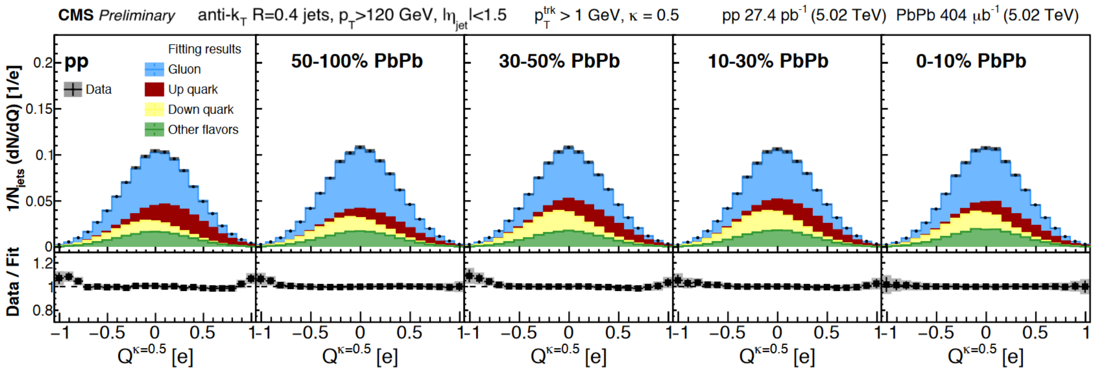

Figure 1.8: The top series of graphs show jet charge measurements from CMS showing the jet charge distribution for data as well as the fitted jet charge distributions from different progenitor partons from Monte-Carlo as a series of stacked histograms (i.e. each coloured histogram is stacked on top of the previous instead of being overlaid). These are separated from left to right from pp to increasingly central Pb-Pb collisions. The bottom series of graphs show the ratio between the data and the fitted Monte-Carlo shown in the graph above. Note the gluon jets form the majority of jets in all systems. Additionally, note the shift from up quark jet contributing to the second largest fraction in pp to down quark jets being the second largest fraction in Pb-Pb. This is due to the increased relative fraction of down quarks to up quarks in Pb compared to protons. Figure taken from Ref [56].

The relative shift experienced by these jet charge distributions is seen in the means of each distribution shown in the table 1.2.

Figure 1.9 shows the fraction of gluon jets found by CMS when comparing track p_T

Table 1.2: The table shows means given for the jet charge distributions of a given parton. The uncertainties are not given as they are not given by CMS. [56]

Parton	$< Q >$ [e]
Gluon	0.001
Up	0.288
Down	-0.165

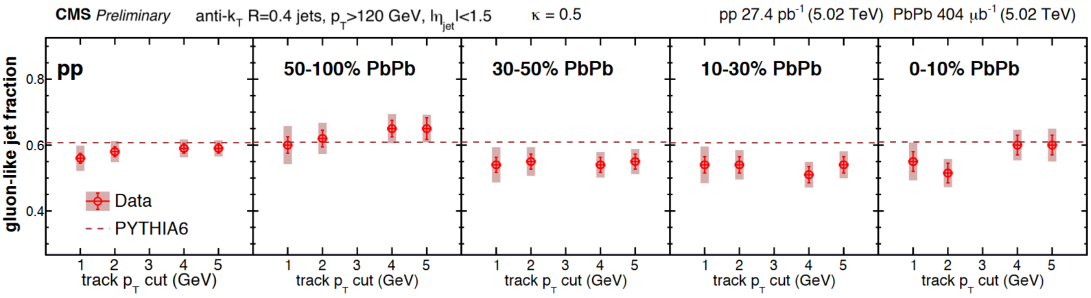

Figure 1.9: The figure shows the fraction of gluon-like jets found in CMS. It shows how these gluon-like jet fractions vary based on the track p_T cut as well as when in pp and increasingly central Pb-Pb collisions. The dotted line shows the gluon-like jet fraction measured directly from PYTHIA6 without fitting to data. Figure taken from Ref [56].

cuts as well as between pp and increasingly central Pb-Pb collisions. The gluon-like jet fraction directly extracted from PYTHIA6 is also plotted as the dotted line. PYTHIA6 is a Monte-Carlo event generator. This figure shows that there is some evidence of variance in gluon-like jet fraction between pp and Pb-Pb. However, it is unclear that there is a significant suppression of the gluon-like jets due to the QGP as theorised. The measured gluon-like jet fraction is the same within errors for all presented values by CMS. This suppression would be seen as a significant adjustment in the gluon-like jet yields in Pb-Pb collisions when compared to pp collisions. Instead, there is an increase in the gluon-like jet fraction in the $50-100\%$ centrality bins when compared to pp. Additionally, while there is a reduction in the gluon-like jet fraction in the $30-50\%$ as well as $10-30\%$ centrality bins, the effects are marginal. Finally, the most central bin in Pb-Pb collisions, $0-10\%$, where the largest effect from the QGP would be expected, shows an increase in the gluon-like jet fraction over less central collisions.

While CMS has already conducted the analysis performed in this area, there is still an interesting avenue for the ALICE detector to explore. The CMS detector is not specialised in measuring heavy-ion collisions, and thus the ALICE detector may be able to provide more insight when exploring the most central Pb-Pb collisions. Additionally, due to its strong magnetic field, the CMS detector is designed to probe a significantly higher track momentum space than the ALICE detector. However, this magnetic field prevents the CMS detector from being able to reconstruct low-momentum tracks. Therefore, the ALICE detector has a significant advantage when it comes to probing the soft track space as it has a minimum track $p_T = 0.15\ \text{GeV/c}$, an order of magnitude lower than the smallest $p_T = 1\ \text{GeV/c}$ shown in the CMS analysis. As seen in figure 1.7 the extent to which particles and by extension jets are affected by the medium is p_T dependent. Therefore, these lower momentum tracks might hold key information on the jet charge that the CMS detector is unable to reconstruct. Therefore, with a significantly different parameter space than the analysis performed using the CMS detector, it is possible that further insight into the nature of the QGP's effect on jet charge might be uncovered.

Chapter Two

Jet Physics

2.1 Overview

A jet is a highly collimated spray of particles resulting from a single hard scatter between two partons in the initial collision. As the scattered partons propagate, they hadronise and decay, splitting into several hadrons. These series of decays result in the particles spreading out into a widened cone of hadrons. The decay continues until it forms a shower of particles which are measured by the detector. This cascading decay results in many particles observed, all of which share a common progenitor parton. Since the initial hard scatter is a collision between two or more partons, jets are always formed in pairs or more. Although it should be noted that the corresponding paired jet is not always detectable as it can have lower momentum or otherwise fall outside of the acceptance of the detector.

2.2 Jet-finding

Defining a jet from theory can be helpful when conceptualising jet physics and trying to understand its characteristics. However, the theoretical definition is not always practical.

This impracticality exists because it is currently impossible to detect the initial hard scatter of the jet directly. Instead, the jet is detected only through the final state particles interacting with the detector. Therefore, it is helpful to have a different definition which uses the final state particles to categorise the jet instead of the initial hard scatter. When dealing with real data, a jet is defined as follows: a jet is any set of final-stage particles clustered by a jet-finding algorithm. This definition allows the jet to be considered from only the perspective of final state particles rather than needing information from the initial collision.

With this definition based on final state particles, it is essential to clarify a few details. Firstly, with this jet definition, it is possible to cluster groups of particles together, which are, in fact, not genuine jets. These are known as combinatorial jets. These jets result from a large momentum in a given area of the detector. In order to avoid this, several parameters can be tweaked in the algorithm to minimise this effect. The main one of these parameters is the $p_{T,\mathrm{chjet,min}}$. This parameter is important as it ensures that only areas clustered above a momentum threshold will be accepted as jets. Secondly, it is essential to note that because of this definition, what is or is not a jet depends on our choice of parameters. Not only might there be new jets, but which particles are considered part of the jet and which particles are considered background is also affected by choice of parameters in the jet-finding algorithm. Therefore, it should be realised that a given jet is not unique but instead a function of the parameters used in the jet-finding algorithm.

With this in mind, several jet-finding algorithms have been developed [60][61][62][63]. These algorithms aim to attempt to recreate the logic of jet decay and reverse-engineer the quantum mechanical fragmentation process. Thus, in theory, a jet-finding algorithm causes particles to be clustered together in a way which reverses the fragmenting process.

Each jet-finding process must meet specific criteria for these algorithms to be rigorous enough for experimental analysis. Namely, they must be both infrared and collinear (IRC) safe. IRC safety is a series of rules requiring that the distribution of jets identified should be unmodified by the algorithm when soft infrared emissions are added. Additionally, the algorithm must produce jets unaffected by collinear splitting. IRC safety is vital since collinear splitting and soft radiation are both standard features of fragmentation. Ensuring this insensitivity can be critical to reducing their effects on jet finding. IRC safety is particularly important for soft radiation in Pb-Pb collisions, as the jets are in a background-dominated environment.

Infrared (IR) safety is critical since an IR-unsafe algorithm breaks the relationship between the partonic structure of the event and the observed structure. This relationship is crucial when analysing events as this structure must be maintained to understand and account for detector effects. The role of a jet-finding algorithm is to link the true jets to their observed counterparts. Therefore, being IR-unsafe would effectively make an algorithm unusable.

The first component of IRC safety is the detector itself. The detector provides an element of IRC safety by default due to the acceptance limits for very low transverse momentum tracks $p_{T,\text{track}} \rightarrow 0.150$ GeV/c. Combining this with the tracker's finite resolution ensures that jets are independent of the detector. Next, the algorithm must be tweaked to be safe as well. The fragmentation process is non-deterministic; thus, the jet-finding algorithms must be unaffected by them.

There is more than one way to approach the jet-finding process. These fall into two categories, cone-type algorithms [64] and sequential recombination algorithms. Cone-type algorithms are typically not IRC-safe. Additionally, Cone-type algorithms tend towards being more complex, requiring non-physical parameters for the algorithm to function. Sequential-recombination algorithms, in contrast to cone algorithms, are IRC-safe by design. Sequential-recombination algorithms are the only type used in this work.

The three most commonly used sequential recombination algorithms are k_T [60], anti-k_T [61] and Cambridge-Aachen [62] [63]. Each algorithm differs in its advantages and disadvantages and thus should be selected depending on the goal of the analysis.

There are two main parameters to be considered in a sequential recombination algorithm. These parameters are the distances between any two particles i and j:

$$d_{i,j} = min((k_{T,i})^p, (k_{T,j})^p)\frac{R_{i,j}^2}{R^2} \tag{2.1}$$

and the distance between the particle and the beam,

$$d_{i,B} = k_{T,i}^p, \tag{2.2}$$

where d_{ij} is the distance between the particles i and j, and d_{iB} is the distance between the particle i and the beam. Parameters $k_{T,i}$ and $k_{T,j}$ are the transverse momentum of the particles i and j. Finally, p is a parameter defined by the choice of jet finding algorithm. Additionally,

$$R_{ij}^2 = (\eta_i - \eta_j)^2 + (\theta_i + \theta_j)^2 \tag{2.3}$$

defines the radial distance between the particles and in the azimuthal-pseudorapidity plane squared. The parameter η is the pseudorapidity and θ is the azimuthal angle and R^2 is the square of the jet radius. The jet radius is a parameter predefined for the jet finding, which is used to define and constrain the size of the jet. The parameter p is set to determine the relative dependence of geometry compared to energy. The value of p is determined by the recombination algorithm used.

A general sequential clustering algorithm uses the following series of steps:

- Calculate the values of d_{ij} and d_{iB} for all particles in a given event,
- Find the smallest values of d_{ij} and d_{iB} for all particles,
- If the smallest value is a d_{ij} value, combine the two particles i and j using the recombination scheme,
- If the smallest is a d_{iB} value, remove the particle i, label this particle as part of the jet, and remove this item from the list,
- Repeat these steps until every particle has been clustered into a jet,

2.2.1 k_T Algorithm

The k_T algorithm is the sequential recombination algorithm that was first used. It was used originally by scientists working with the Large Electron-Positron collider at CERN [65]. For the k_T algorithm $p = 2$. This algorithm was initially extremely slow. However, implementing the algorithm in the FastJet package [66] drastically improved its speed and usability. Using this algorithm produces distance measurements between particles that are closest to the structure of divergences in the QCD emissions. The k_T algorithm more strongly weights low momentum particles. Thus, this algorithm is used to categorise the background in this analysis.

2.2.2 Anti-k_T Algorithm

The anti-k_T algorithm is the most commonly used jet-finding algorithm for analysing heavy-ion collisions at the ALICE detector. This algorithm causes clustering around a core of leading particles. This structure is because of the parameter choice for anti-k_T, $p = -2$. This results in jets with a more circular shape when compared to the other jet finding algorithm. Thankfully, the algorithm is still IRC-safe despite this. A final advantage of the anti-k_T algorithm is that it should be mainly unaffected by changes in the underlying event and pile-up. This is because the algorithm clusters high p_T particles first which should be above the background. These factors make it particularly well suited for jet finding in Pb-Pb collisions.

2.2.3 Cambridge-Aachen

The Cambridge-Aachen (C/A) algorithm depends only on the spatial separation of tracks. This approach differs from the k_T and anti-k_T, which consider the transverse momentum of the tracks. Practically speaking, this means that the parameters in the algorithm, corresponding to $p = 0$. Therefore, the equations simplify so that d_{ij} simplifies to ΔR_{ij}. The C/A algorithm is excellent in resolving jet substructure. The algorithm allows undoing the pairwise clustering of the jet. It is possible to identify the sub-jets that make up the original jet. The C/A algorithm will cluster all tracks into a jet within the maximum radius R that is set when programming the algorithm. If the total $p_{T,jet}$ is above a set minimum threshold, then the resulting cluster of particles is considered a jet instead of part of the underlying event.

2.3 Jet Quenching

Jet quenching is the name given to the process through which the QGP reduces the overall energy of a jet. This suppression occurs as the parton traverses through the QGP and interacts with the medium. There are two mechanisms that primarily cause this quenching.

Firstly, collisions between the particles and the partons in the QGP can cause the jet's progenitor parton to lose energy as these collisions transfer momentum from the parton to the soft background particles in the QGP. The second mechanism for energy loss in QGP is radiatively through gluon Bremsstrahlung. Both processes are shown in figure 2.1. Gluon Bremsstrahlung is a mechanism only permitted within the medium of the QGP due to the system's state of deconfinement. Due to this property, radiated gluons can exist and travel through the QGP, losing energy.

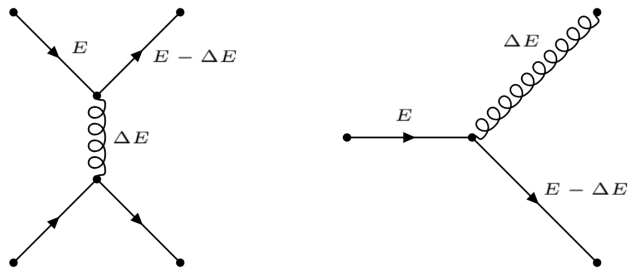

Figure 2.1: Feynman diagram showing both methods of energy loss in jet quenching with the left showing collisional energy loss, and the right, gluon Bremsstrahlung.

Bjorken first estimated collisional energy loss in 1982 [67]. At low momenta, energy loss via collisions is the dominating term. The average energy loss per scattering event is modelled by the following,

$$\langle \Delta E_{coll}^{1scat} \rangle = \frac{1}{\sigma T} \int t \frac{d\sigma}{dt} dt, \tag{2.4}$$

where σ is the scattering cross-section, t is the momentum transfer, and T is the system's temperature [68].

Alternatively, at higher momenta, radiative energy loss is the dominant mechanism. In general the radiated energy loss for a charge traversing a medium is given by the Bremsstrahlung spectrum,

$$\langle \Delta E_{rad}^{1scat} \rangle = \int \omega \frac{dI_{rad}}{d\omega} d\omega, \tag{2.5}$$

where ω is the energy of the parton/gluon radiated and I_{rad} is the intensity of radiation.

An interesting aspect of jet quenching is that it can cause single jets to be detected. This can occur because, while jets are formed in at least pairs, the energy reduction from jet quenching can cause the total energy of a jet to fall outside of the threshold required for jet finding. Typically, this will occur when the initial hard scatter of two partons is on the edge of the QGP volume. This is because this position in the QGP will mean that one parton will have to traverse only a small fraction of the entire QGP. In contrast, the other parton, since it will be travelling in the opposite direction, will have to traverse through a much more significant fraction of the QGP and thus will lose more energy in the QGP.

Measurements of jet quenching provide indirect evidence of the production of QGP in heavy-ion collisions. This is achieved by the comparison between pp collisions, where no QGP is produced when compared to those in Pb-Pb collisions with QGP. These comparisons show the suppression of high energy partons was found in the presence of the QGP [28] [29] [30] [31] [32]. By studying the scale of the energy loss through jet quenching, information can be revealed about the properties of the QGP, such as temperature, density and size.

2.4 Background subtraction

One of the main difficulties in analysing heavy-ion collisions is in handling the background-dominated environment. This is a particularly large challenge in jet finding since the jet constituents are interspersed within the soft particles from the underlying collisions that are not members of the true jet. The background particles in Pb-Pb collisions can affect the jet distributions in three ways. The first way is that many soft tracks in a small enough area can be found as a jet despite not originating from a single hard scatter. This is known as a combinatorial jet and can cause difficulties as they do not share a common origin and thus have different properties from genuine jets.

The second way background can affect a jet is from background tracks being clustered into a jet by the jet finding algorithm despite not originating from the same partonic hard scatter. This can cause problems if trying to study a property of all the particles in the jet, as these particles will smear those effects.

Finally, the third way the background can influence a jet is if a jet's momentum is below the level of the average momentum of background particles, then the jet will not be detectable.

In order to help combat the background effects on jet finding, several techniques have been developed for mitigating this problem. These have the difficult task of reducing the effects of the background while not affecting the properties of the jet.

One of the most commonly used background subtraction techniques, and the one used for this analysis, is the constituent subtraction technique. This background subtraction technique was explicitly developed to preserve the jet substructure. The constituent subtraction method was developed from the previous pile-up subtraction techniques that used the shape-expansion method and area-based subtraction [69]. The constituent subtraction method instead subtracts the background on the level of individual particles instead of from the jet as a whole. This is an improvement in maintaining jet shapes and jet kinematics compared to the area-based subtraction method. This was shown using comparisons with jets from PYTHIA-generated pp collisions at a generator level [69]. It should be noted that the constituent subtraction method is unaware of which articles are "background" and thus subtracts momentum from the nearest particle rather than knowing what is a part of the true jet.

2.4.1 Background Momentum Density Calculation

Before any background subtraction techniques can be used, it is important first to characterise the background. The momentum density of the background ρ must be calculated first. In order to do this, an initial pass of jet finding must be carried out for the event as a whole with a given jet radius R. In order to avoid real jets being used here when categorising the background, the two highest momentum clusters are discarded since any event is liable to contain two jets from a single hard scatter. This step is not required in all analyses but is performed with this one, as is typical with jet analysis in ALICE. Once the jet finding is complete and the entire event is clustered, the background density ρ is found with the following equation,

$$\rho = \frac{p_{T,jet}}{A_{jet}}, \tag{2.6}$$

where $p_{T,jet}$ is the transverse momentum of the clustered background and A_{jet} is the area of the jet. Determining the area poses a difficulty as the jet does not have an exact shape or boundaries. Instead, the area is determined by the number of false "ghost" tracks. These ghost tracks are massless and initially carry an insignificant amount of momentum. Due to the algorithm's IRC-safe nature and the ghost particles' extremely low momentum, their addition should not affect the jet. This technique using ghost tracks is used to determine the jet area since the exact area of a jet is not clearly defined [66]. The ghost tracks are distributed uniformly throughout the event in the η - ϕ plane separated to cover a corresponding area of $A_g = 0.01$ in η - ϕ space. The number of ghosts clustered into the jet can then be counted and used to calculate the area of the jet. Once this area is known, it can be used to calculate the mean momentum density needed to perform background subtraction.

The parameter, ρ, is strongly influenced by the centrality of a collision. This is shown in figure 2.2, where the mean background momentum density increases by approximately a factor of 200 between the most and least central collisions. This means that the most central collisions are the most reliant on background subtraction techniques.

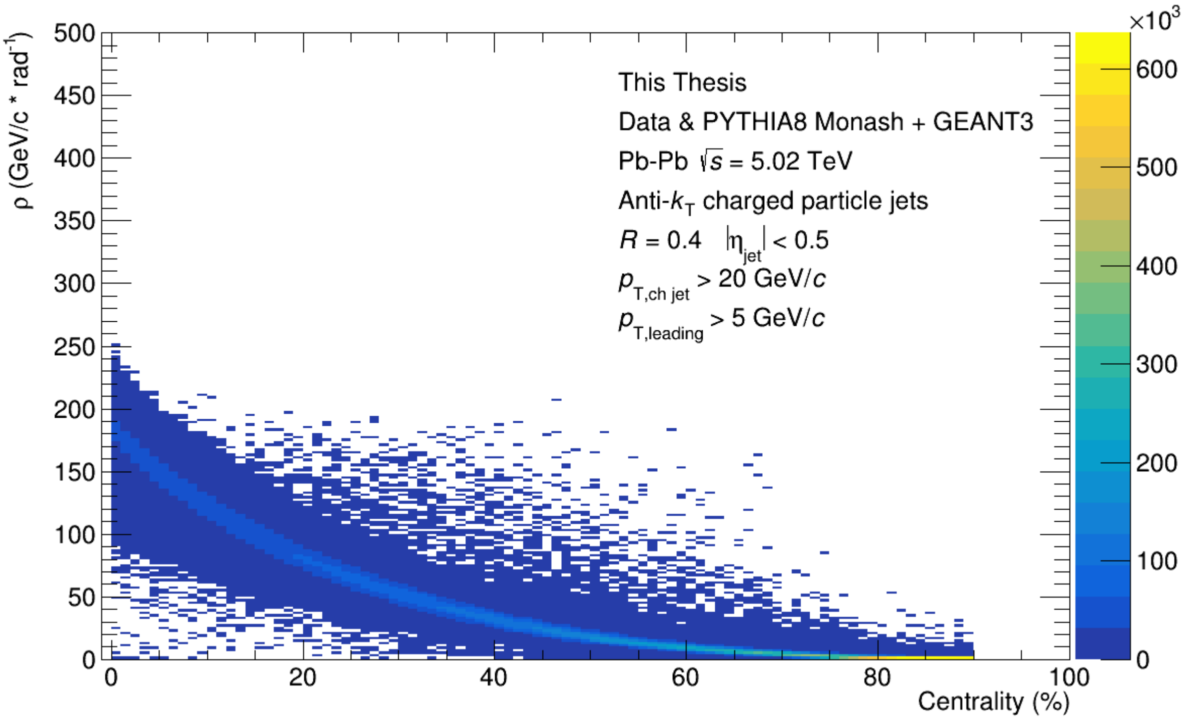

Figure 2.2: The figure shows the mean background momentum density, ρ, of events in Pb-Pb collisions between $0 - 100\%$ centralities. This demonstrates the large increase in background effects as centrality increases. See chapter 4 for more specific details regarding the cuts taken to generate this data.

2.4.2 Constituent Subtraction

The constituent subtraction technique subtracts momentum on a track-by-track basis [69]. The first step is calculating the distance between each particle and ghost in the jet. This is calculated with the following equation,

$$\Delta R_{i,g} = p^{\alpha}_{T,i}\sqrt{(\eta_i - \eta_g)^2 + (\phi_i - \phi_g)^2}, \tag{2.7}$$

where the subscript i denotes the particle and subscript g denotes the ghost. The parameters, η, and, ϕ, are the pseudorapidity and azimuthal angle of the particle, respectively. The transverse momentum of the particle is $p_{T,i}$. Here, α, is a tuneable parameter in the algorithm. Typically, the recommended value of $\alpha = 0$. However, setting $\alpha > 0$ allows the subtraction to be weighted towards low p_T tracks. In theory, this could provide a more accurate jet as higher p_T tracks are more likely to be true members of the jet. However, for this analysis, the recommended value is used for consistency with the FastJet implementation used in ALICE [66].

These distances are computed for the full list of particles and ghosts in the jet and then ordered from shortest to longest. The ghost particles are now also given a transverse momentum proportional to the mean background momentum density ρ,

$$p_{T,g} = A_g\rho, \tag{2.8}$$

where, $p_{T,g}$ is the momentum of the ghost particles, A_g is the area given to each ghost particle and ρ is the mean transverse momentum of the background.

After iterating through the list from smallest to largest $\Delta R_{i,g}$ for each particle and ghost, some comparisons are made. Suppose the transverse momentum of the particle is more significant than the transverse momentum of the ghost, $p_{T,i} > p_{T,g}$. In that case, the ghost is deleted, and the track's momentum is adjusted using the following equation,

$$p_{T,i} = p_{T,i} - p_{T,g}. \tag{2.9}$$

This reduces the particle's transverse momentum by the average background transverse momentum. On the other hand, if the ghost's momentum is greater than the particle's momentum, the real track is removed, and the momentum of the ghost track is adjusted to:

$$p_{T,g} = p_{T,g} - p_{T,i}, \tag{2.10}$$

This means that the process reduces the ghost's transverse momentum by the particle's transverse momentum. This process continues for all particles and ghosts in the jet until every track or every ghost is removed from the jet. Because of this approach, the constituent subtraction method does not affect the position coordinates of the jet in η and ϕ as the technique reduces the particles p_z component of momentum by the same factor as the p_T momentum. Once the process is completed, the total momentum subtracted from the jet is,

$$p_{T,subtracted} = \rho \times A_g \times N_g, \tag{2.11}$$

where N_g is the number of ghosts in the jet area.

Importantly, the total momentum subtracted from the event is not:

$$p_{T,subEvent} = p_{T,subtracted} \times N_{jets}, \tag{2.12}$$

since some of the jets that were clustered had momentum significantly less than $p_{T,subtracted}$, this will result in these jets being completely removed. It should be noted that in this case N_{jets} is the number of jets in a given event not the number of jets in all events. Since these jets are likely to be combinatorial jets resulting from clustering a large number of soft background particles together. The result is that the momentum subtracted from the event by removing these jets is less than $p_{T,subtracted}$. Thus, the overall momentum subtraction from the event is less than what would be suggested by equation 2.12.

2.5 Jet Tagging

It is sometimes essential to compare jets found with different parameters. Since jet finding is a non-unique procedure where different parameters can lead to different jets, a system is needed to tag different jets, which are likely from the same initial scatter, while being found separately. In order to do this, a jet-matching algorithm is developed, which can match any number of jets to each other.

There are three situations in which tagging is used in this analysis. The first is tagging between particle level and detector level Monte-Carlo (MC) data (for a more detailed explanation on what these levels are, see chapter 4). These data differ as the detector level MC is the particle level MC after being placed through a GEANT3 detector simulation. This has the effect of smearing the particles; thus, the jets will differ slightly between the two levels. Therefore, it is required to be able to connect the two for comparison.

The second use of tagging is to reject combinatorial jets. This is achieved by performing jet finding with the typical constituent cut $p_T > 0.15$ GeV/c and a second jet finding cut of $p_T > 4$ GeV/c. The second jet cut is used as a high-momentum core to tag these jets. This is because a jet with this substantial constituent cut is unlikely to be a combinatorial jet. Thus, any jet that cannot be tagged with a high momentum core jet can be discarded as a combinatorial jet.

The third situation where tagging is used in this analysis is to tag jets before background and post-background subtraction. In this case, the jet finding is carried out on Pb-Pb data directly and then for a second time after constituent subtraction has been performed. This allows a direct investigation of the effects jet finding has on the data.

The actual mechanism of jet tagging is performed by geometric matching. The distance between all the jets in an event is calculated in the η - ϕ plane and then compared. The jets that are closest together are then matched and given a tag in the software. It is also possible to require that the two jets share similar η and ϕ and $p_{T,\mathrm{jet}}$. This would be used to ensure an even closer match between jets. This is typically only used when comparing two samples of jets known to contain the same jets.

Chapter Three

Experiment

3.1 Introduction

The Large Hadron Collider (LHC) is the largest particle accelerator ever constructed. It is also the highest energy particle accelerator reaching a peak collision energy of $\sqrt{s} = 13.6$ TeV in proton-proton runs. The machine occupies a tunnel that was constructed in 1988 and was initially built for the Large Electron-Positron Collider (LEP) [70]. The tunnel itself is 26.7 kilometres in circumference and is a minimum of 50 metres underground at any given point and is still one of Europe's largest-ever civil engineering projects [71]. In 2001 LEP was decommissioned, and the LHC was built in its place.

3.2 History

The LHC has undergone a number of upgrades since it was first built. While there was a short initial run in 2009 at the injection energy of $\sqrt{s} = 0.9$ TeV, Run 1 reached the operational energy of $\sqrt{s} = 7$ TeV in 2010 [72]. Operations continued until early 2013, when the machine entered its first long shutdown period for two years while preparing for Run 2.

In 2015 Run 2 started, and the LHC began accelerating protons at $\sqrt{s} = 13$ TeV [73]. In 2018 Run 2 ended, and the second long shutdown began (slightly extended due tot he COVID pandemic) to enable a number of upgrades of the machine and experiments. Run 3 began on July 5th, 2022 with the LHC now reaching its highest energy of $\sqrt{s} = 13.6$ TeV. The run will continue until December 2025, when long shutdown three will begin to upgrade the LHC to the High-Luminosity LHC [74] as well as experiments. A layout of the accelerators and detectors at CERN can be seen in figure 3.1.

3.3 CERN accelerator complex

The LHC accelerates heavy ions as well as protons. However, the stages of acceleration are different for either type.

For pp collisions, the process starts at Linear Accelerator 4 (LINAC4), which accelerates negatively charged hydrogen up to 160 MeV. This accelerator was newly built for Run 3 and replaced the previous Linear Accelerator 2 (LINAC2), which had been used for 40 years, and Linear Accelerator 1 (LINAC1) before that. LINAC4 differs from previous generations as it adds an additional electron to hydrogen rather than stripping it away. This extra electron, along with its original electron, is removed during injection into the Proton Synchrotron Booster (PSB). The PSB is comprised of four superimposed synchrotron rings which are responsible for accelerating the protons from 160 MeV to 1.4 GeV for injection into the Proton Synchrotron (PS) as well as being passed to other low-energy experiments. The use of the PSB increases the number of protons that are accepted by the PS by a factor of 100, allowing higher luminosities [76].

For Pb-Pb collisions, the process begins quite differently. The process starts with a block of solid isotopically pure ^{208}Pb. A sample of this lead is heated until vapourised. It

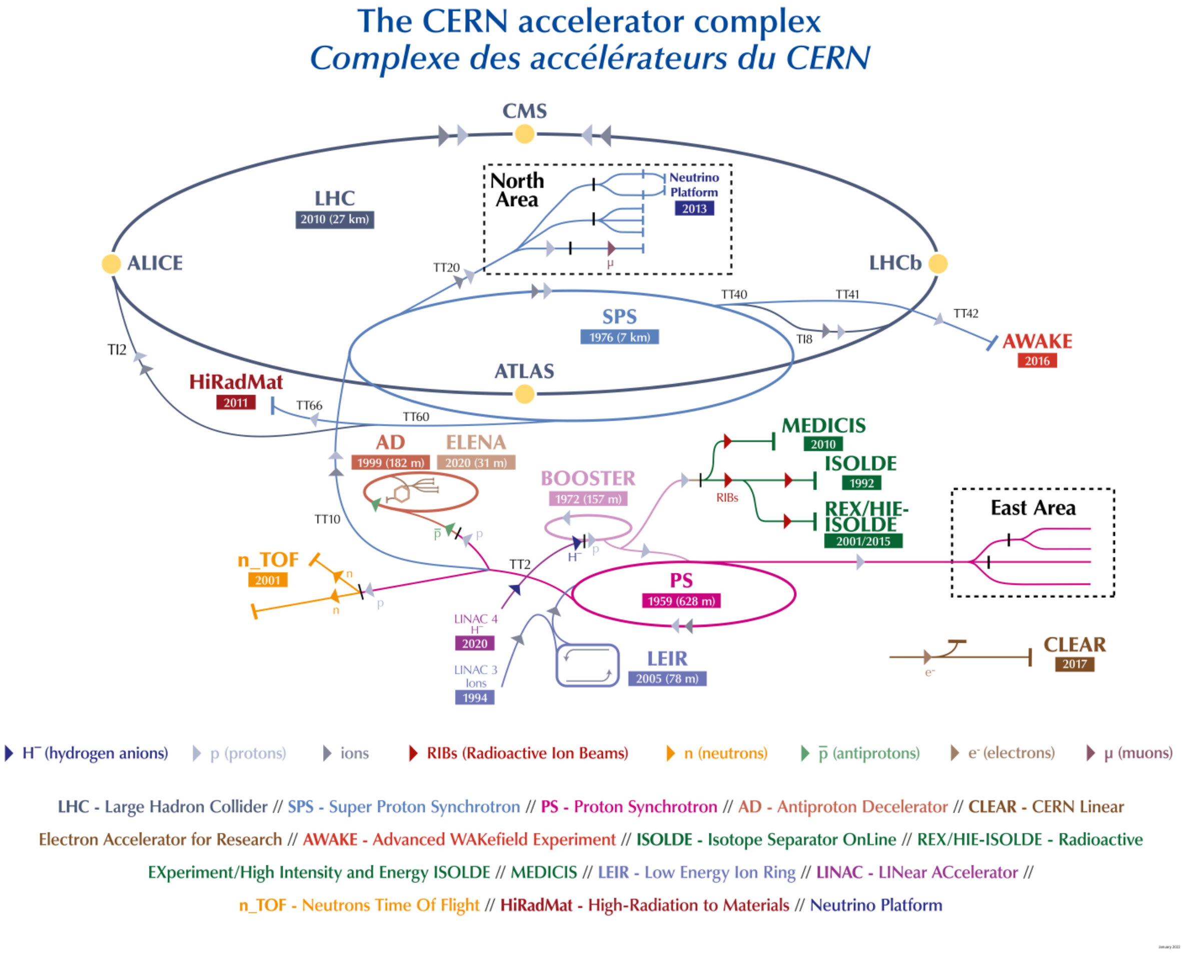

Figure 3.1: The figure shows the map of the CERN accelerator complex with the currently used accelerators as well as main detectors. Diagram taken from Ref [75].

is then ionised, stripping away the lead atom's electrons until they have all been removed and only the lead nuclei are left. This process is done by a series of fine filament strippers, which remove the electrons from lead atoms. These lead ions are then accelerated by bending magnets to select only lead ions that have had all their electrons removed. These lead ions are injected into Linear Accelerator 3 (LINAC3). Originally these ions were provided by LINAC 1. After the construction of LINAC 2, however, in 1994, a dedicated accelerator was built to provide a source of heavy ions to better study the QGP. It accelerates the ions up to 4.2 MeV for injection into the Low Energy Ion Ring (LEIR), where they are accelerated to a further 72 MeV. Originally it was called Large Energy Anti-proton Ring (LEAR) and designed to decelerate protons. However, in 1996, work to convert it to LEIR began, and it is now used to provide ions for detectors at the LHC [77].

The Proton Synchrotron (PS) was originally built in 1959 and was CERN's first synchrotron and, at the time, the highest-energy particle accelerator in the world. The PS, despite its name, can accelerate both heavy ions and protons and thus is where the processes for pp and Pb-Pb acceleration rejoin and continue in the same way from here. With a circumference of 628 m, the PS's primary purpose now is to accelerate particles up to 26 GeV to be fed into the Super Proton Synchrotron (SPS) [78]. The SPS, famous for being used to discover the W and Z bosons [79], is the final stage of acceleration before injection into the LHC rings. It is the second largest machine at CERN; it has a 7 km circumference and accelerates particles up to 450 GeV before they are injected into the LHC [80].

The LHC is a synchrotron which consists of two concentric rings held at a high vacuum through which hadron beams are accelerated in opposing directions. The machine is filled by the SPS with two beams. Each beam contains 2808 bunches of protons with 1.2×10^{11} protons per bunch. The beam is accelerated by 16 superconducting radio frequency (RF) cavities. These cavities use an electrical field to apply an impulse on charged particles that enter the chamber. These chambers are responsible for bringing the beams from an injection energy of 450 GeV to the maximum energy per beam of 6800 GeV. The fields inside the RF cavities oscillate with a frequency of 400 MHz. Because of this oscillation, the timing of a particle's arrival affects the relative strength of acceleration. The chambers are tuned such that a perfectly timed particle, and thus one with the desired energy, is not accelerated. Likewise, particles that arrive too early (therefore having too high energy) are decelerated towards the ideal and vice versa for late particles. It is this process that sorts the beam into groups of particles known as "bunches" [81].

In order to keep the particles within the beam pipe, their trajectories are bent by 1232, 15-meter-long dipole magnets. These magnets ramp up to a maximum of 8.3 T as the beam increases in energy. The dipole magnets are kept at an operating temperature of 1.9 K. The low temperatures are required to keep the magnets in a superconducting state, allowing them to handle the high electrical currents passed through the magnets required to provide the large magnetic field. To keep the beam highly collimated and prevent defocusing, 392 quadrupole magnets are used to manage corrections on the beam. Additionally, the dipole magnets themselves are equipped with sextupole, octupole and decapole components to help with this correction. [82].

As the beam is injected, the process of bringing it up to energy begins. As the energy increases and the magnets ramp up, if the beam falls outside of acceptable parameters, automated systems will cause the beam to dump. However, if all parameters are acceptable and the beam is brought up to full energy, then the stable beam will be magnetically adjusted at the four main collision points on the LHC such that the beams cross paths and collisions begin.

A Toroidal LHC Apparatus (ATLAS) [83] is located at point 1 of the LHC, which, alongside Compact Muon Solenoid (CMS) [84], was instrumental in the discovery of the Higgs Boson in 2012 [85] [86].

These two experiments serve as large general-purpose particle detectors at the LHC with similar capabilities providing the ability to cross-check results. ATLAS and CMS are optimised in different ways and use different detector technologies. This results in differing systems, thus, greatly enhancing the discovery potential of the LHC by having unique two general-purpose detectors.

Large Hadron Collider Beauty (LHCb)[87] is another major experiment on the LHC, which aims to study the differences between matter and antimatter by investigating the properties of the b quark. Rather than being a cylindrical detector, LHCb is built favouring the forward direction allowing them to focus on the particles which are at large rapidities.

Finally, A Large Ion Collider Experiment (ALICE) [33] is the detector at the LHC that this research uses. The ALICE detector is a general-purpose heavy-ion detector. These differ from pp collisions in two important respects: much higher multiplicity in head-on collisions and the potential creation of a QGP in the initial stages of the collision. The challenge of the much higher multiplicities created in heavy-ion collisions required the creation of a detector which specialises in dealing with these conditions. The creation of a QGP allows the study of the states of matter that existed in the moments after the Big Bang and is the primary area of research for the ALICE detector.

3.4 ALICE

The ALICE detector sits at point 2 of the LHC, 56 metres underground. At 26 metres long and 16 metres radially, the detector is the pinnacle of developments in heavy-ion collision detection [88]. Typically, these collisions are Pb-Pb collisions. However, Xe-Xe collisions have also been used. Because of the extremely high multiplicities in central Pb-Pb collisions, the ALICE detector was designed to measure approximately 4000 particles per unit rapidity.

The ALICE detector underwent a significant upgrade over Long Shutdown 2 in preparation for Run 3. However, since the work presented in this thesis uses data from Run 2, this section will only discuss the ALICE detector as it was during Run 2.

The ALICE detector is comprised of 18 subdetectors. Each of these detectors can function as a standalone detector. However, they are designed to be most effective when working together with the ALICE detector as a whole when coordinated by the Central

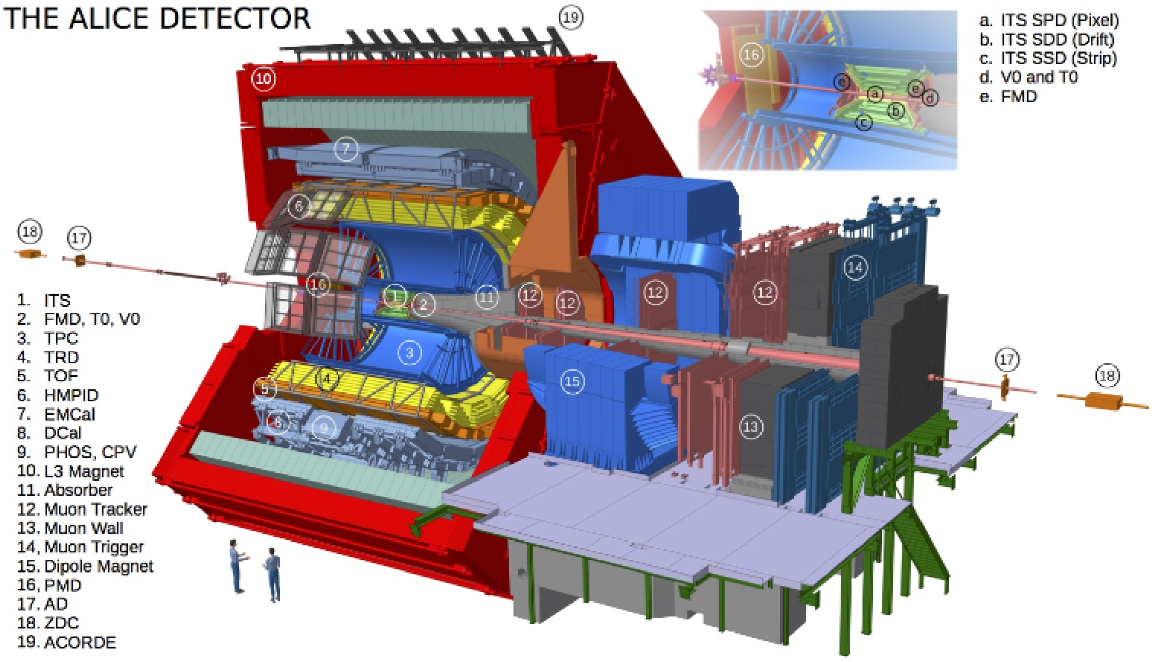

Figure 3.2: The figure shows a cross-section of the ALICE detector showing the composite subdetectors. Diagram taken from Ref [89].

Trigger processor (CTP). These subdetectors can be seen in figure 3.2. These subdetectors can be split into three groups based on location. These groups are the central barrel detectors, the forward detectors and the muon spectrometer.

3.4.1 Central Barrel

The central barrel detectors are enclosed within the main solenoid magnet providing a typical magnetic field of 0.5 T. The magnetic field selected is crucial for determining the p_T acceptance range of the detector, with ALICE's smaller magnetic field strength partially responsible for the sensitivity of the detector to low momentum tracks when compared to CMS. In order of increasing radial distance from the collision point, the detectors making up the inner barrel are:

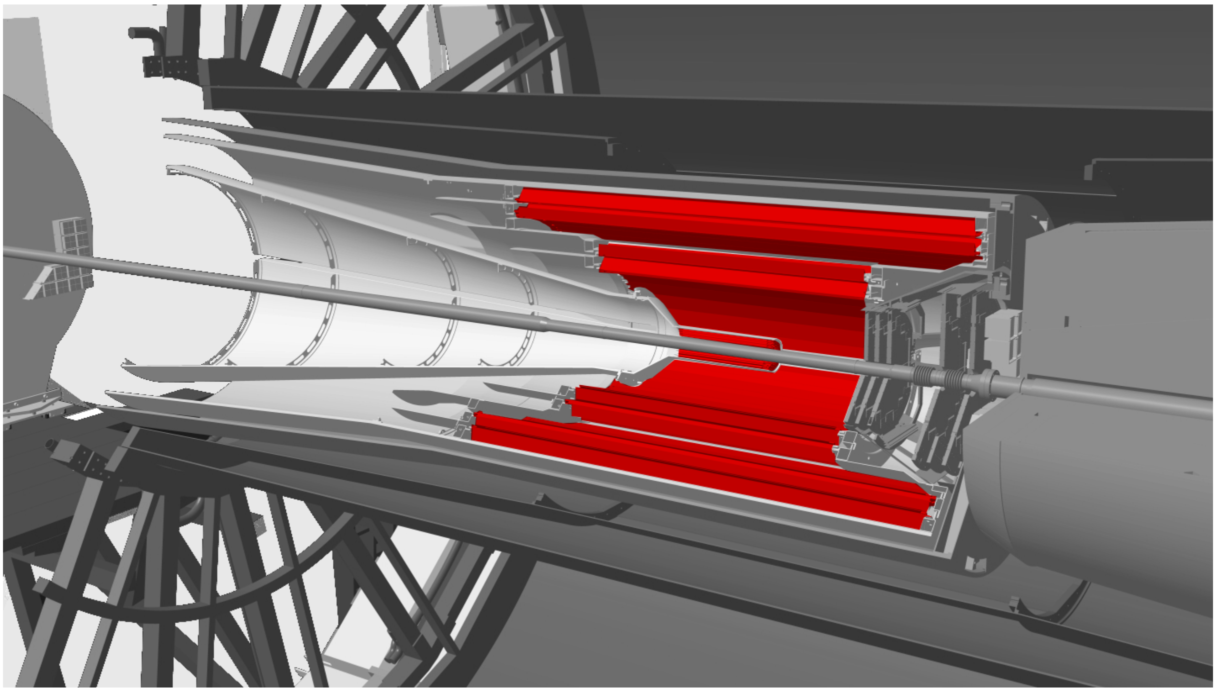

Figure 3.3: The figure shows the ITS as a red highlighted segment of the ALICE detector. Diagram taken from Ref [90].

- The Inner Tracking System (ITS) is the first detector encountered by particles emitted from the collisions [91] [92]. Its key role is to identify the primary and secondary vertices of the collisions, as well as provide initial tracking information and a degree of particle identification. It covers a pseudorapidity range of $-0.9 < \eta < 0.9$ and is cylindrical around the beam pipe. It is the only detector able to measure tracks with less than 100 MeV since the magnetic field prevents these particles from being measured by subsequent detectors. It is comprised of three sub-detectors, the Silicon Pixel Detector (SPD), the Silicon Drift Detector (SDD) and the Silicon Strip Detector (SSD) as seen in figure 3.3. Each of these sub-detectors is made up of two layers such that the ITS as a whole is composed of six layers. The SPD is the closest to the beam pipe and is comprised of approximately 10^7 cells measuring approximately 425 μm $\times$ 50 μm [93]. The SPD's large number of pixels is required to achieve the high angular resolution needed this close to the beam pipe. It is designed to resolve a track density of about

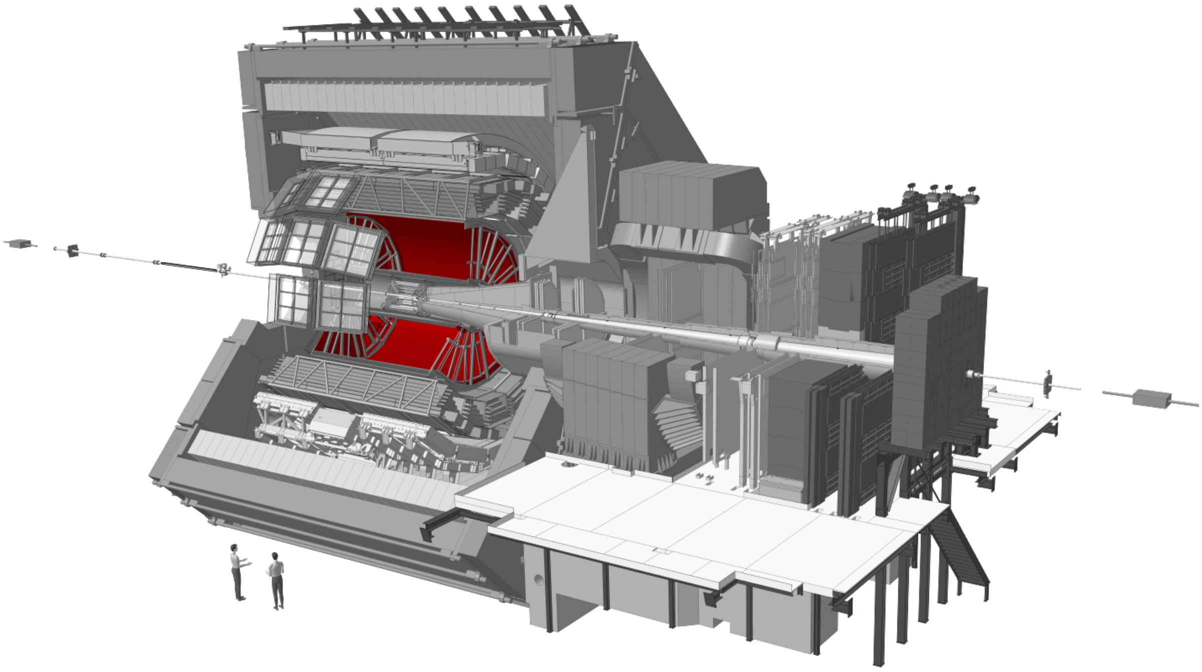

Figure 3.4: The figure shows the TPC as a highlighted segment of the ALICE detector. Diagram taken from [90].

90 cm^{-2}. While the SPD is comprised of individual pixels, the SDD is comprised of strips and thus only has a high segmentation in one direction. The SDD determines the position in the coarsely segmented direction using the drift time of the charge induced by the particles. Using this technique, the SDD achieves spatial resolutions smaller than 50 μm. The SSD is located furthest from the beam pipe, thus, is only required to deal with approximately 1 track per cm^2. Its primary function is to allow the correct correlation of tracks in the ITS to the TPC (see below). It completes this function by being a double-sided detector enabling a three-dimensional measurement of a track's position.

- The Time Projection Chamber (TPC) is the main barrel tracker of the ALICE detector [94] [95]. It is responsible for constructing the trajectory of charged particles and measuring their momentum. Alongside the TPC's tracking capabilities, it also performs particle identification. As standard for barrel detectors, it covers the pseudorapidity range of $-0.9 < \eta < 0.9$ with a cylindrical shape giving full azimuthal coverage. Alternatively, the TPC can allow for $-1.5 < \eta < 1.5$ coverage for tracks with a reduced length. The TPC covers an extensive range of transverse momenta from approximately 0.1 GeV/c to 100 GeV/c. The TPC is significantly larger than the ITS with an inner radius of 85 cm, an outer radius of 250 cm and a length of 5 metres. A diagram of the TPC can be seen in figure 3.4. It is separated into two chambers by a central cathode at −100 kV that provides a uniform electric field of 400 V/cm. As charged particles traverse the chamber, they leave a trail of ionisation. The electrons from these charged particles are accelerated towards the nearest endplate. This acceleration takes a maximum of 90 μs if the track is accelerated over the maximum 2.5 m. The endplates are used to detect the electrons from the ionised trail. The end plates determine the z-position of particles using the drift time. The remaining two positional coordinates are determined by the x-y coordinates of the charge arriving at one of the 18 sectors each end plate is divided into. Each of these sectors is covered with a multi-wire proportional chamber (MWPC) and a cathode pad readout. Taking advantage of these designs, the TPC can record 76 spatial points per track.

- The Transition Radiation Detector (TRD) is a detector designed to identify electrons with momenta greater than 1 GeV/c. The TRD also corrects for distortions of charged tracks measured in the TPC [96]. The TRD is a cylindrical detector with an inner radius of 2.9 m and an external radius of 3.68 m. The TRD has full azimuthal coverage and a slightly reduced pseudorapidity range $-0.84 < \eta < 0.84$. The detector is comprised of 522 chambers. Each of these chambers contains a 3 cm drift region filled with Xe/CO_2 mixed together. Additionally, these chambers are equipped with a radiator and a MWPC. These chambers are split into eighteen sectors, each further split into thirty chambers split into stacks of five longitudinally and six radially.

- The Time-Of-Flight (TOF) is a detector that measures the speed of particles by measuring the precise time for a particle to reach the TOF from the vertex. It is a cylindrical detector with an inner diameter of 3.9 m and a pseudorapidity coverage of $-0.9 < \eta < 0.9$. By using this precise measurement of the particle's speed, the TOF is able to be highly effective in particle identification. The TOF can identify pions and kaons between 0.5 GeV/c and 2.5 GeV/c and protons up to 4 GeV/c [97] [98]. The TOF is comprised of 1593 Multigap Resistive Plate Chambers (MRPC) in 18 azimuthal sectors. Each MRPC is split into ten gap chambers in two stacks. This allows the TOF to achieve a timing resolution of approximately 56 ps [99].

- The High-Momentum Particle Identification Detector (HMPID) is a detector that specialises in the identification of high-momentum particles [100]. It expands the momentum range of the particle identification of pions, kaons, and protons. It is comprised of a single arm proximity Ring Imaging Cherenkov (RICH) detector with full azimuthal coverage.

- The Photon Spectrometer (PHOS) is an electromagnetic calorimeter around the central barrel of the detector used to measure the energy of particles resulting from the collision [101]. However, unlike other barrel subdetectors, the PHOS does not have full azimuthal range coverage. The PHOS offers approximately 100° of azimuthal coverage. The PHOS modules are each composed of a lead tungstate crystal calorimeter and Charged Particle Veto (CPV) that suppresses the charged particle background [102].

- The Electromagnetic Calorimeter (EMCAL) is an electromagnetic calorimeter located around the central barrel designed to measure energy deposition [103]. Similar to the PHOS, the EMCAL lacks complete azimuthal coverage, instead covering approximately 107°. It is composed of a lead-scintillator sample. The EMCAL, along with the other calorimeters, allows jets to be studied as full jets rather than only sampling charged particles in the jets.

- The Di-jet Calorimeter (DCAL) is a third electromagnetic calorimeter located opposite the EMCAL since both the EMCAL and the DCAL lack full azimuthal coverage. Using both calorimeters in tandem is required to study energy from back-to-back jets. The DCAL, EMCAL, and PHOS are all evenly spaced around the barrel [104].
- A Cosmic Ray Detector (ACORDE) is a detector for cosmic rays which is located external to the solenoid magnet on top of the ALICE detector [105]. It is used to trigger the experiment on cosmic rays.

3.4.2 Forward Detectors

The forward detectors are much smaller than the central barrel detectors. They are located close to the beampipe and in the forward pseudorapidity direction. The sub-detectors that make up this group are as follows:

- VZERO (V0) is comprised of two scintillator arrays, V0A and V0C. V0A is positioned 340 cm from the front side of the ALICE detector, and the V0C is located on the front face of the muon absorber. Together they serve the purpose of selecting the minimum bias events. The V0 can also be used to veto online triggers in ultra-peripheral collisions as well as to complement the muon spectrometer's detector capabilities. Each of these scintillators is composed of four rings with eight elements leading to a total of 32 elements. These rings and elements vary in size to maximise pseudorapidity coverage. The pseudorapidity range covered by the V0A and V0C are $2.8 < \eta < 5.1$ and $-3.7 < \eta < -1.7$ respectively. Each element is equipped with a 12-bit analogue-to-digital converter with a voltage tuned to have 15 counts for a Minimum Ionising Particle (MIP), corresponding to 2 kV in pp and 1.5 kV in Pb-Pb collisions due to the higher multiplicities [106].

- The TZero (T0) are two arrays of twelve Cherenkov counters which can be used to provide an alternative measurement to collision time when compared to the TOF.
- The Alice Diffractive detector (AD) [107] are two sets of scintillator pads split into four sections located on either side of the ALICE detector. On the A side of the detector, the ADA is located 17.5 m from the collision point with a pseudorapidity coverage of $4.7 < \eta < 6.3$. On the C side, the ADC side is located 19 m from the collision point and covers a pseudorapidity range of $-6.9 < \eta < -4.9$.
- The Forward Multiplicity Detector (FMD) is a detector composed of 5 rings of silicon strip detectors designed to measure the charged particle multiplicity at increased pseudorapidity ranges [108] [109]. One ring of the FMD is located on the C side of the detector and covers a pseudorapidity range of $-3.4 < \eta < -1.7$. The remaining four rings are located on the A side of the detector and cover the pseudorapidity range of $1.7 < \eta < 5.0$.
- The Photo Multiplicity Detector (PMD) is a detector designed to measure the multiplicity of photons in a collision. The PMD is composed of two arrays, each split into 24 modules, each module then split into a further 576 hexagonal chambers [110]. It is located on the A side of the detector and provides a pseudorapidity coverage of $2.3 < \eta < 3.7$.
- The Zero Degrees Calorimeter (ZDC) is made of two calorimeters located 112.5 metres away from the detector in both directions designed to measure the energy deposition at high magnitude pseudorapidities. The ZDC produces the minimum bias event selection, provides measures of the centrality of the collisions and provides the absolute luminosity of an event [111].

3.4.3 Muon Spectrometer

A large section of the ALICE detector is the Muon Spectrometer. The Muon Spectrometer is located in the forward direction, making it sensitive to muons from the decay of charm and bottom quarks. Its location allows detection of collisions products in the pseudorapidity range of $-4.0 < \eta < -2.5$ at low p_T [112]. The main components of the muon spectrometer can be seen in figure 3.5 and include the following:

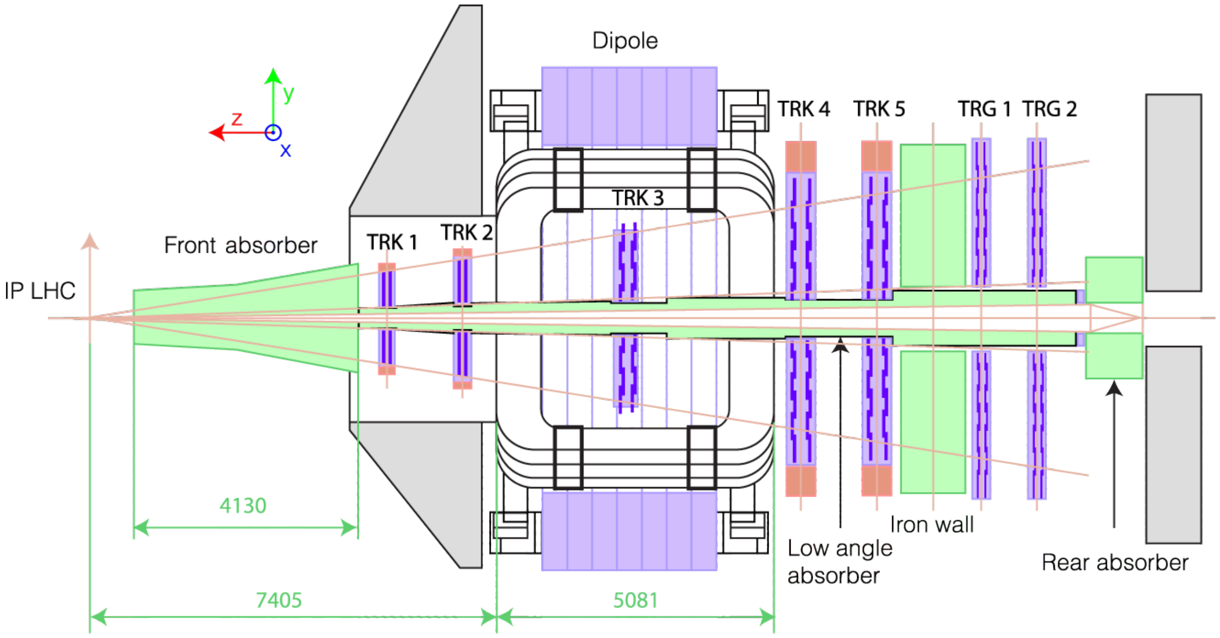

Figure 3.5: A schematic diagram of the Muon Spectrometer of the ALICE detector taken from [113].

- There are three absorbers that form part of the Muon Spectrometer, each serving a different role. The three absorbers are the front absorber, the beam shield and the muon filter. The front absorber is designed to remove any remaining hadronic scattering at forward rapidity as well as mitigate the backscattering into the central barrel. The front absorber is four metres long and located 90 cm from the interaction point such that it is positioned to ideally absorb hadronic scattering. It is made of three components, the inner shield, the central core and the outer shield. The inner and outer shields are made of high atomic number materials, namely steel, tungsten and lead. Conversely, the central cone is composed of low atomic number materials, namely concrete and carbon. This is to limit scattering. However, the section of the central cone nearest to the muon spectrometer is made of heavier lead and tungsten to limit backscattering, such as with the inner and outer shields. The beam shield surrounds the beam pipe and is constructed from high atomic number materials. It shields the spectrometer from particles produced in various forward rapidities and secondary particles. Finally, the muon filter is located between the trigger and tracking chambers and shields the forward muon spectrometer's trigger chamber.

- The Dipole Magnet provides the 0.7 T magnetic field to the muon spectrometer since it is located outside of the solenoid magnet. This magnetic field is required to measure the momentum and charge of particles in the spectrometer [114] [115].
- The Muon Tracker is the section of the muon spectrometer that tracks particles. It is comprised of five panels labelled as TRK in figure 3.5. Two of these tracking panels are located before the dipole magnet, one within the dipole magnet, and two after the dipole magnet.
- The Muon Trigger is responsible for selecting events based on when a muon is detected above a p_T threshold. It is composed of two trigger panels located at the back of the muon spectrometer. Each trigger panel is comprised of two layers of 18 Resistive Plates Chambers (RPC). The timing resolution of these panels is less than 2 ns.

3.4.4 The ALICE Trigger

Similar to the ALICE detector, the ALICE trigger system received a complete upgrade during Long Shutdown 2 in order to prepare the experiment for Run 3 [116]. This section will focus on the trigger system used during Run 2. The Run 2 Trigger system is made up of one Central Trigger Processor (CTP). The CTP itself is composed of eleven 6U VME boards. The CTP works in concert with 24 Local Trigger Units (LTU), which connect the CTP to subdetectors to provide the overall trigger system for the ALICE detector [117].

The CTP can distribute four different trigger levels, namely, LM (level minus), L0, L1, and L2, to the LTU of each subdetector. These different trigger levels differ in the latency of each signal. The LM trigger level has the shortest latency at 650 ns; this allows this trigger level to be used as a wake-up trigger to be sent to the TRD. The L0 trigger level has a latency of 900 ns and then 6.5 μs for L1 and 88 μs for L2.

The LTU connect to the subdetectors by integrating with the Front-End Electronics (FEE) of each subdetector. The LTU are responsible for transmitting the L0 signal to the subdetector via LVDS cables, while L1 and L2 triggers are sent by the Trigger and Timing Control system. The LTU have the ability to operate in concert with the CTP allowing for a global run. However, individual LTU can also emulate the CTP internally and thus run independently. This standalone mode can be useful for debugging systems, testing new detector configurations or running individual subdetectors for triggering on cosmic rays.

The CTP logic is responsible for identifying trigger classes and sending the corresponding signal to a detector cluster. A class is a series of inputs into the trigger system which are defined and correspond to a specific signal. A cluster is a group of subdetectors which are triggered in tandem due to similar readout times. Clusters are not exclusive; therefore, a given subdetector can belong to several classes.

Once the FEE has received a trigger from the connected LTU, a signal is sent to the DAQ Readout Receiver (D-RORC) cards using the Detector Data Links (DDL). These D-RORC cards are connected to Local Data Concentrators (LDC) that combine the data received from each DDL in order to compile the information from each detector into a sub-event. The sub-event is then transferred to the Global Data Collectors (GDC) for the final assembly of each sub-event into a full event.

Chapter Four

Data Selection and Unfolding

4.1 Monte-Carlo Generation

One of the key tools used in particle physics is simulated data. Simulating data using a set of current known physical predictions and then comparing these simulated data to measured data allows the quality of the predictions to be assessed. Additionally, the comparison enables the search for any features in the measured data that are not in the simulated data. These features could be evidence of mechanisms not being simulated.

Simulated data are generated using a Monte-Carlo (MC) generator. These types of generators use the MC method to randomly sample numbers to simulate events. In cases where the physics is well described, it is simple enough to calculate the underlying process. However, when the physics is not well defined, the generator uses numerical models to determine the outcome of the probability distributions. These numerical models are created by using measured data.

The three main sections of the event that can be handled by a MC generator are the initial collision, the parton shower and hadronisation. There are several different MC event generators which exist, and within these generators are different tunings to affect the internal parameters. These generators differ in the precise details and methods used to simulate events. The main event generator used in this analysis is PYTHIA [118]. The POWHEG event generator [119] is also used; however, this is limited to an investigation of the choice of generator on the jet yields in section 5.5.

PYTHIA8 is the main MC event generator used in this analysis. PYTHIA is one of the most complete particle event generators and is able to handle all three steps of the event generation, from the initial collision to hadronisation. PYTHIA8, alongside its older version PYTHIA6, is the main event generator used by the Jet Physics Working Group in the ALICE collaboration. POWHEG is an MC event generator which simulates next leading order corrections to the event, which are not considered in PYTHIA. This added complexity leads to the POWHEG generator being considerably more computationally expensive than the PYTHIA generator. Additionally, the POWHEG event generator is not designed to simulate the parton shower or the hadronisation process. Instead, it is used in tandem with another generator to complete these processes. In this analysis, when POWHEG is used, the parton shower and hadronisation are then simulated by PYTHIA6.

4.1.1 The Particle and 'detector level's

While MC generators provide an excellent tool for analysis, the ability to use these events to compare to measured data are limited if the detector effects are not also simulated. This is because any differences between the MC data and the real data could be introduced due to detector effects instead of a difference in the underlying physics. Therefore, the GEANT3 [120] software is used to simulate these detector effects. GEANT3 is software that simulates the passage of particles through matter. A replica of the ALICE detector is constructed within the software, and the effects that the detector will have on the generated MC event are then simulated. This should allow for the generated MC event to be compared to the measured data.

The introduction of these simulated detector effects means that the MC events now exist at two separate levels, ‘particle level’ and a ‘detector level’. The ‘particle level’ contains all information in the events, including information relating to partons and is the direct output of the MC simulations. The ‘detector level’ is the result of inputting the ‘particle level’ information through a GEANT3 simulation of the ALICE detector. Thus, the ‘detector level’ should represent the output seen from the ALICE detector.

4.2 Data Selection and Cuts

This analysis uses five sets of data, all from the LHC Run 2 (2015-2018) or from generated MC data anchored to the Run 2 period. These are listed in full in table 4.1. For pp collisions, there is a Run 2 data set, LHC17q, which are data measured from the ALICE experiment and a set of MC data, LHC18b8, used to generate the jet charge distributions. There are two additional data sets for Pb-Pb collisions, LHC18q and LHC18r. These data are from Run 2 and are used to measure jet charge in data and used as the background during embedding. Finally, the MC data set LHC19f4 for Pb-Pb are PYTHIA-generated pp data anchored to the LHC18q and LHC18r run periods to be embedded into these events.

These data are already pre-screened by the ALICE Collaboration Data Preparation Group to ensure that they are of good quality and that none of the detector systems had issues. This occurs before the data are qualified for analysis to minimise systematic issues with the data. Additionally, the data are run through the ALICE framework system of filter bits with bits $(1 << 8)|(1 << 9)$. These filter bits are specific tags on each track that correspond to specific cuts made when accepting the tracks to ensure good quality. The

Table 4.1: The table shows the data sets used during this analysis. There are three real data sets. These data sets are used for the jet charge distributions to be fitted. Both Pb-Pb data sets are combined in this process. There are additionally two MC data sets. These are used to generate the distributions. In the case of the LHC19f4 data set, this is done by embedding into the two collisions Pb-Pb data sets.

Run Period	Collision System	Data Type	N_{Events}
LHC17q	pp @ 5.02 TeV	Real Data	83,305,431
LHC18b8	pp @ 5.02 TeV	MC	110,743,600
LHC18q	Pb-Pb @ 5.02 TeV	Real Data	393,046,648
LHC18r	Pb-Pb @ 5.02 TeV	Real Data	487,195,587
LHC19f4	pp @ 5.02 TeV	MC	196,886,750

filter bits are standard for the data sets chosen, and it is important to use them to avoid double-counting tracks.

There are still additional selections and cuts to the data that need to be performed. The events are selected for a given trigger set in the software correlated with a hardware trigger. The tag "kINT7" handles the software trigger in the analysis. This means that events are required to meet the minimum bias and V0 triggers. The minimum bias trigger is designed to reject background effects from the beam while selecting inelastic events with minimum physics bias. In pp collisions at least one track is required in the V0A, V0C or the SPD. In Pb-Pb collisions two tracks are required [121].

There is a general track p_T cut of 0.15 GeV/c, which is the minimum track p_T for the ALICE detector.Moreover, the tracks considered are limited tracks from charged particles only. While the ALICE detector can measure neutral particles using the EMCAL subdetector, using this subdetector considerably limits the overall detector acceptance. This limitation, combined with the nature of the jet charge, means that only charged particles are considered during jet reconstruction in this analysis.

A minimum $p_{T,\mathrm{chJet}}$ cut is used at the jet-finding stage. This cut is set to 20 GeV/c, which sets the jet above the background level of soft particles and aims to minimise the effects of these particles. This corresponds to the background seen in Pb-Pb collisions, and thus a cut below this would be dominated by combinatorial jets.

An additional cut on the jet at the final stage requires that the jet has a leading track $p_T > 5$ GeV/c. This cut is used to mitigate the number of combinatorial jets from the background, as it requires the jet to contain at least one hard track.

The jet-finding algorithm also includes an acceptance check to ensure that it only includes tracks within a certain geometry. In this analysis, the accepted geometry is stated as "kTPCfid", which requires the entire jet to fall within the TPC acceptance range. This manifests in cuts in pseudorapidity. The standard ALICE barrel detector acceptance is $|\eta| < 0.9$. Thus, the jet must not fall outside of this acceptance range. This places a new cut on the jet that requires $|\eta_{\mathrm{jet}}| - R < 0.9$, in the case of this analysis for jets with $R = 0.4$ this means $|\eta_{jet}| < 0.5$.

Finally, the Pb-Pb data are separated into different centrality bins. From $0 - 90$ % in 10 % increments, allowing the QGP's effects to be investigated with increasing centrality.

4.3 Unfolding

The ALICE detector provides a set of powerful tools to probe into the nature of fundamental particles, but the detector cannot provide a snapshot of the physics without being affected by the detector biases. This bias is because each element of the detector has specific efficiencies which are p_T dependent. Thus, without accounting for these effects, generated MC events will never accurately match the data measured from the detector.

Simulating the detector effects in MC data allows the comparison between MC with detector-simulated effects directly with the data measured from the ALICE detector. This comparison is valid but of limited utility because the results from analysing the data are limited to what the ALICE detector measures rather than representing true physics. Therefore, a technique to go from the 'detector' to the 'particle' level in real data is required. The technique used to accomplish this is called unfolding. Unfolding can be viewed as the inversion of detector effects on real data. This is visually represented in the diagram in figure 4.1.

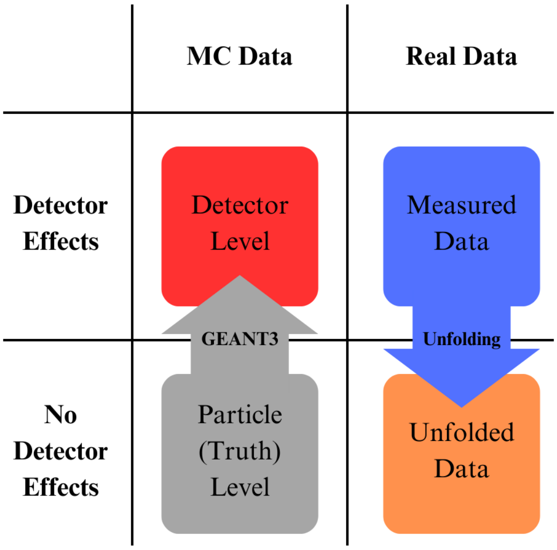

Figure 4.1: The diagram shows the different data levels of both MC data and real data. These are separated into 'with detector effects' and 'without detector effects' and the mechanisms to translate between data levels.

Unfolding is a technique that allows the data to be adjusted to account for detector effects on the measured characteristics of particles such as p_T. The software used to handle this is called RooUnfold [122]. Unfolding works by performing deconvolution on the data by using a response matrix. This response matrix is created using particle-level and detector-level MC events. With 1D unfolding, this response matrix is a 2D matrix with the detector and 'particle level' jet charge being the x and y axis, respectively. A more complex approach is 2D unfolding. In 2D unfolding, the response matrix is a third-order tensor with the jet charge and the $p_{T,\mathrm{chJet}}$ which deconvolutes both variables simultaneously. This 2D deconvolution is necessary as $p_{T,\mathrm{chJet}}$ is highly susceptible to detector effects; thus, unfolding both variables simultaneously better accounts for the detector effects.

The first step in the unfolding process is to extract both jet charge distributions and $p_{T,\mathrm{chJet}}$ distributions for the measured data and the MC data for both detector and 'particle level's. A response matrix is created using the 'detector level' and 'particle level' MC data. This response matrix is seen in figure 4.2. The response matrix is used to deconvolute 2D histograms of jet charge and $p_{T,\mathrm{chjet}}$. Firstly, the response matrix is applied to the MC data to ensure closure.Closure being a method to determine the consistency of the method. This closure is from applying the response matrix to the 'detector level' MC data, which should return the 'particle level' MC data. Dividing this unfolded MC data by the original 'particle level' MC data should return unity. This is seen in figure 4.3. Once this has been checked, the response matrix is applied to the data. This application allows the experimental data to be unfolded to account for detector effects, as seen in figure 4.4. For a visual comparison of how the unfolding affects the data, compare figure 4.5, showing the data before unfolding, to figure 4.4 showing the data after unfolding. The newly unfolded real data are now able to be compared directly to the 'particle level' MC data allowing the fitting to extract real physics.

The Bayesian unfolding method requires the specification of a so-called regulation parameter for the unfolding. In this case, the regulation parameter is the number of iterations of the unfolding process. Since the process converges rapidly, it is recommended that a small number of iterations is selected [123]. This has the benefit of saving computational time, as well as reducing the statistical error on the process as this increases with the number of

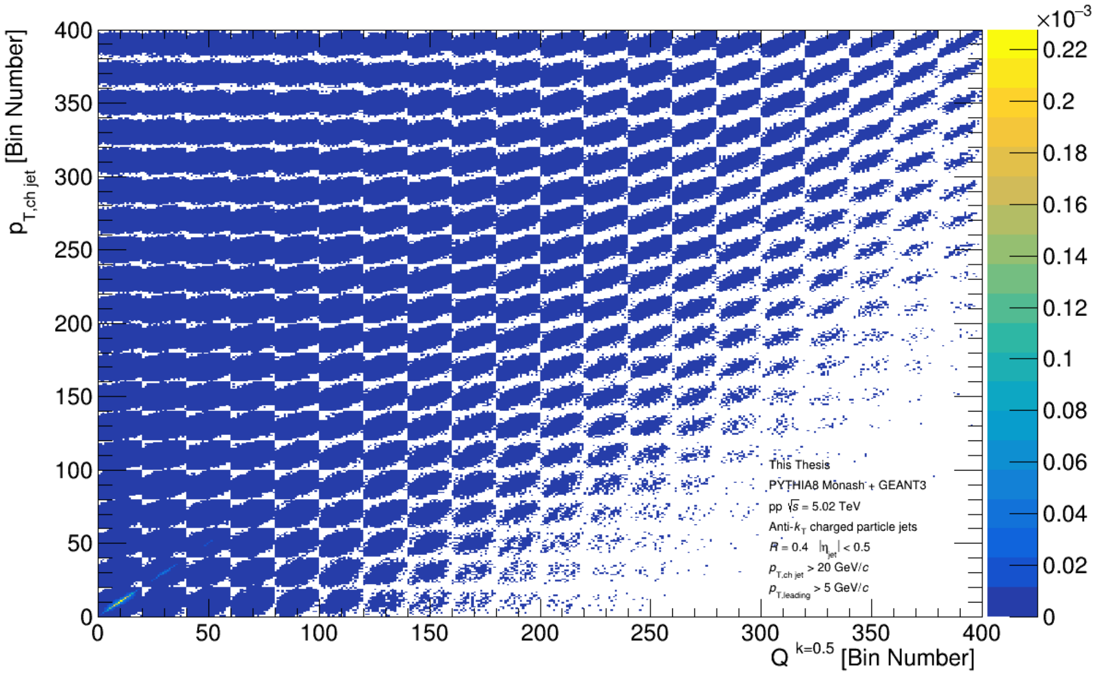

Figure 4.2: The flattened three-dimensional response matrix in a two-dimensional histogram. This graph can be viewed as a series of graphs along the X and Y axis as a whole comprising the ‘detector level’ jet charge and $p_{T,\mathrm{chJet}}$ respectively. However, within this, every 20 bins represent a separate ‘particle level’, $p_{T,\mathrm{chJet}}$ and jet charge two-dimensional histogram. The more diagonal this matrix is, the closer the ‘detector level’ follows the ‘particle level’.

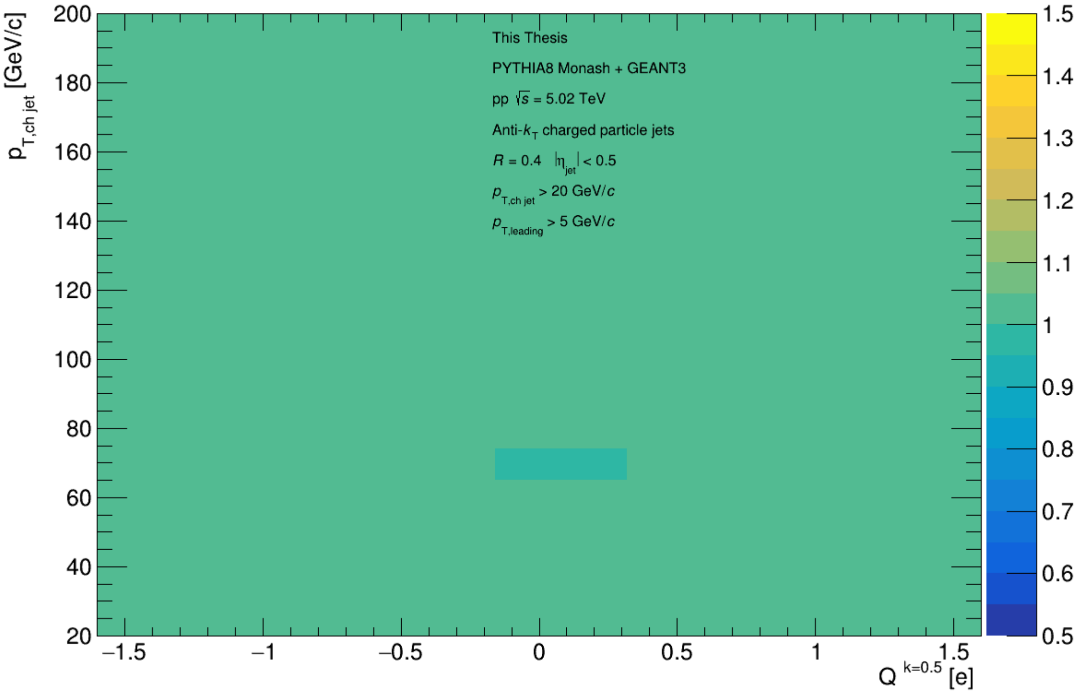

Figure 4.3: A two-dimensional histogram showing the MC closure by using the unfolding to go from ‘detector level’ to ‘particle level’ MC data. This histogram has been normalised by dividing it by the original ‘particle level’ MC data for a simpler comparison to unity. Note the colour change by 1 bin in the central region. This is a consequence of floating point errors in the graphing software rather than a discrepancy.

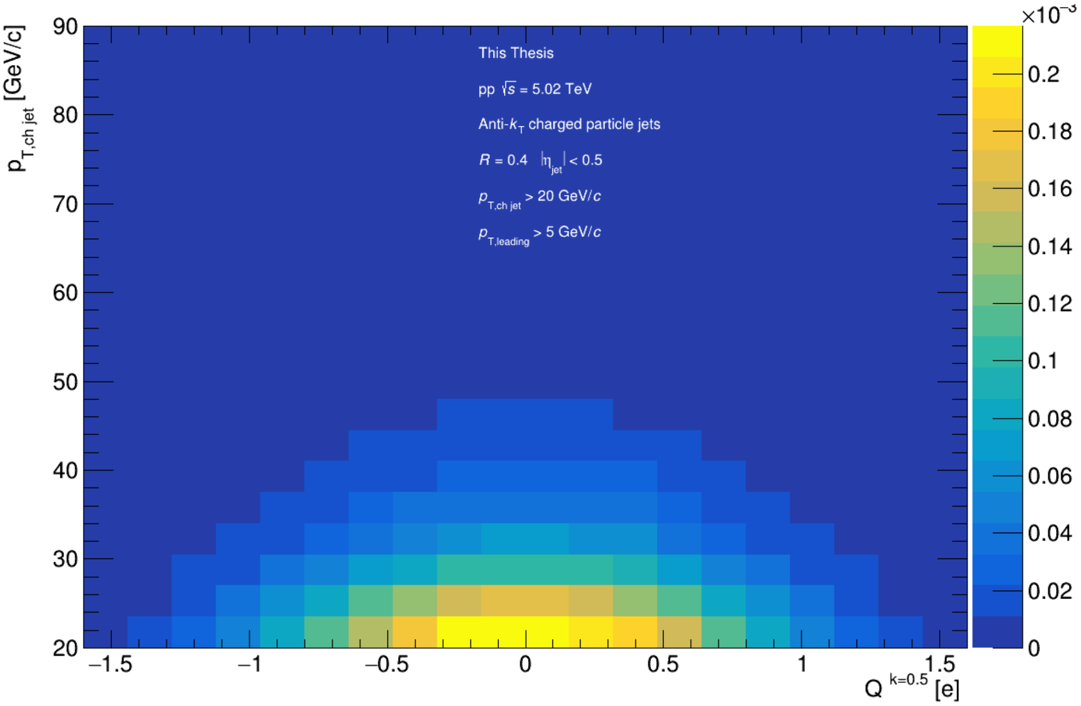

Figure 4.4: A two-dimensional histogram showing the measured $p_{T,\mathrm{chJet}}$ and jet charge distribution after unfolding.

iterations. The process for finding and selecting a regulation parameter is based on when the overall difference between iterations is smaller than the total error. This is seen in table 4.2, where the regulation parameter is set at 2.

The measured data are plotted, which results from calculating the jet charge directly from the ALICE detector's measured events. These are not unfolded and are shown in comparison to the particle and 'detector level' MC in figure 4.6. Finally, there are the unfolded data, which result from unfolding the $p_{T,\mathrm{chJet}}$ and jet charge measured in the real data and should partially mitigate the detector effects. Thus, unfolded data are compared to the 'particle level' MC data. For the sake of simpler comparisons to follow in the rest of this work, the comparisons are made between the projection of the jet charge axis of the 2D histogram rather than the histogram as a whole.

Figure 4.7 shows the same level splitting but this time for Pb-Pb instead of pp. By

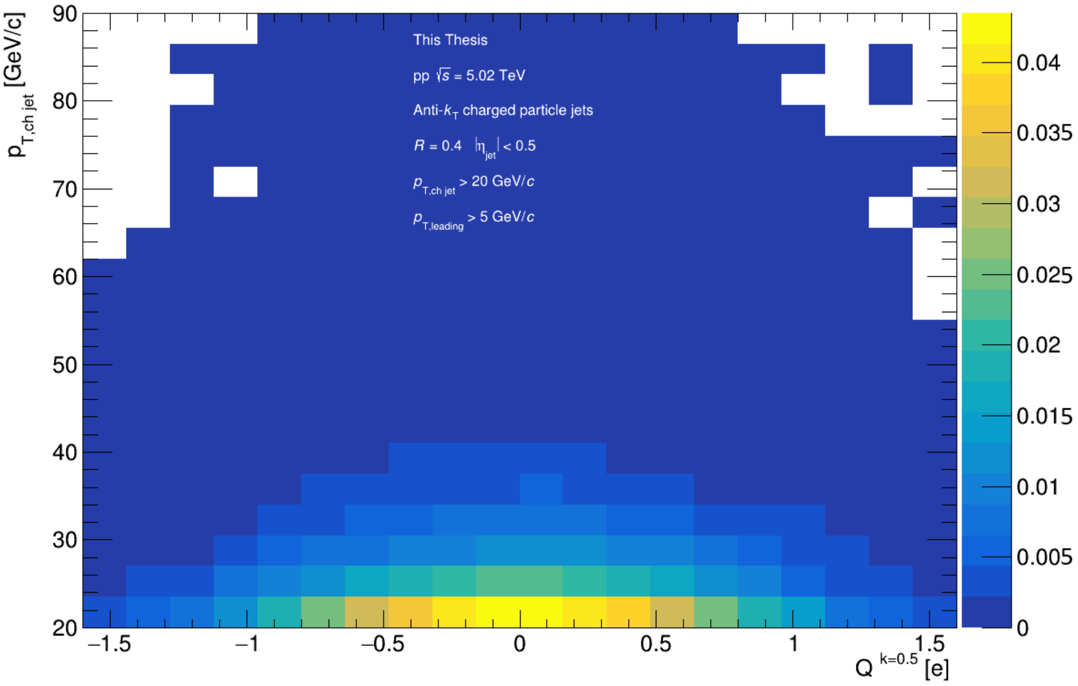

Figure 4.5: A two-dimensional histogram showing the measured $p_{T,\mathrm{chJet}}$ and jet charge distribution before unfolding.

Table 4.2: The table shows the values for the summed difference between the 2D histograms of jet charge and $p_{T,\mathrm{jet}}$ for successive regulation parameters as well as their summed error. The summed statistical error is already significantly larger than the difference between the successive iterations. Thus, the regulation parameter of 2 is picked. This summed error starting so high suggests that the detector effects on the jet charge and $p_{T,\mathrm{jet}}$ are significant.

Regulation Parameter	Unfolding Differences	Total Error
2-1	0.00245244	0.0386367
3-2	0.00168376	0.049193
4-3	0.00135737	0.0564227
5-4	0.00105685	0.0619721

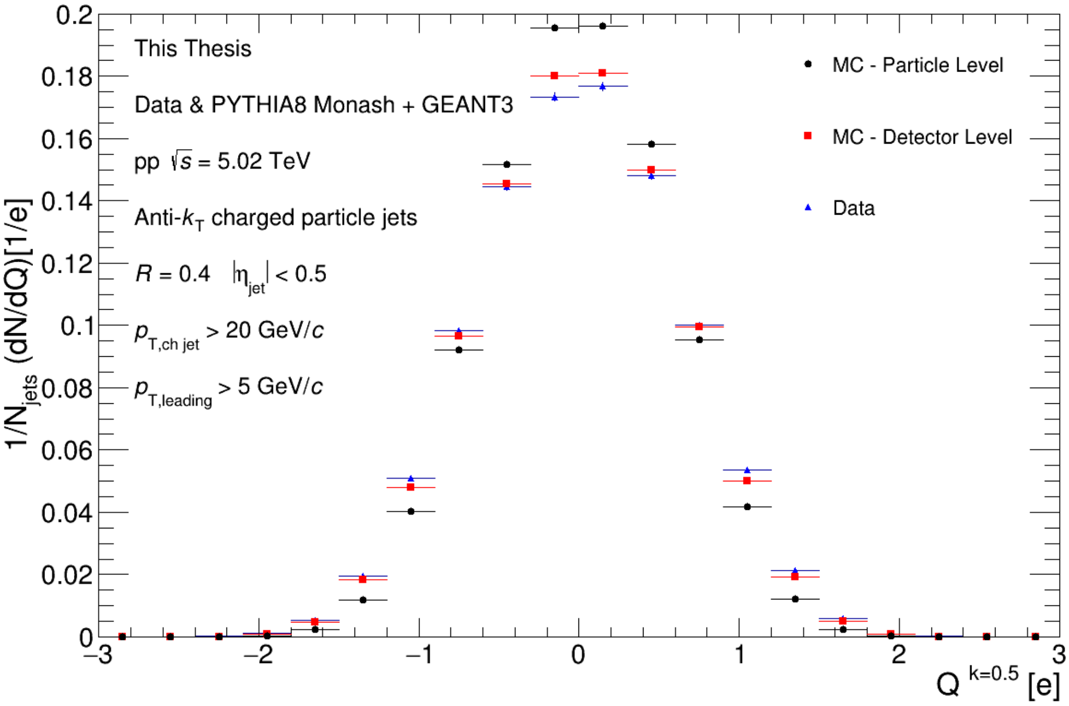

Figure 4.6: Normalised jet charge distribution measured with the ALICE detector in pp collisions at $5.02 TeV$ (blue) compared to the corresponding 'particle level' (black) and 'detector level' (red) MC data. Note there is no unfolded data shown in this histogram. See equation 1.7 and text for details.

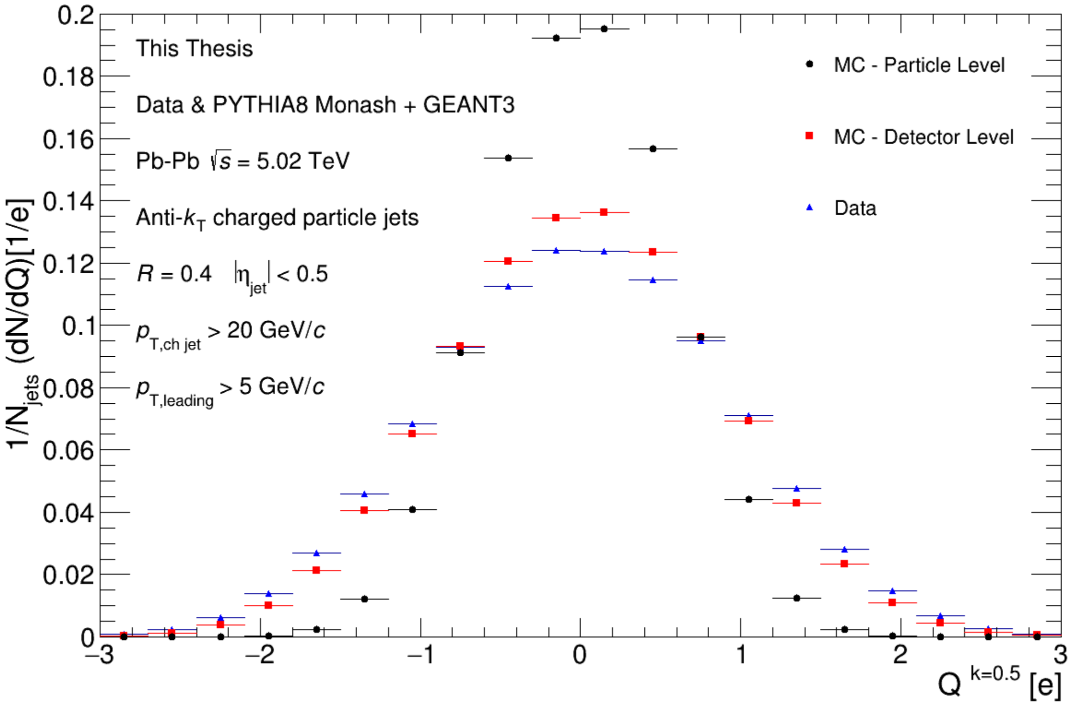

Figure 4.7: Normalised jet charge distribution measured with the ALICE detector in most central (0-10% centrality) Pb-Pb collisions at 5.02 TeV (blue) compared to the corresponding 'particle level' (black) and 'detector level' (red) MC data. Note there is no unfolded data shown in this histogram. See equation 1.7 and text for details.

comparing figures 4.6 and 4.7, it is clear that while the 'detector level' and the data are not in full agreement, they share a general trend of being wider than the 'particle level' distribution. This effect is particularly pronounced in the Pb-Pb events, where the data level is significantly narrower than the MC would suggest.

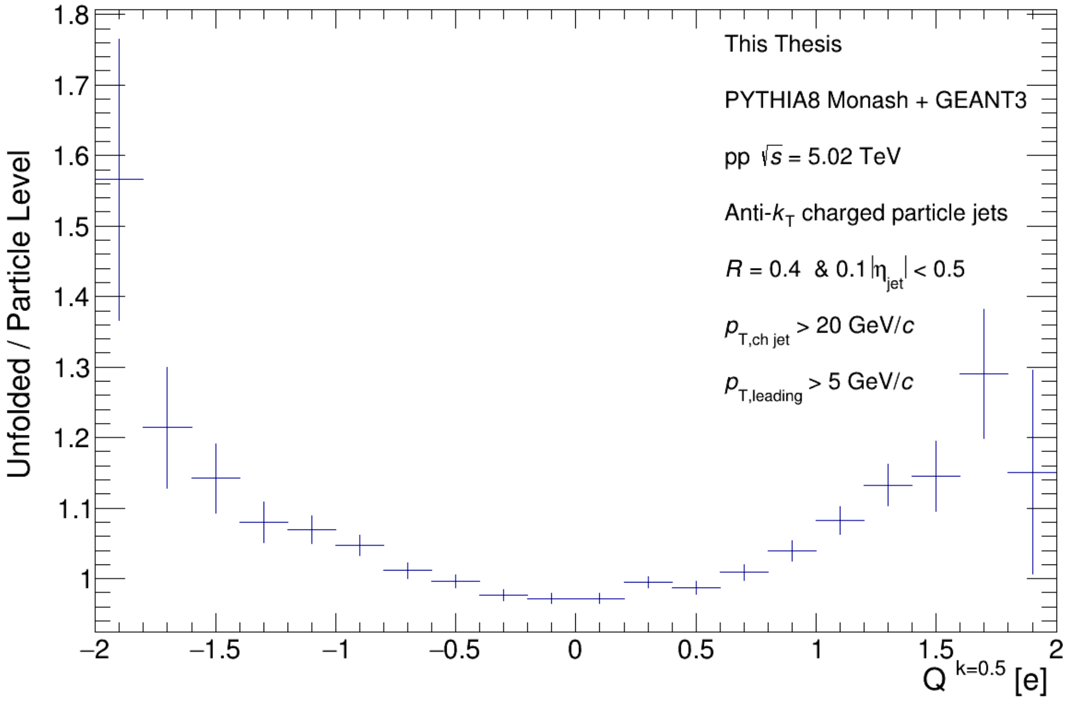

Figure 4.8: The figure shows the ratio between the unfolded measured jet charge and the particle-level MC data jet charge. By examining this ratio, it is possible to see the effect of the unfolding on the data. This is shown for 5.02 TeV pp collisions.

As seen in figure 4.8, the unfolding does go some way to translating the data to the 'particle level' MC data. However, there is a larger discrepancy between unfolded data and the 'particle level' at the ranges larger than $|Q| > 1.6$. Additionally, the upward trend in the ratio at the extremities shows that the unfolded data are wider than the 'particle level' MC data. As a result of this spread, the fitting will be done within the range $-1.6 < Q^{k=0.5} < 1.6$ e for the jet charge.

Chapter Five

Jet Charge

5.1 Introduction

The jet charge is the momentum-weighted sum of the electrical charges of the tracks that make up the jet. It is defined in equation 1.7 and repeated here for clarity,

$$Q^k = \frac{1}{(p_T^{\text{jet}})^k} \sum_{i \in \text{jet}} q_i (p_T^i)^k, \tag{5.1}$$

where Q^k is the jet charge, p_T^{jet} and p_T^i are the transverse momenta of the jet and track, respectively, and q_i is the electrical charge of the jet constituent. The parameter k is a scaling power that affects how sensitive the jet charge is to the charge of the individual tracks in the jet depending on their momenta. Higher values of k enhance the jet charge's sensitivity to high momentum tracks, and lower values of k reduce this sensitivity. The value of $k = 0.5$ has been suggested to produce a jet charge that is most heavily influenced by the jet's progenitor parton [44]. This value was therefore used in this analysis.

The jet charge is weighted to favour higher momentum tracks over their low momentum counterparts. This is because these high-momentum tracks are more likely to be closely associated with the scattered progenitor parton as they constitute a significant fraction of the momentum of the initial hard scatter. These particles are also more separated from the lower momentum random background particles, which may have been clustered into the jet despite not being part of the initial hard scatter.

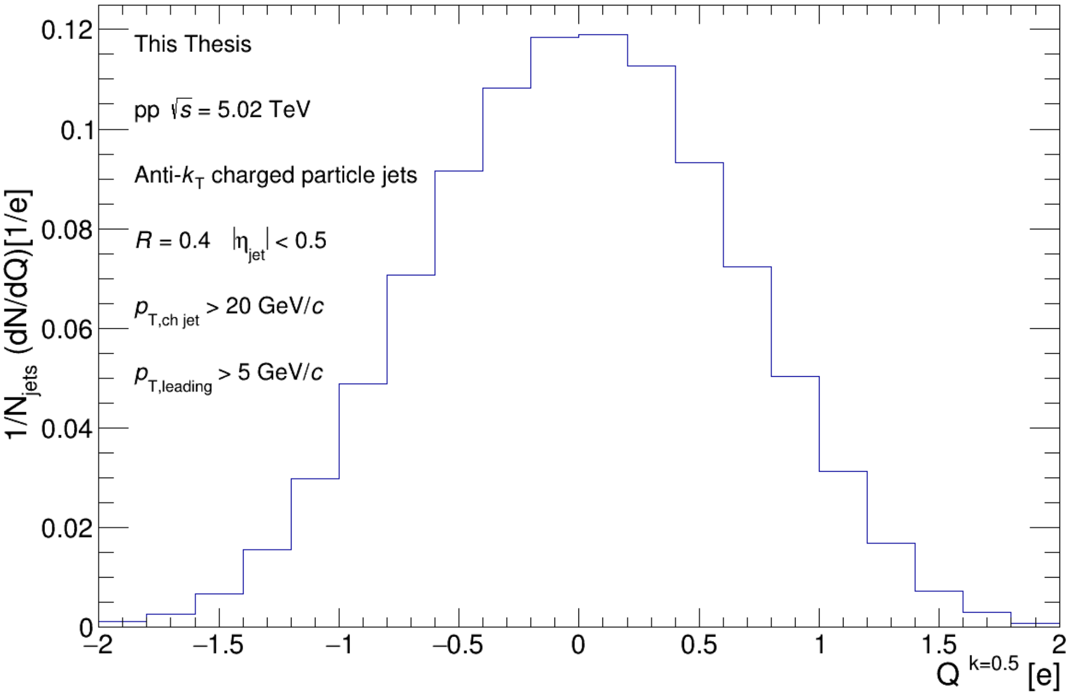

Figure 5.1: Normalised jet charge distribution from jets extracted from the LHC17q, 5.02 TeV pp data measured at ALICE. This graph contains jets of measured momenta $p_{T,\text{chJet}} >$ 20 GeV/c.

The partons that may be involved in a jet's hard scatter are valence quarks, sea quarks, anti-quarks and gluons. Therefore, these can be separated into three groups: negative charge, positive charge, and neutral. The negative charge group is composed of down, strange, bottom, anti-up, anti-charm and anti-top quarks. The positive charge group receives contributions from up, charm and top, as well as anti-down, anti-strange, and anti-bottom quarks. The neutral group contribution comes only from gluons. This distinction provides an exciting opportunity because, while there is an overlap between these groups, the gluon-type jets influence the jet charge in a way that differs from any quark or antiquark-type jets. Thus, there is the potential to separate the gluon-like jets from the quark-like jets by investigating the jet charge. This separation offers an interesting avenue of investigation as it allows the analysis of the effects of the QGP on quark- and gluon-like jets. A suppression of gluon-like jets is expected in Pb-Pb collisions as gluons are suggested to interact more strongly (than quarks) with the QGP due to being doubly colour charged, as predicted through lattice QCD simulations [124]. The result would be a reduction in the integral of the final distribution of gluon-like jets and, thus, a reduction in the measured gluon-like jet yields. This quenching would be represented in data by broadening the jet charge distribution in Pb-Pb collisions since the gluon jet charge distribution is narrower than its quark counterparts. This narrowed distribution results from the gluon-like distribution being centred around the gluon's electrical charge, 0. The quark-like distribution is composed of jet charge distributions from quarks of both positive and negative jet charges. Thus, the jet charge distribution for quark-like jets is spread over a broader range than for gluon-like jets. These distribution shifts have been shown by CMS previously [56] [57].

5.2 Jet Charge Template Generation

The jet charge for a single jet is not a useful quantity. This is due to the wide range of potential jet charges measured for a single jet dominating over the effect of the initial parton. Instead, the jet charge becomes valuable when a distribution is created using the jet charge calculated from many jets. This process can be completed for the data to construct a distribution for the jet charge seen in actual collisions. However, doing so with real data alone does not enable distinguishing between quark-like and gluon-like jets, as there is no way to determine the initial parton in an event. This is because the parton cannot be measured directly by the detector. Additionally, since the QGP does not extend into the inner tracker, the partons would not be free to interact with the detector, and only final-state particles can be detected. This means it is not simply a matter of finding the progenitor parton for a jet in the collision data.

Thus, Monte Carlo (MC) events have been used to create distributions for the jet charge for each type of initial parton because the MC events generated contain information about the entire collision system, including the initial partons. These distributions can then be used as templates and fitted to the data. This would allow jets to be identified on a statistical basis but not a jet-by-jet basis.

This raises the challenge of determining the progenitor parton for a given jet in the MC events. This challenge must be resolved to create these jet charge templates linked to given progenitor partons. Two approaches to acquiring and determining the initial parton have been investigated and will be discussed here. These two methods are referred to as the structure-based method and the momentum-based method.

5.2.1 The Structure-based method

While the MC data contain information about the initial-state particles, it does not have information about jets, as this information depends on the choice of parameters for the jet-finding algorithm. Thus, the first step is to perform jet finding on the final-state particles of the reconstructed MC data. This process must be completed both at the ‘detector’ and ‘particle’ level, as this is required for the unfolding process discussed in section 4.3. Once this is done, jet matching is performed to find the geometrically closest jet between the particle-level and ‘detector level’ jets in the MC data. It will then take these two jets and match them together, linking them in the analysis framework and allowing them to be directly compared.

Each particle within a MC data sample contains information linking it to the particle that created it, known as the "mother" particle. This process forms the core of the structure-based method. The mother particle is retrieved for each of the particles in the ‘particle level’ jet. This mother particle can then similarly be queried until the final mother particle has been reached for each jet particle. Once completed for all the particles in the jet, the output is an array containing the possible progenitor partons of the jet. In the ideal case, this collection of particles contains only one parton, and then the flavour of the parton can be linked to the jet. If there is more than one potential type of parton associated with the jet, the most frequent parton is connected to the jet and the fraction of the particles which agree with this most frequent parton is also recorded with the jet. This can occur as jet finding is not deterministic, and background particles may be wrongly associated with the jet. The measurement of the fraction of particles that agree with the progenitor parton is also an indicator of the certainty of matching, which can be used when analysing the data to select jets with only confident matching. This discrepancy in the possible progenitor partons can occur due to the jet-finding algorithm. This discrepancy happens when the algorithm is clustering a particle that does not originate from the initial hard scatter into the jet, thus leading to disagreement about the progenitor parton. Once this has been done for all jet candidates in the MC data sample, the jet charge distributions can be associated with different progenitor partons. This is shown in figure 5.2.

Table 5.1: The table shows the means extracted for the four jet charge distributions associated with specific partons (from figure 5.2) using the structure-based method. These means are calculated for a 60% agreement in parton flavour.

Parton	Mean Jet Charge [e]	σ
Up	0.048 ± 0.002	0.56
Down	-0.032 ± 0.002	0.56
Gluon	0.006 ± 0.001	0.56
Other	-0.032 ± 0.003	0.56

Figure 5.2 shows the relative distributions for the gluon, up, down and ’other’ pro-

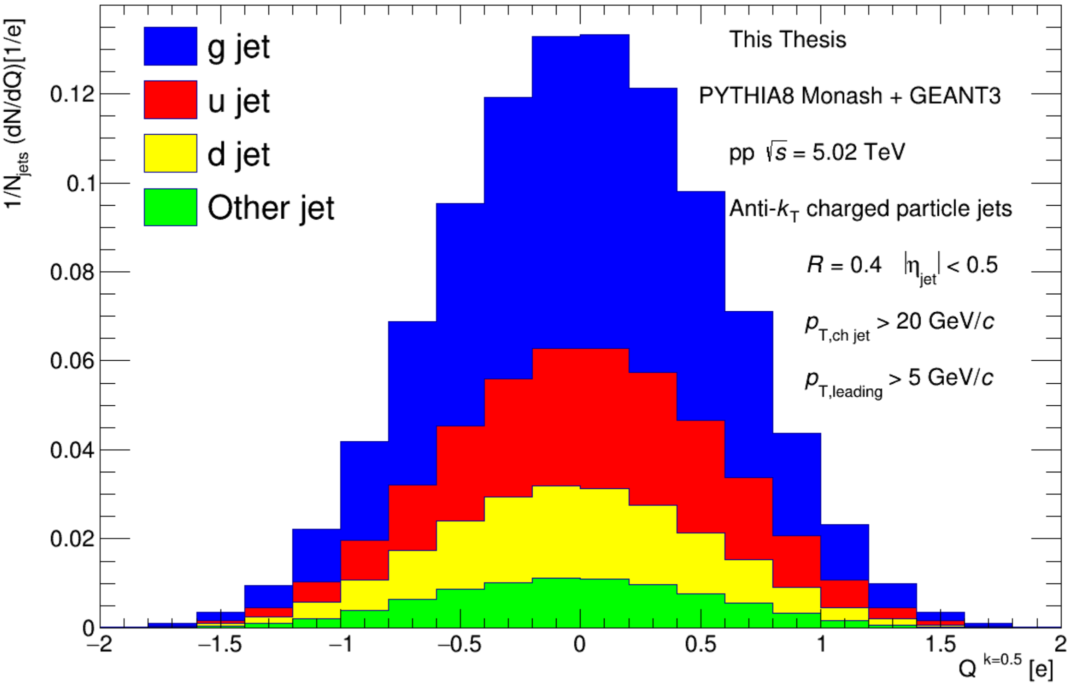

Figure 5.2: A stacked histogram showing the normalised jet charge distributions from jets extracted from the LHC17q pp MC data measured at ALICE. This graph contains jets of measured momenta $p_{T,\mathrm{chjet}} > 20$ GeV/c and is separated by colour into progenitor parton. The blue section of the histogram is the gluon contribution. The red section is the up-quark contribution. Similarly, the yellow portion is the down quark distribution, and the green is the grouped anti-quark, strange quark and heavy quark contribution. These distributions are produced by the structure-based method.

genitor parton of jets. The four distributions are shifted with respect to each other as expected according to the progenitor parton. Namely, the means of each distribution are: $< g >= 0.006$ e for gluons,$< u >= 0.048$ e for up quarks,$< d >= -0.032$ e for down quarks and $< o >= -0.032$ e for others. These means and the corresponding error on the mean and standard deviation are reported in table 5.1. However, while the distributions for each jet charge type are shifted in the direction expected for its given progenitor parton, the distributions are still highly central, and the overall range is significantly larger than the magnitude of any of the shifts shift. In theory, the size of this separation is not an issue; so long as there is a consistent shift, the separation between gluon and quark jets exists. However, the small magnitudes of these differences can cause problems in differentiating the templates. This can pose issues as to validate the MC method; it must be fitted to the data. This difficulty fitting is because if these differences are smaller than the differences between the MC data and the real data after unfolding or other systematic errors, these differences will no longer be sufficient for separating progenitor partons. Therefore, maximising these differences is one of the critical conditions of using this method.

There are three methods to attempt to maximise the seperatation between different progenitor parton jet charge distributions. The first and most straightforward method is to adjust the requirements placed on the certainty of the progenitor parton. For example, requiring 90% of partons to agree rather than 60% will be more stringent in determining the progenitor parton. It should reduce the number of incorrect jet-parton identifications in the sample. However, this method has the downside of reducing the statistics as the number of unmatched jets increases rapidly with the tightness of the cut, as seen in figure 5.3. This figure shows the jet yields for $R = 0.4$ jets for a given fraction of particles agreeing with the progenitor. It can be seen that a stricter level of agreement causes the jet statistics to reduce to at most 40% of the sample. In addition, the effect of this cut has a limited impact on the shape of this distribution, as seen by comparing figure 5.4 with a stricter 90% agreement cut and figure 5.5 with a 70% agreement cut. The comparison between these figures shows that the difference between quark templates and gluon templates is virtually unaffected by the cut on the fraction of particles agreeing on the progenitor parton.

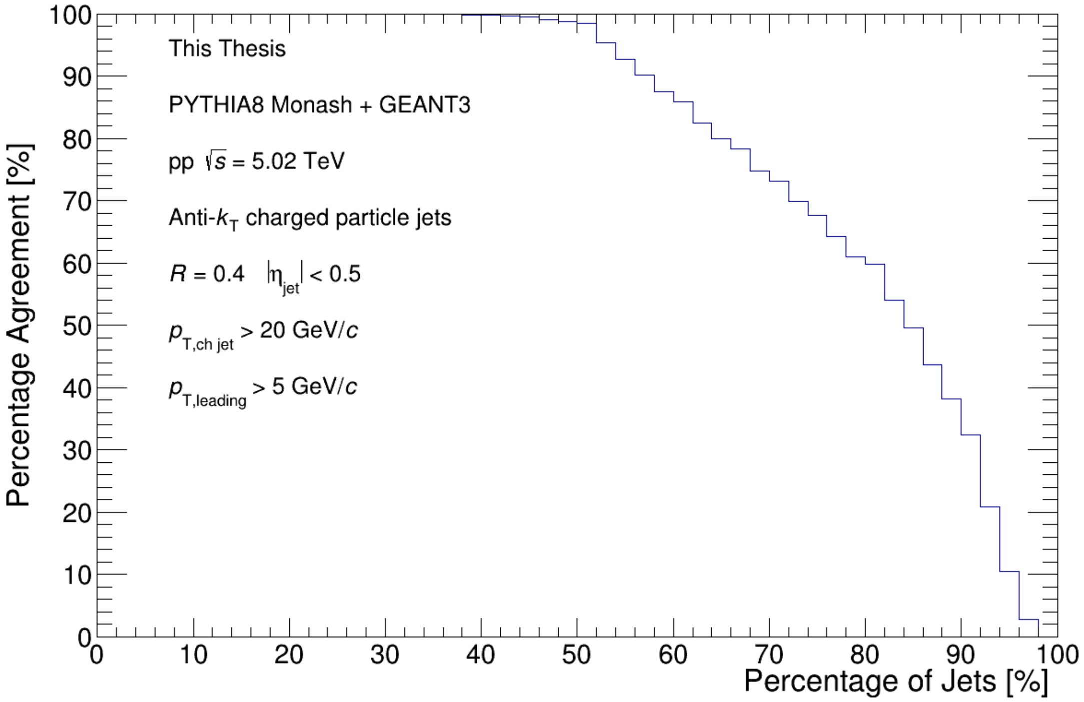

Figure 5.3: A histogram showing the percentage of jets with a given percentage of particles agreeing on the flavour of the progenitor parton. This is important to note, as decreasing the fraction of this cut will substantially reduce the number of unmatched jets. As can be seen from the graph, applying a tighter cut by requiring a higher agreement percentage(which would substantially reduce the number of unmatched jets) has the consequence of also reducing the usable jet statistics significantly.

There is little benefit to increasing the agreement level cut too high because of the small number of final-state particles making up the jet. A single soft particle being clustered into the jet can drastically reduce the certainty of a given progenitor parton for a jet. The significant variance from a single soft particle combined with the minimal effect and the reduction in the number of usable jet statistics means that the fraction of particles required to agree to classify a jet is chosen $f > 0.5$ for all subsequent analysis. This maximises the

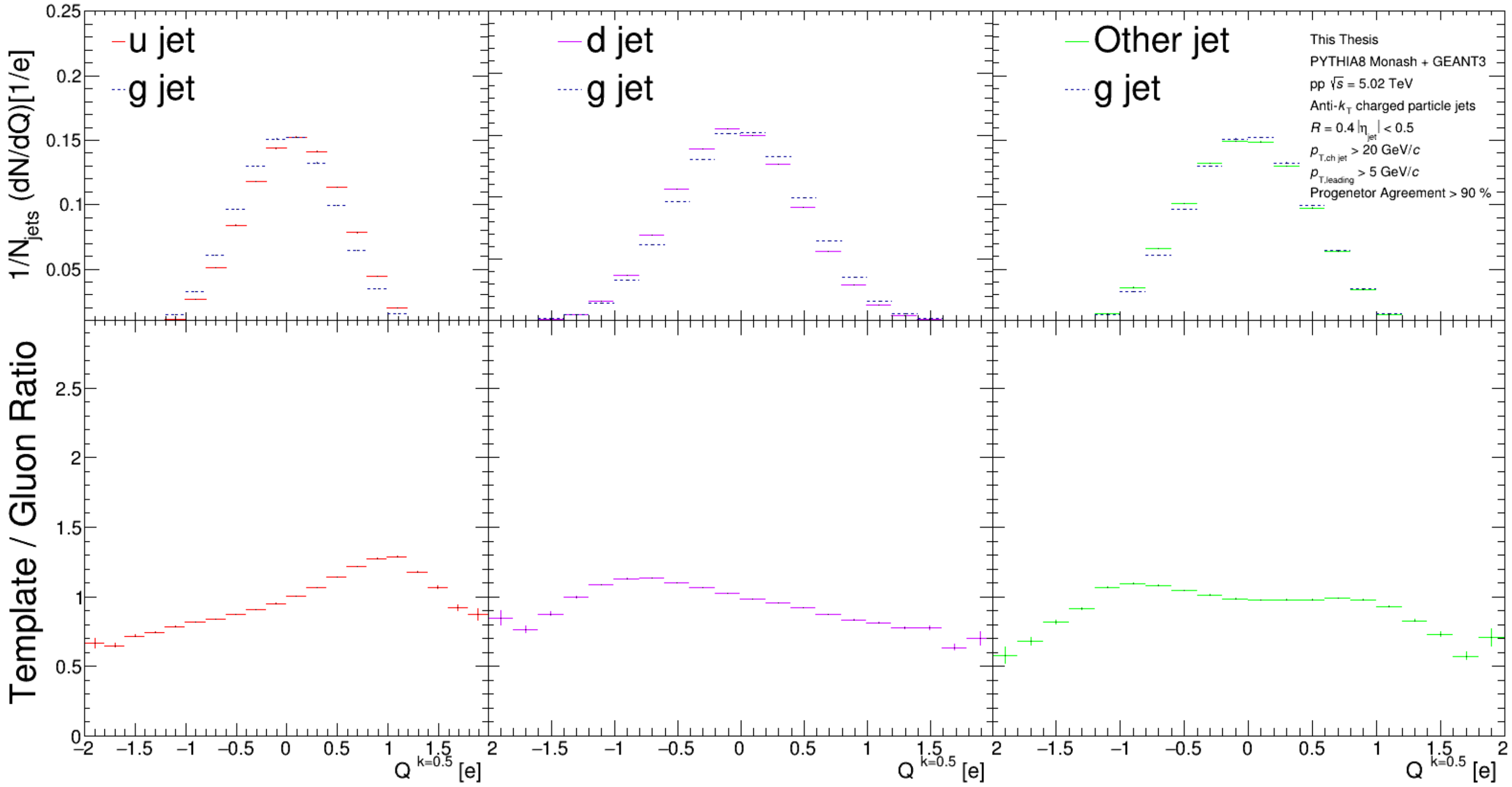

Figure 5.4: The top series of graphs show the normalised jet charge for both gluon distributions and up, down and other quark/antiquark distributions from left to right. The bottom series of graphs show the ratio between the given quark or antiquark or antiquark or antiquark and gluon distributions. This ratio allows the comparison between the distributions in order to determine the maximum distinction between the templates. This graph is constructed with $p_{T,\mathrm{chJet}} > 20$ GeV/c and $R = 0.4$. This graph differs from figure 5.5 by including a harsher 90% requirement on the jet's particles agreement with the initial parton.

number of usable jets in the sample.

The next avenue was to investigate the effect of jet radius R on the jet charge templates.

By comparing figures 5.6 for $R = 0.1$ and 5.5 for $R = 0.4$, the effect of the jet radius on the shape and differentiation of the jet charge templates is minimal, with the most significant difference being in the shape of the other quark/antiquark jet charge distribution template. This minimal effect means that the jet radius should be selected to prioritise a larger number of jets. In this case, $R = 0.4$ is chosen to maximise the number of high-momentum jets, the reason for which will become apparent when considering the effects of transverse jet momentum.

The remaining option for increasing the differences between these jet charge distribution templates was to increase the minimum jet transverse momentum cut $p_{T,\mathrm{jet}}$.

As seen in figure 5.7 where $p_{T,\mathrm{chJet}} > 80$, the effect on the distributions from the $p_{T,\mathrm{chJet}}$ cut is significantly larger than what is seen from adjusting jet radius. However, a substantial downside to increasing minimum $p_{T,\mathrm{chJet}}$ value is that it dramatically reduces the statistics available in the resulting data set. This reduction is because of the rapid decrease in the number of jets of high momentum, as seen in figure 5.8.

Figure 5.8 means that while selecting a higher value of $p_{T,\mathrm{chJet}}$ selection increases separation between jet charge distributions of different progenitor partons, it is not practical as the number of jets extracted with this higher $p_{T,\mathrm{chJet}}$ cut would not be enough to form a statistically significant sample.

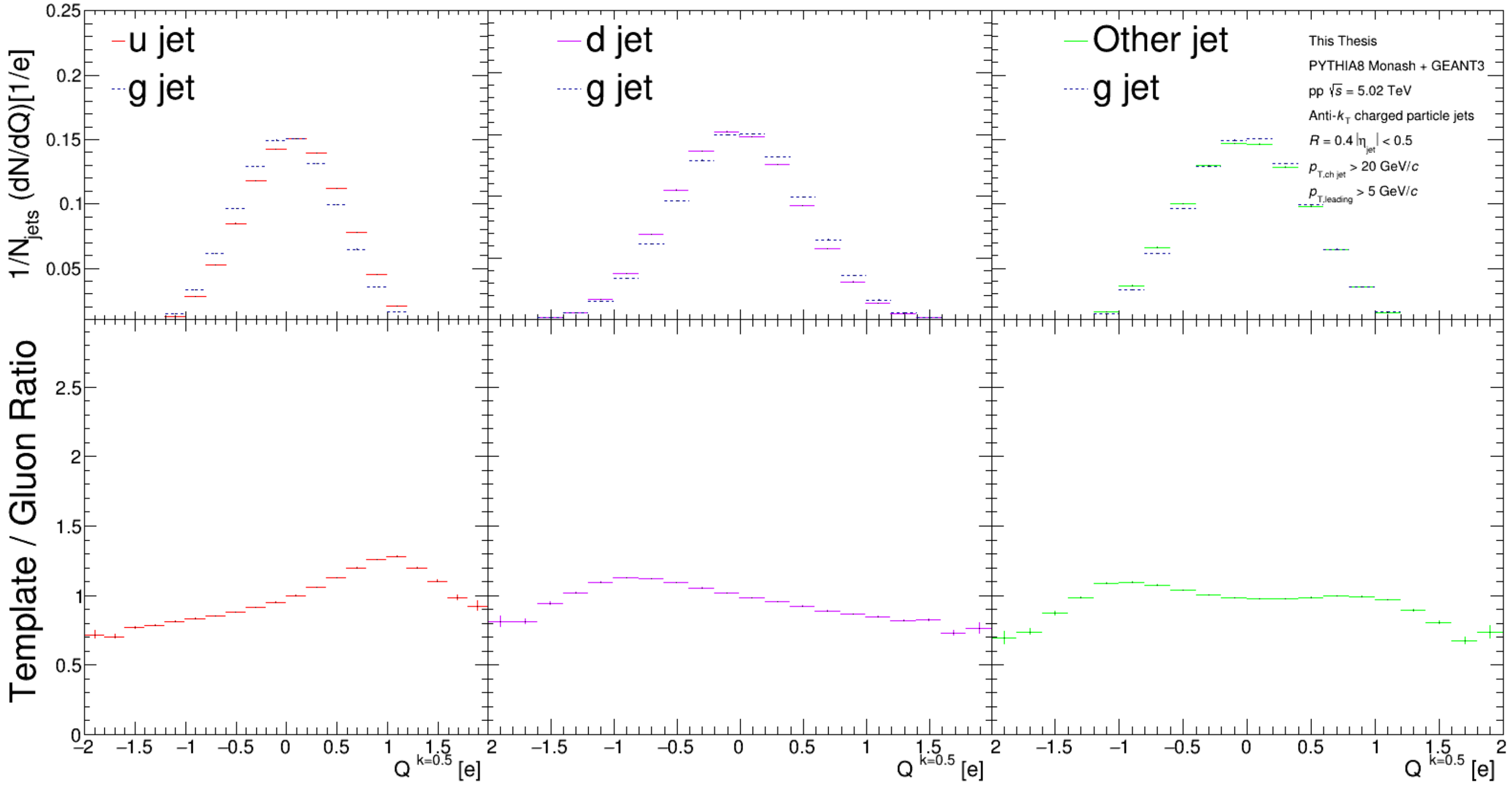

Figure 5.5: The top series of graphs show the normalised jet charge for both gluon distributions and up, down and other quark/antiquark distributions from left to right. The bottom series of graphs show the ratio between the given quark or antiquark or antiquark or antiquark and gluon distributions. This ratio allows the comparison between the distributions in order to determine the maximum distinction between the templates. This graph is constructed with $p_{T,\mathrm{chJet}} > 20$ GeV/c, $R = 0.4$ and a 70% parton agreement cut.

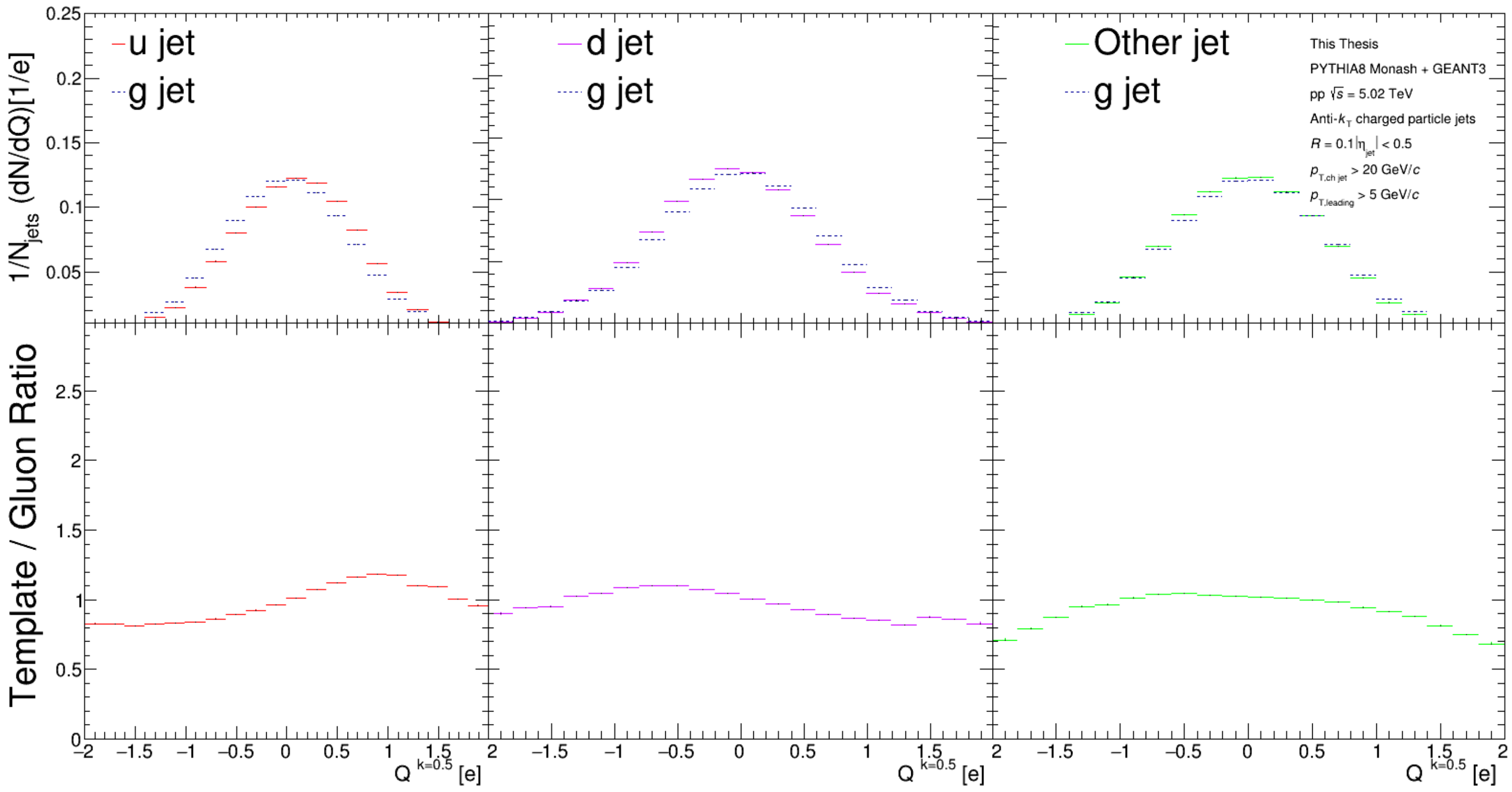

Figure 5.6: The top series of graphs show the normalised jet charge for both gluon distributions and up, down and other quark/antiquark distributions from left to right. The bottom series of graphs show the ratio between the given quark or antiquark or antiquark or antiquark and gluon distributions. This ratio allows the comparison between the distributions in order to determine the maximum distinction between the templates. This graph is constructed with $p_{T,\text{chJet}} > 20$ GeV/c, $R = 0.1$ and a 60% parton agreement cut.

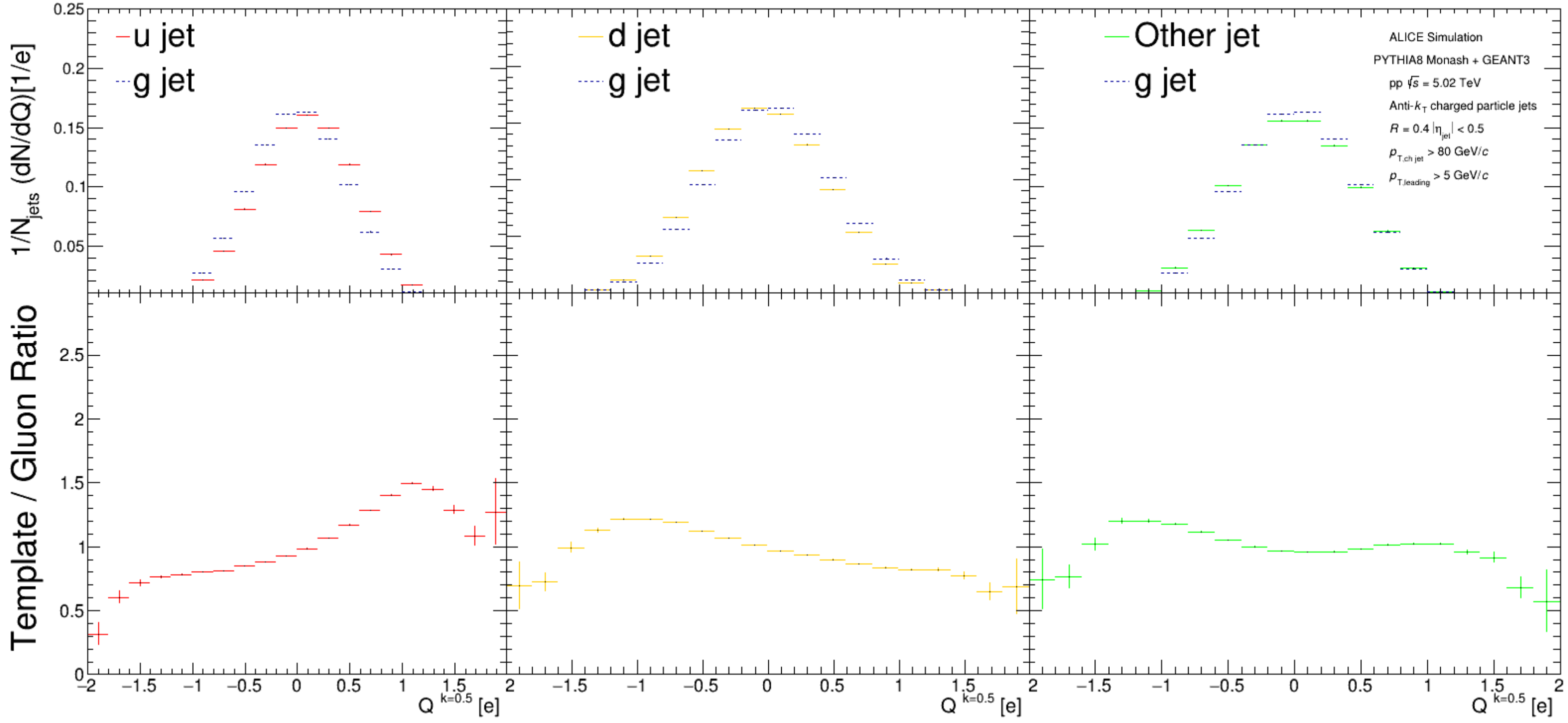

Figure 5.7: The top series of graphs show the normalised jet charge for both gluon distributions and up, down and other quark/antiquark distributions from left to right. The bottom series of graphs show the ratio between the given quark or antiquark or antiquark or antiquark and gluon distributions. This ratio allows the comparison between the distributions in order to determine the maximum distinction between the templates. This graph is constructed with $p_{T,\text{chJet}} > 80$ GeV/c and $R = 0.4$ and a 60% parton agreement cut.

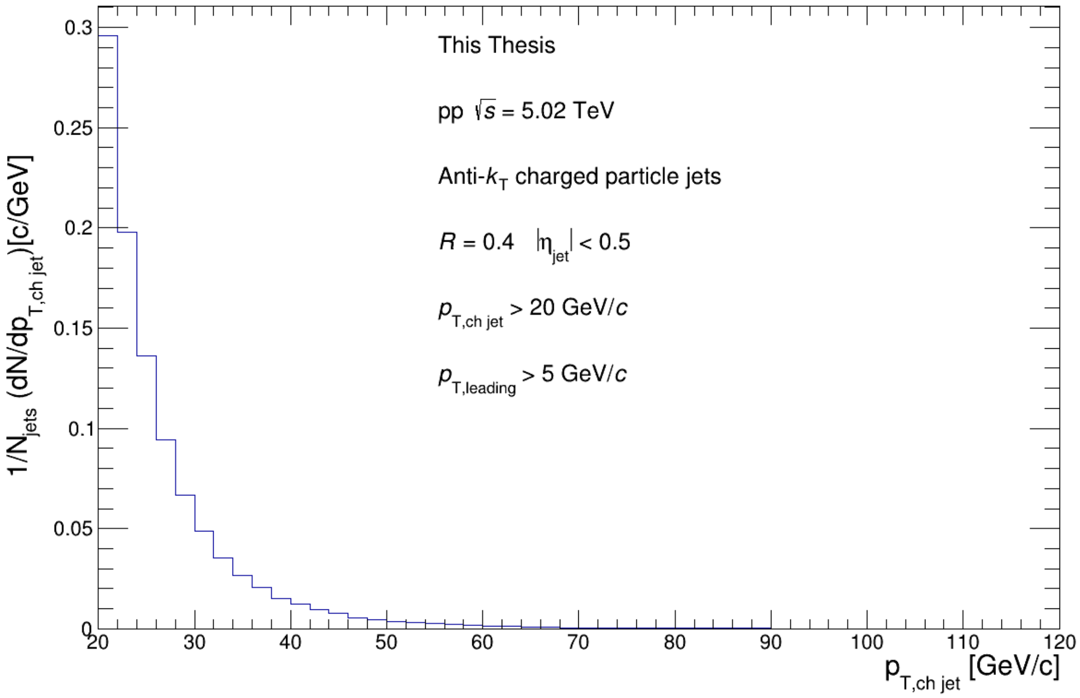

Figure 5.8: Normalised momentum distribution of jets with $p_{T,\text{chJet}} > 20$ GeV/c and $R = 0.4$. It is important to note that the $p_{T,\text{chjet}}$ distribution rapidly decays. Thus, using higher $p_{T,\text{chjet}}$ cuts severely reduces the number of usable jet statistics.

5.2.2 The Momentum-based method

The second approach also requires MC data to access parton information. However, this technique uses a positional matching of the partons to a jet. The first step of the method is to consider all particles in the event and discount all particles that are not partons. This removal is because the partons are the only particles that can cause the initial hard scatter. The next step is to disregard all partons outside of the jet radius; this allows the number of partons to be narrowed down into a selection that could be closely related to the jet. Finally, the remaining partons are ordered by their transverse momentum. If any remaining partons are b-quarks or c-quarks, these are considered to be the partons that initiated the jet. This selection is because these partons are known to be created in the initial collision due to their large mass. If there are no b-quarks or c-quarks in the sample, then the parton with the largest transverse momentum is selected as the jet progenitor parton. This choice is because the highest transverse momentum parton is the most likely to be the progenitor parton from the initial hard scatter.

Table 5.2: The table shows the means extracted for the four jet charge distributions associated with specific partons (from figure 5.9) using the structure-based method as well as the distribution widths σ.

Parton	Mean Jet Charge [e]	σ
Up	0.364 ± 0.003	0.49
Down	-0.230 ± 0.002	0.50
Gluon	0.000 ± 0.001	0.56
Other	-0.032 ± 0.002	0.57

This selection approach has the advantage over the previous technique that there is no ambiguity in the parton selected. Thus, there is no need to implement a threshold for the percentage of particles in agreement with the progenitor parton. Additionally, as seen in figure 5.9 and figure 5.10, there is a significantly larger separation between the different jet charge distribution templates with this technique with the means of each distribution

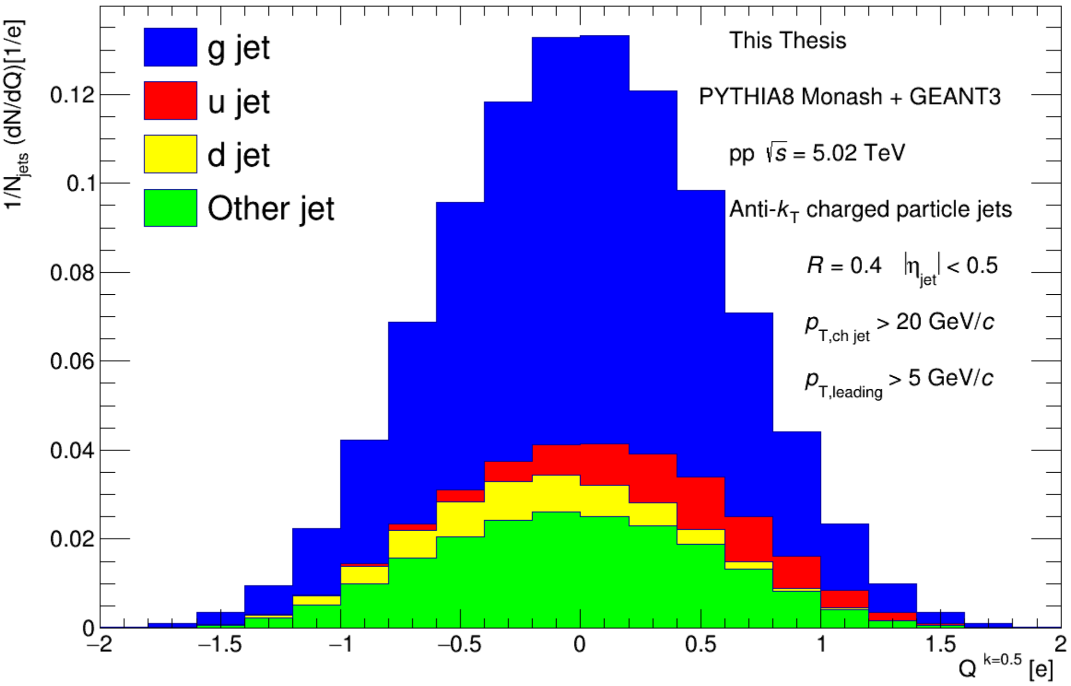

Figure 5.9: A stacked histogram showing the normalised jet charge distributions from jets extracted from the LHC18b8 pp MC data measured at ALICE. This graph contains jets of measured momenta $p_{T,\mathrm{chjet}} > 20$ GeV/c and is separated by colour into progenitor parton. The blue section of the histogram is the gluon contribution. The red section is the up-quark contribution. Similarly, the yellow portion is the down quark distribution, and the green is the anti-quark, strange quark and heavy quark contribution. These distributions are produced by the momentum-based method.

extracted, $< g >= 0.000$ as gluons, $< u >= 0.364$ as up quarks,$< d >= -0.230$ as down quarks and $< o >= -0.031$ as other quarks and antiquarks. The full details for yields of gluons quarks and antiquarks can be found in table 5.2. This separation, combined with the larger gluon fraction (see visually from from comparing figures 5.2 and 5.9) extracted with this technique and the fact that the width of the total distribution is unchanged, suggest that this technique is now including, as gluon jets, jets that the structure-based method previously categorised as quark jets (which had a near zero jet charge). This has the effect of increasing the separation between the templates.

Interestingly, as seen in comparing figure 5.10 and 5.11, unlike with the previous structure based method, these templates are not as strongly affected by the choice of minimum $p_{T,\mathrm{chJet}}$ cut. Thus, this technique gives a more substantial separation without sacrificing statistics by considering higher $p_{T,\mathrm{chJet}}$ jets. Given the lack of sensitivity to the $p_{T,\mathrm{chJet}}$ cut it appears that low $p_{T,\mathrm{chJet}}$ jets are as reliable as high $p_{T,\mathrm{chJet}}$ jets. Thus, a cut of $p_{T,\mathrm{chjet}} > 20$ GeV/c was used for the rest of the analysis.

Comparing the effects of changing the jet radius between $R = 0.1$ in figure 5.12 and $R = 0.4$ in figure 5.10, it is clear that the effects of the jet radius are limited but are in slight favour of $R = 0.4$. Thus $R = 0.4$ is used as the jet radii from this point in the analysis onward.

5.2.3 Technique Summary

For the template fitting procedure to work, the jet charge templates extracted for each jet type must be fitted to the jet charge distribution extracted from the data. Thus, the templates of different flavours must be sufficiently differentiated for this fit to be feasible. Without strong separation, the difference between templates will be negligible compared

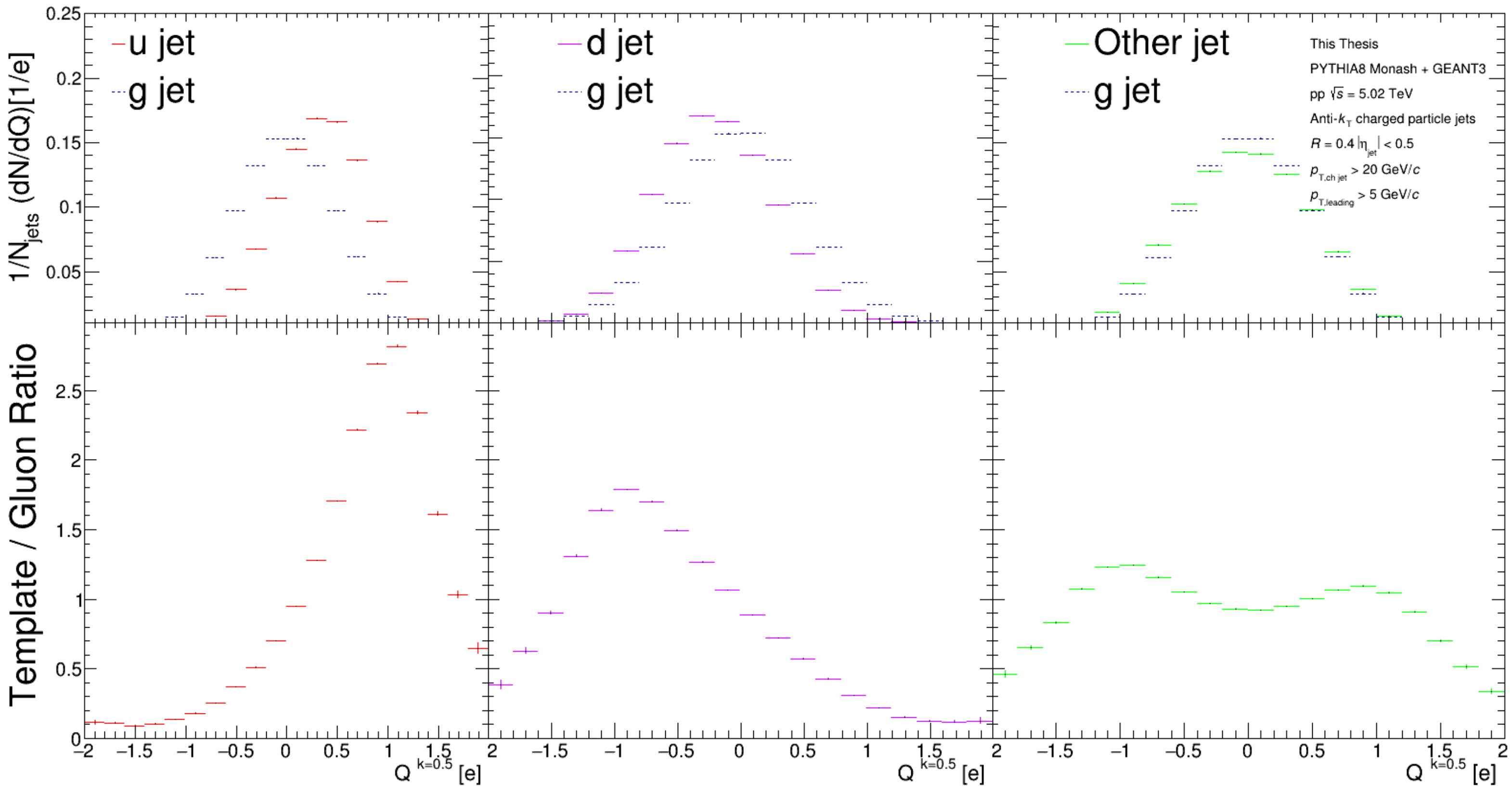

Figure 5.10: The top series of graphs show the normalised jet charge for both gluon distributions and up, down and other quark/antiquark distributions from left to right. The bottom series of graphs show the ratio between the given quark or antiquark or antiquark and gluon distributions. This ratio allows the comparison between the distributions in order to determine the maximum distinction between the templates. This graph is constructed with $p_{T,\mathrm{chJet}} > 20$ GeV/c and $R = 0.4$. These distributions have been generated using the momentum-based method.

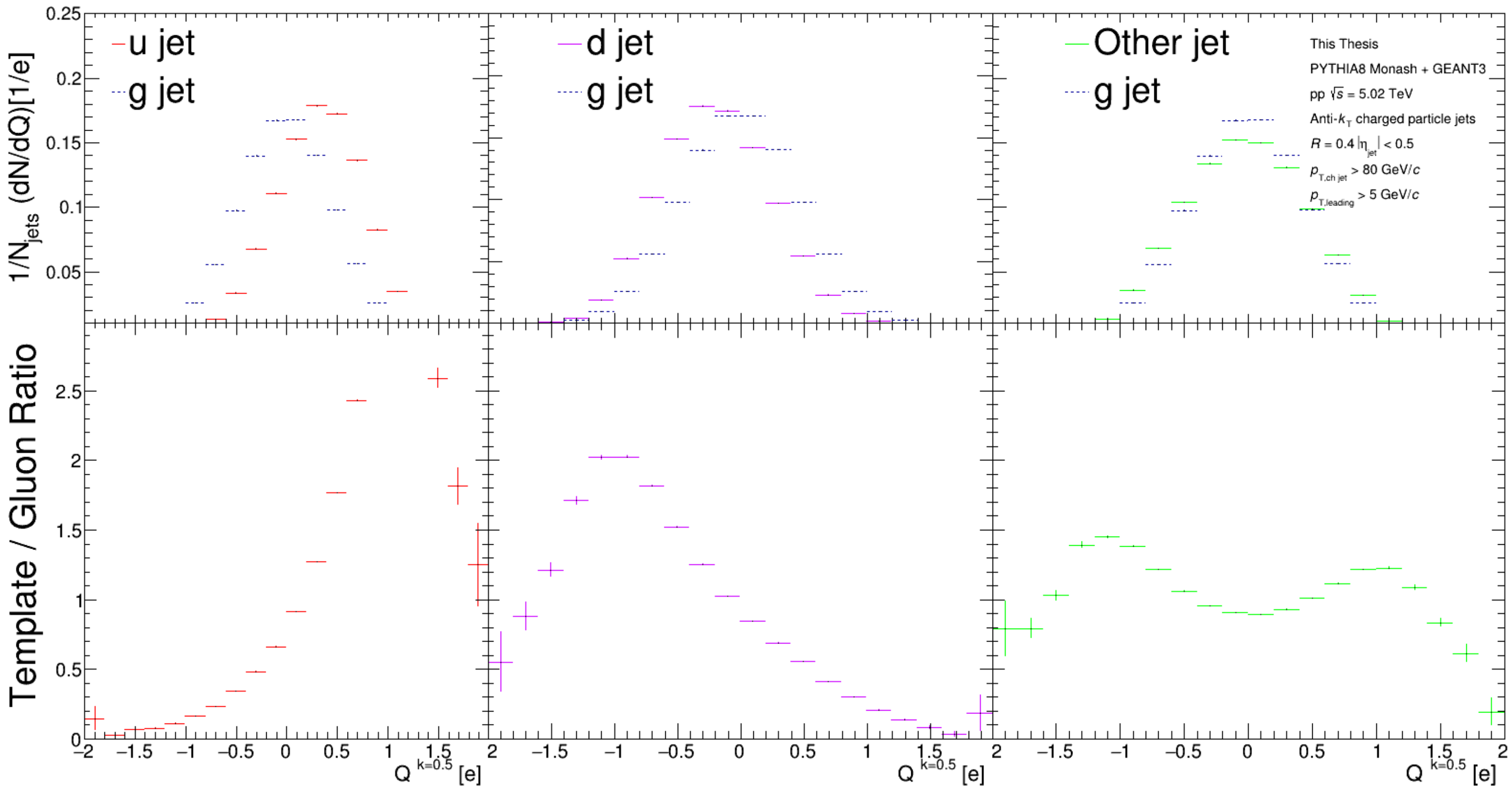

Figure 5.11: The top series of graphs show the normalised jet charge for both gluon distributions and up, down and other quark/antiquark distributions from left to right. The bottom series of graphs show the ratio between the given quark or antiquark or antiquark and gluon distributions. This ratio allows the comparison between the distributions in order to determine the maximum distinction between the templates. This graph is constructed with $p_{T,\mathrm{chJet}} > 80$ GeV/c and $R = 0.4$. These distributions have been generated using the momentum-based method.

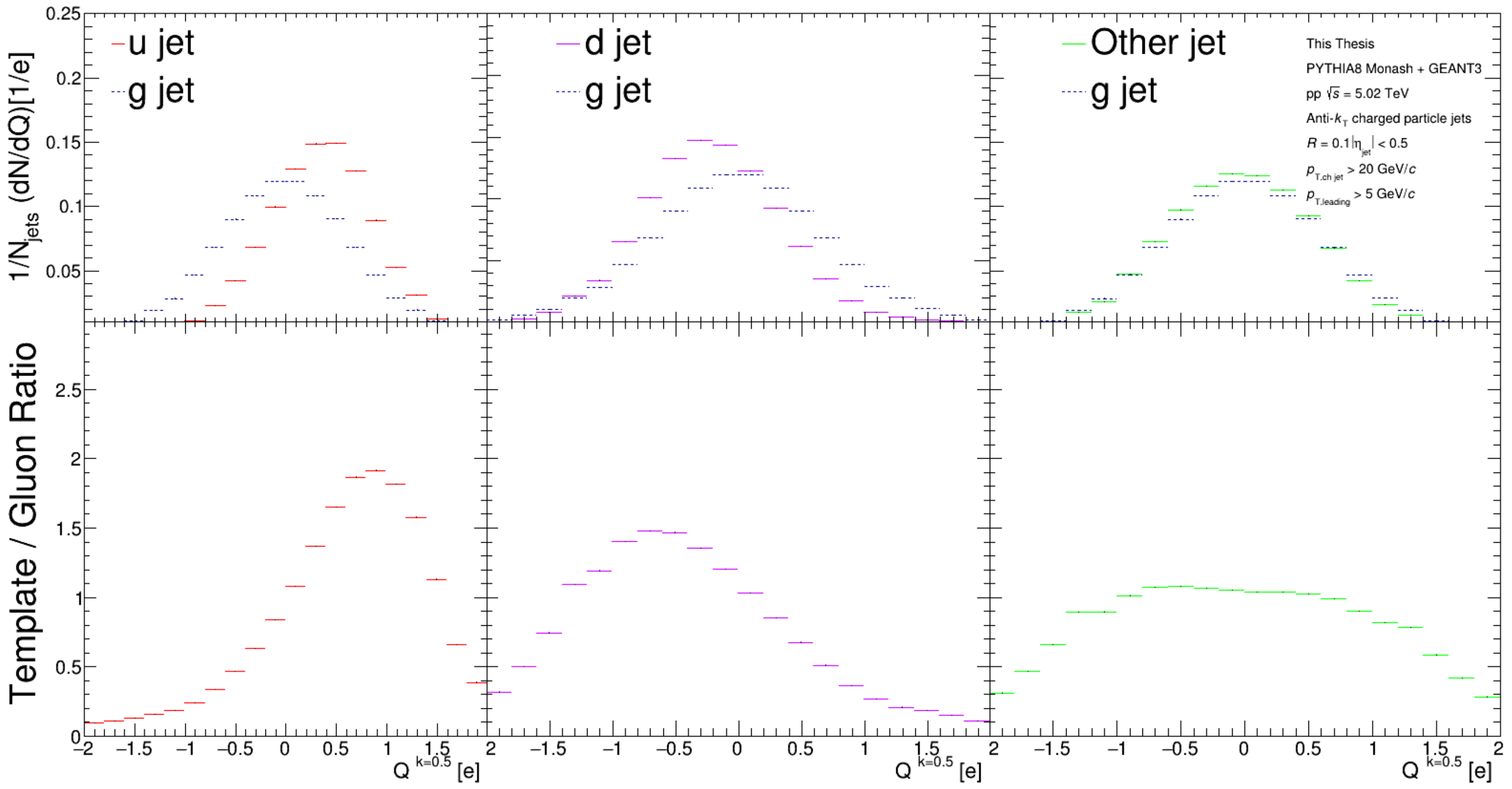

Figure 5.12: The top series of graphs show the normalised jet charge for both gluon distributions and up, down and other quark/antiquark distributions from left to right. The bottom series of graphs show the ratio between the given quark or antiquark or antiquark and gluon distributions. This ratio allows the comparison between the distributions in order to determine the maximum distinction between the templates. This graph is constructed with $p_{T,\mathrm{chJet}} > 20$ GeV/c and $R = 0.1$. These distributions have been generated using the momentum-based method.

to the fluctuations between the MC dara and the real data. If this is the case, the fitting algorithm would be unable to extract any useful results when fitting the templates to the data, as these fluctuations would dominate over the small changes in the templates.

The momentum-based method shows a higher level of template separation as seen by comparing the figures 5.10 and 5.5. This, combined with the fact that it does not require cut on the large $p_{T,\mathrm{chJet}}$ values means the momentum-based method is used moving forward in this analysis.

5.2.4 Jet Charge in Pb-Pb

The technique for extracting the jet charge templates described above only works for pp collisions. Pb-Pb collisions require some modifications in order to generate jet charge templates. The difficulty arises from the extensive background comprised of soft particles in Pb-Pb collisions. Pb-Pb collisions must be considered to explore the effects of the QGP on the jet charge. Thus, some changes to the technique described above must be made to analyse these collisions.

The first difference encountered is that full MC events for Pb-Pb data are prohibitively computationally expensive to generate. Instead, pp MC data events are embedded into real Pb-Pb events so that background particle generation is not required. Additionally, since the background is from real data, it is guaranteed to describe the environment in which real jets are found.

The next step was to apply the constituent subtraction technique discussed in section 2.4.1 to the sample. This technique attempts to remove the majority of the soft background from the event. This is an important step as background removal is required while analysing the collision data and thus must be performed on the MC data to ensure consistency. Template generation still requires access to parton information; thus, the embedded MC data jets must be extracted from the combined embedded data. The following steps are required to extract this information:

1. Jet finding is performed using the k_T algorithm on the Pb-Pb events in order to calculate the average momentum density ρ for use in the constituent subtraction technique.
2. Jet finding is performed using the anti-k_T algorithm on the full Pb-Pb data sample with embedded pp MC events which have been preselected for high Q^2 scatter events complete with Pb-Pb background.
3. Jet finding is performed using the anti-k_T algorithm on the full embedded events after background subtraction using constituent subtraction using the background measured in step 1.
4. Jet matching is used to match these jets from step 2 and step 3 geometrically so jets can be compared to their background-subtracted counterparts.
5. Jet finding using the anti-k_T algorithm can then be performed on the 'detector level' MC data sample that was embedded (but that is not currently embedded).
6. These jets from step 5 can then be geometrically matched to the previous background subtracted jets from step 3.
7. Jet finding using the anti-k_T algorithm is performed on the particle-level MC data sample that was embedded (the same as in step 5) , and these jets are matched to the previous 'detector level' jets from step 5.

The final outcome is that the jets found at the full event (pp MC data embedded into Pb-Pb real data at the detector level) and the pp MC data sample 'particle level' are linked. Thus, the jet charge can be calculated at the full event with background as it would be with the data, and the initial parton can be determined using the 'particle level' MC information. Thus, the effects of the background on determining the initial parton are mitigated while the effects of the background on the measured jet charge are maintained.

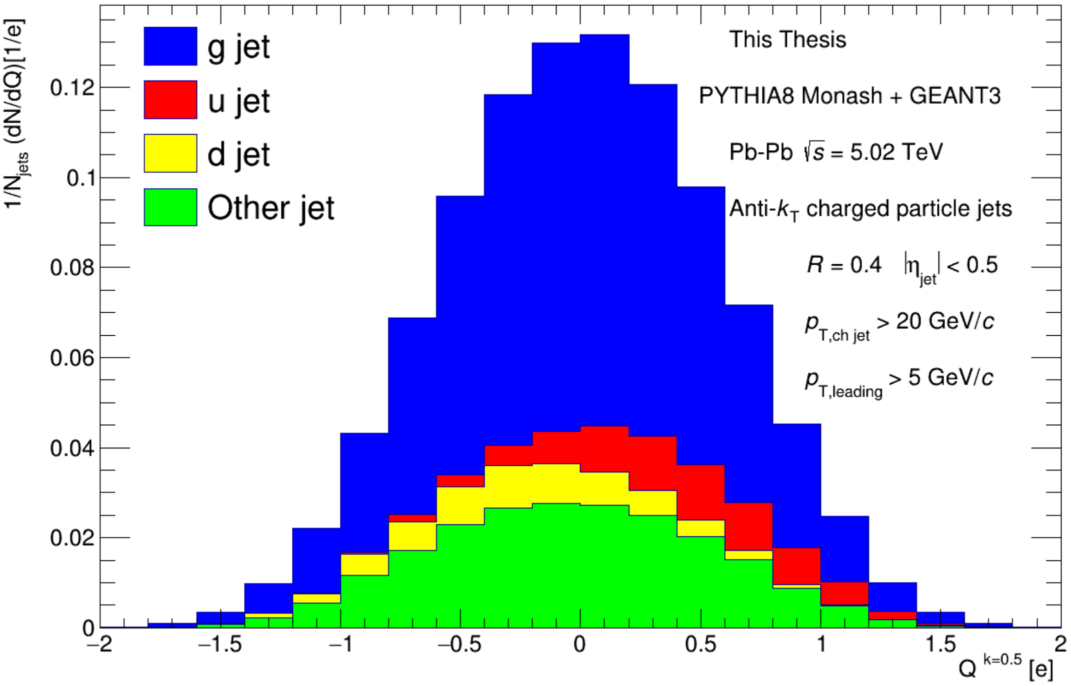

Figure 5.13: A stacked histogram showing the normalised jet charge distributions from jets extracted from the LHC19f4 Pb-Pb data for 0-10% centrality measured at ALICE. This graph contains jets of measured momenta $p_{T,\mathrm{chjet}} > 20$ GeV/c and is separated by colour into progenitor partons. The blue section of the histogram is the gluon contribution. The red section is the up-quark contribution. Similarly, the yellow portion is the down quark distribution, and the green is the anti-quark, strange quark and heavy quark contribution. These distributions are produced using Pb-Pb data at the 'particle level' using the momentum based method.

Figure 5.13 shows that it is clear that at the particle level, the jet charge templates for Pb-Pb collisions do not seem to differ significantly from the templates for pp collisions. However, this is not the case at the 'detector level', as seen in figure 5.14 (note the increased range in figure 5.14 compared to 5.13). This effect is interesting as it shows the effect the background particles have on the Pb-Pb templates since these effects are not seen at the particle level. These effects can be further investigated by considering the less central Pb-Pb collisions, shown in figure 5.15, which now approaches the 'particle level' distribution again. This regression to pp is expected, given that a less central collision would reduce the particle multiplicity and thus reduce the background's effect on the measurements. The unfolding process will mitigate the smearing to an extent. However, this will have a significant effect on the systematic errors from unfolding.

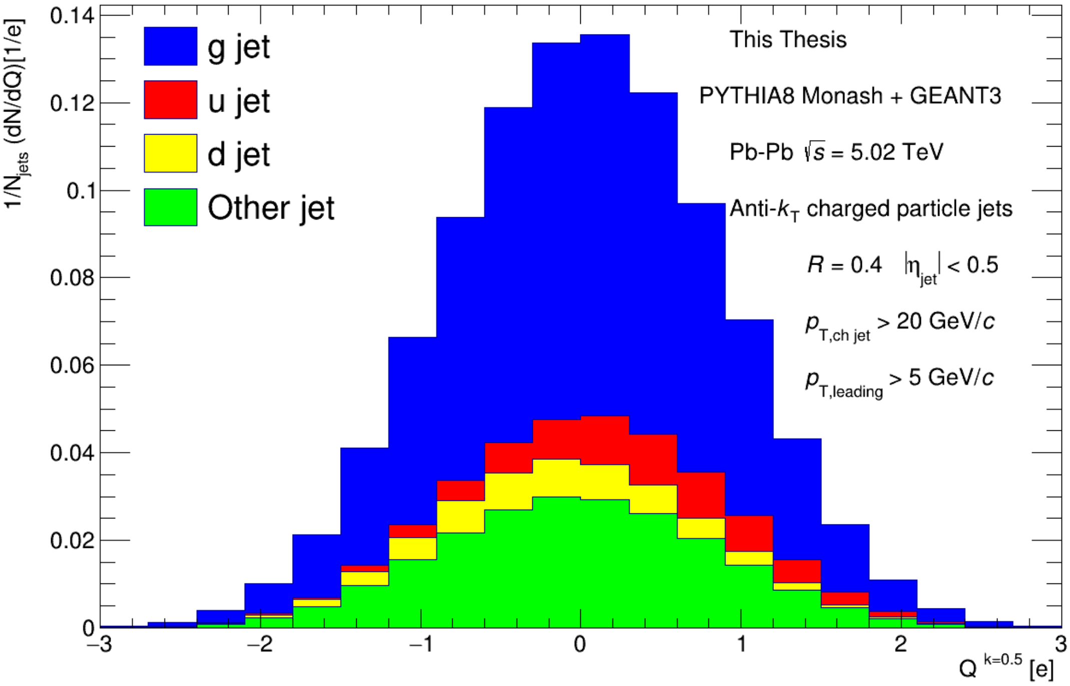

Figure 5.14: A stacked histogram showing the normalised jet charge distributions from jets extracted from the LHC19f4 Pb-Pb data for 0-10% centrality measured at ALICE. This graph contains jets of measured momenta $p_{T,\text{chjet}} > 20$ GeV/c and is separated by colour into progenitor partons. The blue section of the histogram is the gluon contribution. The red section is the up-quark contribution. Similarly, the yellow portion is the down quark distribution, and the green is the anti-quark, strange quark and heavy quark contribution. These distributions are produced using Pb-Pb data at the 'detector level' using the momentum based method.

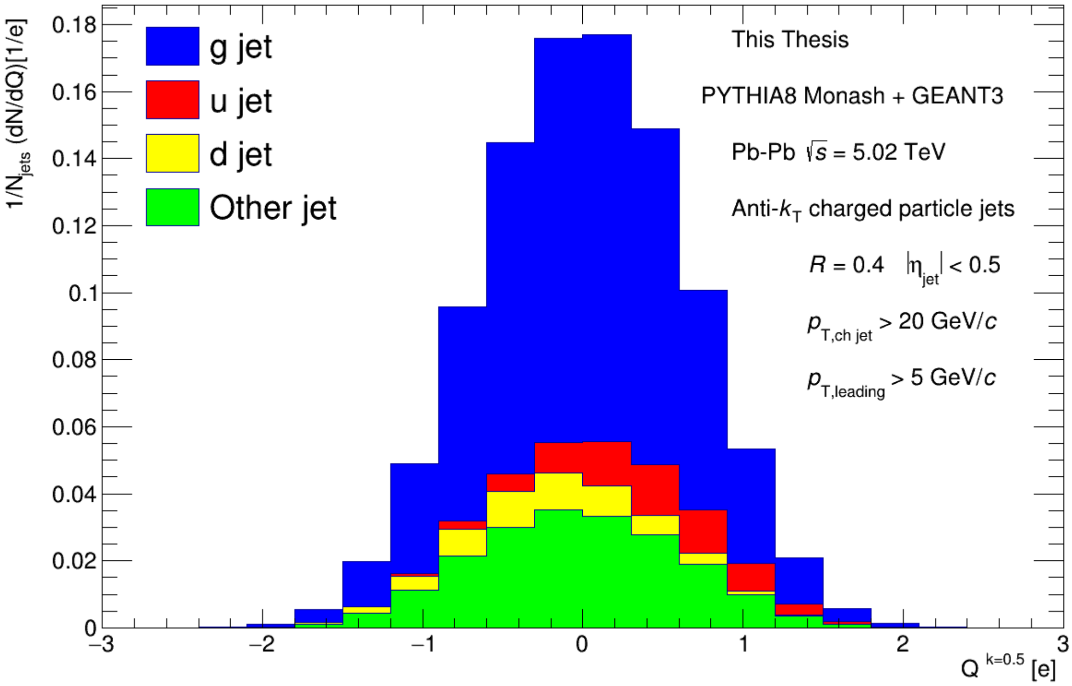

Figure 5.15: A stacked histogram showing the normalised jet charge distributions from jets extracted from the LHC19f4 Pb-Pb data for 80-90% centrality measured at ALICE. This graph contains jets of measured momenta $p_{T,\text{chjet}} > 20$ GeV/c and is separated by colour into progenitor partons. The blue section of the histogram is the gluon contribution. The red section is the up-quark contribution. Similarly, the yellow portion is the down quark distribution, and the green is the anti-quark, strange quark and heavy quark contribution. These distributions are produced using Pb-Pb data at the 'detector level' using the momentum based method.

5.2.5 Yield extraction

The main goal of the template fitting technique is to compare the effects of the QGP on jets in Pb-Pb and pp collisions and to see if these effects are jet charge dependent. The way of achieving this is by comparing the relative yield of gluon jets and quark jets measured in Pb-Pb and pp collision data respectively. This number can be found by integrating the gluon templates after properly normalising the templates such that the total integral of the jet charge distribution is unity. This integral can be performed before the templates are fitted to the data to examine the gluon yields produced directly from the MC.

Once this is done, the MC templates can then be fitted to the data, and the measured yields can be extracted. These yields have been extracted for both pp as well as Pb-Pb data. It is expected that the QGP would cause suppression in all jets but to a greater degree in gluon jets compared to quark jets [124]. The yields are calculated for increasing central Pb-Pb collisions to investigate this suppression. As the collisions become more central, the effects of the QGP should become more pronounced.

An additional step to consider when comparing the jet charge distribution templates is what the yields extracted from these templates are before using them to fit the experimental data and how these differ from what is expected. The details of these yields can be seen in table 5.3. There are some differences between the yields extracted that are immediately clear. Firstly, the gluon jet yields are significantly larger in the momentum-based method. This shift is matched by a corresponding larger up and down quark jet contribution from the structure-based method. Both methods share a gluon dominance as well as a larger number of up-quark jets than down-quark jets. The first set of yields that are concerning is seen in the ratio of quark to anti-quark yields in the structure-based method. This is because the expectation is that heavier quark and anti-quark pairs would have equal yields as they both only exist as sea quarks and are formed by pair production. The ratio between heavier quark jet yields is significantly closer to unity in the momentum-based method than in the structure-based method. The structure-based method shows heavy bias against anti-quarks.

Table 5.3: The table shows the fractional parton jet yields extracted at the 'particle level' using the structure-based and momentum-based methods from pp MC data. These yields have been normalised to unity.

Parton	Structure-Based Yields	Momentum-Based Yields
Up	0.2361 ± 0.0007	0.0729 ± 0.0002
Down	0.1518 ± 0.0005	0.0522 ± 0.0002
Gluon	0.5303 ± 0.0010	0.6996 ± 0.0006
Anti-Up	0.0128 ± 0.0002	0.0303 ± 0.0001
Anti-Down	0.0135 ± 0.0002	0.0308 ± 0.0001
Strange	0.0273 ± 0.0002	0.0218 ± 0.0001
Anti-Strange	0.0068 ± 0.0001	0.0220 ± 0.0001
Charm	0.0134 ± 0.0002	0.0170 ± 0.0001
Anti-Charm	0.0047 ± 0.0001	0.0169 ± 0.0001
Bottom	0.0041 ± 0.0001	0.0185 ± 0.0001
Anti - Bottom	0.0017 ± 0.00004	0.0178 ± 0.0001

One other logic check that can be performed here to investigate the yields is to investigate the ratio between the valence quark contribution to the jet yields. This ratio would be expected to be two as there are double the number of valence up quarks to down quarks. Of course, the yields as measured by jet charge cannot distinguish between sea-quark and valence-quark jets. Therefore, an approximation must be made to find the sea-up and sea-down quark contribution. This approximation is that the sea-up and sea-down quark contributions would be approximately equal to the anti-up and anti-down quark contributions. This is because both of these sets of quarks would be created in pairs and thus should exist in equal amounts. Using this approximation, the equation used to find this ratio is as follows,

$$\frac{u_{valence}}{d_{valence}} \approx \frac{u-\bar{u}}{d-\bar{d}} \approx 2, \tag{5.2}$$

where $u_{valence}$ and $d_{valence}$ are the up and down quark valence jet contribution, u and $\bar{u}$ are the jet yields of up and anti-up quarks and d and $\bar{d}$ are the jet contribution from down and anti-down quarks respectively. For the structure-based method, the result of this is 0.161, and for the momentum-based method, the result is 1.99. This is another advantage of the momentum-based method. These factors combine to once again support the momentum-based method over the structure-based counterpart.

It is possible to extract the yields from the MC data in Pb-Pb collisions before fitting, as was done with pp collisions to perform a sanity check. These yields are shown in table 5.4 and are presented in the extreme of most central and least central collisions to illustrate the maximum discrepancy. The differences between the yields in the most and least central collisions are minimal, approximately 1% in gluon yields. This is good as this means the presence of background in the data will not affect the yields significantly, and any observed effects could be caused by the QGP. The yields are similar to the yields extracted in pp collisions. This is to be expected as the embedded jets from the MC are pp jets. The data can similarly be investigated to show the relative yields of valence quarks as demonstrated in equation 5.2. For this check equation 5.2 yields a ratio of 1.67 in the most central collisions and 1.99 in the least central collisions. This discrepancy seems to be due to the larger anti-up quark yields extracted from the most central collisions. This discrepancy suggests that the background has a more significant factor on the parton yields than expected from the values alone.

The nature of the embedding technique means that the parton yields extracted from Pb-Pb collisions in the MC data will mirror that of pp collisions. This is because the MC is simulating the initial collision as though it were a pp collision. The effects of this are visible in the relative number of up-quark jets to down-quark jets. These effects must be corrected to better compare the MC results to real data (since Pb comprises of 82 protons and 126 neutrons which leads to a valence quark ratio of $\frac{u_{valence}}{d_{valence}} = 0.87$). In order to correct this, the templates in Pb-Pb must be reweighted to account for different initial parton numbers. This is done using the following equation,

$$q_{weighted} = (q_{init} - \bar{q}) \times C + \bar{q}, \tag{5.3}$$

where $q_{weighted}$ is the new quark yield, q_{init} is the initial quark yield, $\bar{q}$ is the initial anti-quark yield representing the sea quark contribution and C is a constant that varies depending on if up or down quark yields are being scaled. For up quarks $C = 0.7$ which is extracted by multiplying the fractional of up quarks in Pb-Pb nuclei divided by the ratio for the proton. Similarly, the corresponding ratio for down quarks is $C = 1.607$, which is the ratio of the down quarks instead. This equation should have the effect of scaling only the valence quark contribution of the up yields by the expected relative number of valence quarks in Pb-Pb collisions compared to Pb-Pb. Performing this weighting on the MC Pb-Pb events leads to the jet yields seen in table 5.5.

5.3 Template Fitting

The jet charge distribution from each type of jet can be integrated across all spaces to gain the yields of each type of jet. However, without fitting this to data, this would only return the yields generated directly from PYTHIA8 + Monash. Instead, these templates must be fitted using the data to extract the actual yields observed in the data. While the theory would predict that the MC events should accurately recreate the observed data, this is not a guarantee when dealing with a derived quantity such as the gluon yields from jet charge. The MC does not contain all the physics that may or may not be occurring in reality. For example, the MC does not simulate jet quenching. Thus, it is still required to fit the templates to investigate how the MC events' jet charge differs from the jet charge measured

Table 5.4: The table shows the fractional parton jet yields extracted from the MC for 0-10% Centrality and 80-90% Centrality for comparison. These yields have been normalised to unity.

Parton	Pb-Pb Yields 0-10% Cent	Pb-Pb Yields 80-90% Cent
Up	0.0784 ± 0.0004	0.0723 ± 0.0003
Down	0.0631 ± 0.0004	0.0563 ± 0.0003
Gluon	0.663 ± 0.001	0.6737 ± 0.0009
Anti-Up	0.0512 ± 0.0004	0.0456 ± 0.0003
Anti-Down	0.0468 ± 0.0003	0.0429 ± 0.0003
Strange	0.0341 ± 0.0003	0.0298 ± 0.0002
Anti-Strange	0.0315 ± 0.0003	0.0286 ± 0.0003
Charm	0.0217 ± 0.0002	0.0195 ± 0.0002
Anti-Charm	0.0215 ± 0.0002	0.0190 ± 0.0002
Bottom	0.0099 ± 0.0001	0.0083 ± 0.0001
Anti - Bottom	0.0091 ± 0.0001	0.0077 ± 0.0001

Table 5.5: The table shows the fractional parton jet yields extracted from the MC for $40-50\%$ centrality after manual up and down quark weightings have been applied. These yields have been normalised to unity.

Parton	Pb-Pb Yields Weighted
Up	0.0640 ± 0.0003
Down	0.0665 ± 0.0004
Gluon	0.6648 ± 0.0009
Anti-Up	0.0458 ± 0.0003
Anti-Down	0.0429 ± 0.0003
Strange	0.0302 ± 0.0003
Anti-Strange	0.0292 ± 0.0003
Charm	0.0198 ± 0.0002
Anti-Charm	0.0195 ± 0.0002
Bottom	0.00893 ± 0.0001
Anti - Bottom	0.00843 ± 0.0001

in the data.

The fitting needs to be conducted with care because of the similarity between each template. While it might seem simplest to fit the templates to the data by using a fitting parameter to control the amplitude of each template, this approach runs into issues as it has four fitting parameters. An increased number of fitting parameters leads to more difficulty in reaching a reliable fit. If the templates are not sufficiently different from each other, then there will be multiple minima in the fit. This will result in the templates being equally able to fit the data at multiple points, thus preventing the fitting from providing useful information. Therefore, to mitigate this possibility, some predictions about the fitting system are used to simplify the fitting algorithm.

Since the final step in the process is to see the effects of the QGP on the gluon yields, the gluon templates must be kept separate from the other templates in the fitting process. The expected suppression of gluon-like jets by the QGP is because of the colour charge of gluons. Since this is based on the colour charge, the suppression from the QGP is expected to affect quarks to a lesser degree than gluons. Additionally, quarks all experience colour interactions in the QGP in the same way, regardless of their flavour. Thus, if they were affected, the quarks would experience the same effect regardless of flavour. Therefore, their templates can be combined during the template fitting.

$$f_{\mathrm{JetCharge}} = C_1 f_g + C_2 f_q, \tag{5.4}$$

Where C_1 and C_2 are both constants found during fitting, which best match $f_{\mathrm{JetCharge}}$ to the unfolded data, similarly, f_g and f_q are functions derived by interpolating the histograms for the gluon and quark templates. This simplified approach allows the fitting algorithm to focus only on two combined templates. The width of the templates is the primary difference between the gluon template and the combined quark template. The quark template is wider than the gluon template, as seen in figure 5.16. However, it is worth noting that this is not true at the edges of the jet charge distribution. Instead, the difference in shape could be more accurately described as a bulge at the mid-values of jet charge that results from the positive and negative shifts of the quark templates. When it comes to fitting, however, this distinction is minor as these extremities will have the largest uncertainty.

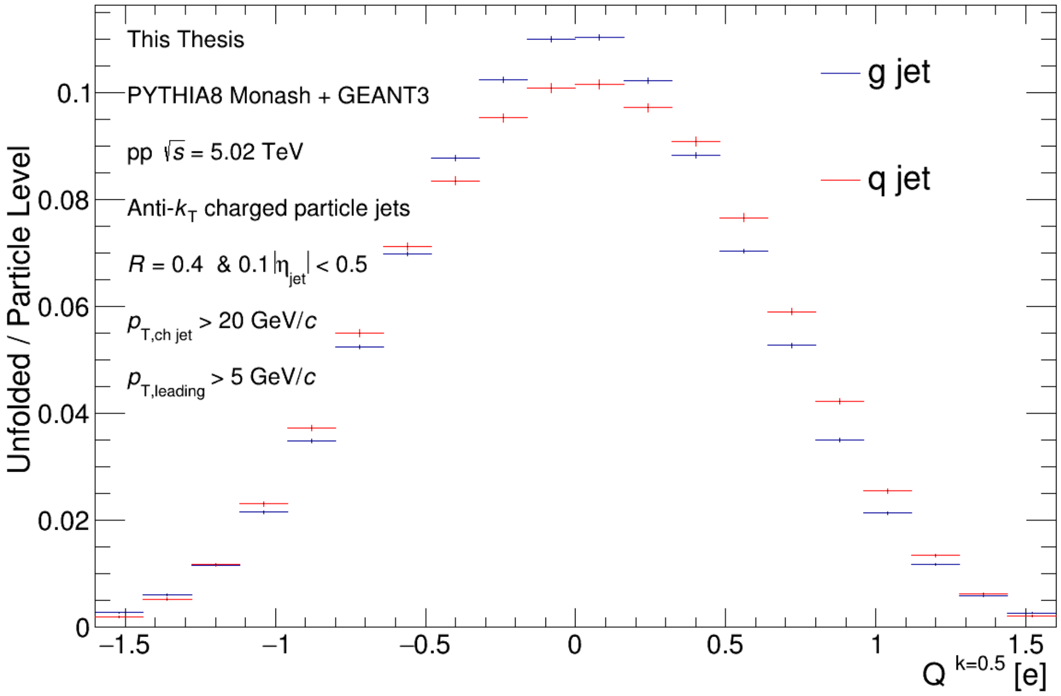

Figure 5.16: The figure shows normalised jet charge functions that will be used in the fit to the data. These functions are the gluon template, f_g, and the combined remaining 'quark' template, f_q. The main distinction is that the quark template is wider than the gluon template.

The inbuilt ROOT fitting method reports the statistical error on the fit. These are listed with the fit in the table 5.6. A larger concern is the consistency of the fit. This concern arises because these templates are very similar to each other and the data; thus, small changes can introduce significant variances in the fitting algorithm. Thus, a closure test is shown here to demonstrate the consistency of the fitting.

The closure test randomly splits the MC data into two different sets of data. For the test process, one of these data sets will be treated as though it is the measured data, and the second set will be used to generate the templates. It will then fit the templates to the first set and attempt to extract the quark and gluon fractions. An example of this closure fit can be seen in figure 5.17, which shows the fitting achieving a closure of 1 with the randomly selected test data with an error of 0.056.

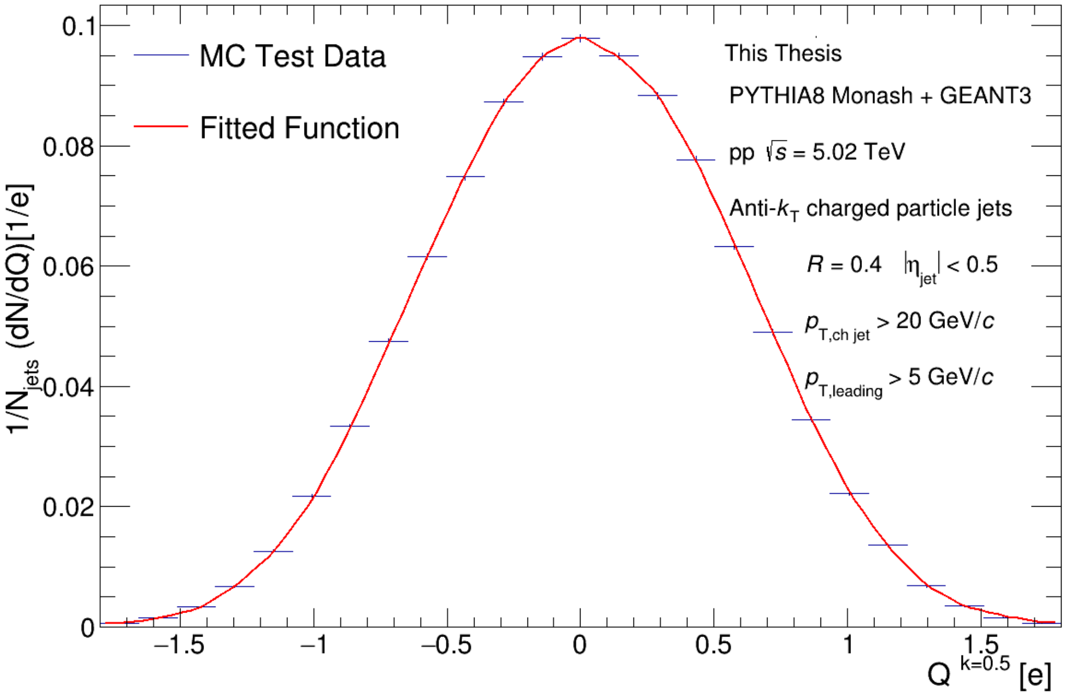

Figure 5.17: The figure shows the MC test jet charge distribution generated randomly from half the data, and the red line shows the fitted results. The templates have been able to reproduce the test data with a maximum error of 5.6%.

As seen in figure 5.17 and table 5.6, the closure test can successfully fit one half of the MC data to the other. This closure suggests that it will be possible to do the same for the data providing that the jet charge distributions in pp and Pb-Pb do not have any fundamental differences. Additionally, the closure test can be further pushed to test for consistency if the test is run with multiple repetitions to reshuffle the random selection of jets creating two new samples. It can be seen that there is some instability in the fitting.

Table 5.6: The table shows the results of the ROOT fitting system when run for the closure test with errors calculated using the Minos technique and the "IMPROVE" algorithm from TMinuit. The value of unity would represent complete closure as this would show the randomly selected half of the data perfectly match the other half. The parameters C_1 and C_2 represent the "Gluon" and "Quark" constants, respectively, as given in equation 5.4. These fits are for pp MC data.

Parameter	Value	Error	Size	Derivative
C_1	0.984284	0.0270130	-0.00007	-0.799911
C_2	1.03216	0.0565983	0.0565983	-0.0000939930

Over 100 repeats of the closure test, the average separation from unity for the closure test is 0.032, with none of the fitting results being over 0.1 from unity when calculating the ratio between the fit and the jet charge from the MC data sample.

5.4 Fitting Yields results

Fitting the jet charge distribution templates to the data allows the extraction of the gluon-like jet yields. Fitting in pp is important for two reasons: first, to check that the MC accurately represents the data. Secondly, to be a point of comparison for the Pb-Pb yields. Using the same method with both pp and Pb-Pb allows the yields to be compared as it is a relative reduction that is expected. Since the reduction in the gluon-like jet fraction should be from effects absent in pp, which could be the QGP, these yields are shown for $0-90\%$ centrality in Pb-Pb in figure 5.18, with each bin covering a range of 10 centralities. This allows a comparison of more central collisions, which should have stronger effects from the QGP, to less central collisions with less QGP.

As seen in figure 5.18, the effects of the QGP on the gluon yields remain unclear.

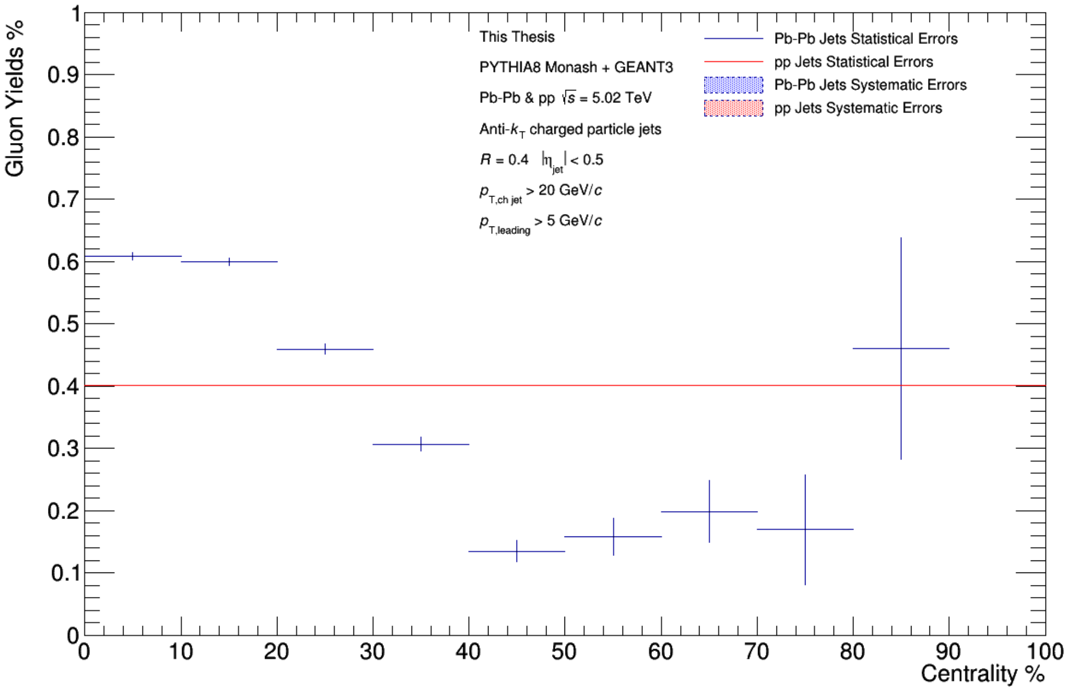

Figure 5.18: The figure shows the fitted gluon yields for a given centrality in Pb-Pb collisions as well as for all pp collisions. The figure shows a decrease in the gluon yields at the $30-80\%$ centrality range. However, it also shows an increase in the gluon yields at high centrality ranges. This suppression is likely a consequence of the increasingly dominant background in more central collisions.

There is a decrease in the gluon jet yields $30-80\%$ Pb-Pb centrality range compared to that in pp. These effects become stronger as Pb-Pb collisions become more central from $40-80\%$. However, the gluon yields increase once again in more central Pb-Pb collisions $0-40\%$, which is the opposite of what is predicted. Finally, the Pb-Pb collisions within the $80-90\%$ centrality bin also has significantly higher gluon yields than the pp. This increase is also unexpected, but there are several ways for which this discrepancy can be accounted. The final $80-90\%$ centrality bin has significantly higher uncertainty when compared to the other bins. This uncertainty is because as the centrality increases, the number of jets decreases, thus, decreasing the available statistics. This is because the probability of a hard parton scattering is less as the overlap between the colliding Pb nuclei decreases. Thus, the final bin may be simply a consequence of the fitting being less confident due to this lack of statistics. This can be seen in the error bars in figure 5.18.

The question of the increasing gluon-like jet yields observed for more central collisions is more complex. In more central collisions, the density of background particles increases. As the number of background particles increases, the chances of background particles being clustered into a given jet also increase. These soft background particles that are clustered into the jet will affect the jet charge of that jet. One would expect this random change to be independent of the gluon jet yields. However, since these random background particles have a random charge, they have a jet charge distribution which is narrower. Thus, when the jet charge is measured in the most central Pb-Pb collisions, the effects of the shifted quark jets are mitigated by the inclusion of these soft particles. This results in the jet yield in the most central collisions appearing to be more "Gluon-like" in the data due to the background influence.

In terms of fitting, the primary distinction between the gluon-like and the quark-like templates is their relative width. This difference is because the gluon-like template is centred around zero, and the quark-like templates are combined from positively and negatively shifted templates. Thus, background particles in more central collisions could be shifting the jet charge in the data to appear more gluon-like, thus obfuscating the true effect of the QGP on the jets in these more central collisions.

In order to investigate this, templates were constructed and fit using the same parameters with the exception of using a higher $p_{t,\text{track}}$ cut. The intention behind this is that a larger $p_{t,\text{track}}$ allows better separation between the background and the particles of the jet by only allowing higher momentum particles to be selected. In this case, the $p_{t,\text{track}}$ is set to a value of 800 MeV/c instead of the typical ALICE acceptance of 150 MeV/c. This value was chosen in order to maintain a reasonable number of particles in jets while being substantially above the typical acceptance. The results of these templates can be seen in figure 5.19. As can be seen from the figure, the results of a higher track $p_{t,\text{track}}$ cut are consistent with what is seen at the original lower track $p_{t,\text{track}}$. It seems that the higher track $p_{t,\text{track}}$ cut is unable to sufficiently counter the effects of higher multiplicity events in the most central Pb-Pb collisions. This was tested again with a higher $p_{t,\text{track}}$ cut of $p_{t,\text{track}} > 3000$ MeV/c. However, this higher $p_{t,\text{track}}$ reduced the statistics available significantly, leading to an unusable sample.

5.5 Systematic Errors

It is essential to consider systematic errors when discussing these yields as these errors may dominate over the statistical errors. Three primary sources of systematic errors in the gluon yields will be discussed below:

- Detector tracking efficiency.
- Choice of the MC generator.
- Regulation parameter in the unfolding process.

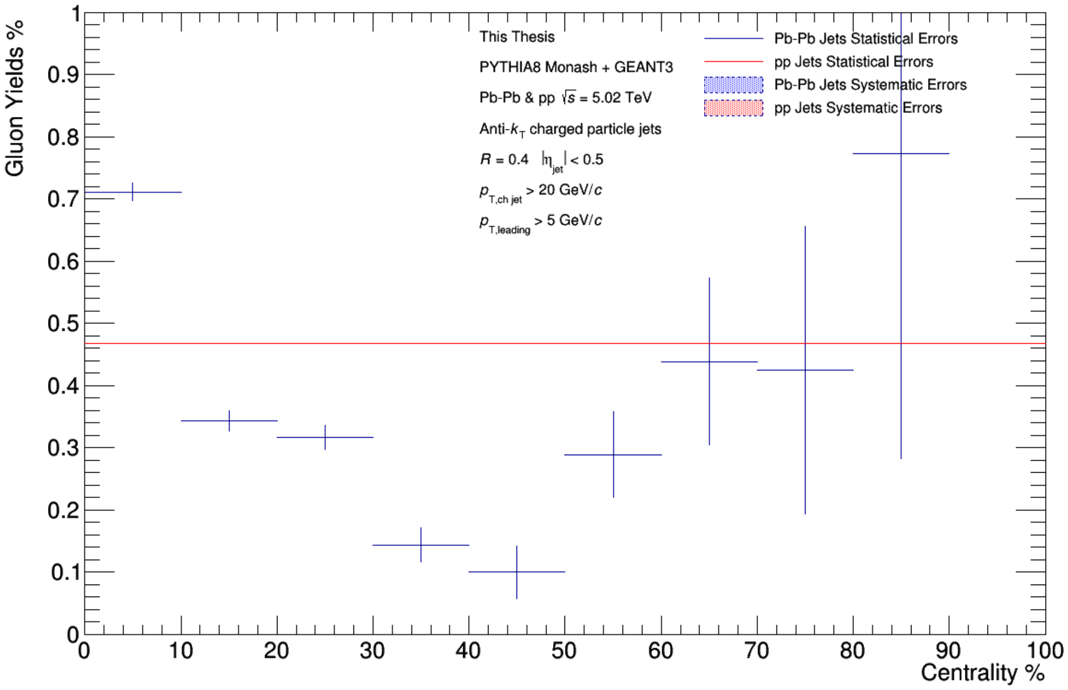

Figure 5.19: The figure shows the fitted gluon yields for a given centrality in Pb-Pb collisions as well as for all pp collisions for a higher $p_{t,\text{track}} > 800$ MeV/c. This shows that the reduction of the gluon yields is consistent with what is seen with the original $p_{t,\text{track}}$ cut. Note that in this figure the systematic error is not included.

5.5.1 Track efficiency

The ALICE detector has a known inefficiency regarding when a track is detected. However, there is an uncertainty with this inefficiency of about 2%. Thus, a systematic uncertainty is determined by running the analysis framework with an additional parameter. This parameter means that for each particle, there is a 2% chance that the track is removed from the event and not considered during jet finding. This removal simulates the detector's true efficiency, potentially being % lower than the accepted value. Conducting this analysis and comparing the results leads to a systematic uncertainty in the gluon yields of 2.97%.

5.5.2 Generator Choice

There is a further systematic uncertainty relating to the choice of MC generator used to generate the templates. The MC generator used is the PYTHIA8 generator. A second sample of MC data is produced using a different generator. Comparing these two sets of templates makes it possible to determine the size of this systematic error. In this case the POWHEG and PYTHIA8 generators are used, where POWHEG is used to simulate the initial hard scatter, and PYTHIA8 is used to propagate the parton shower. Theoretically, this approach should better simulate known physics because POWHEG is used to simulate the next leading-order effects. However, it is significantly more computationally expensive than simply using PYTHIA8 with the Monash tuning and thus is not used as the main production generator for the ALICE collaboration. Unfortunately, due to this limitation, there are no fully prepared POWHEG data sets available to the Jet Physics Working group at ALICE. Using locally generated POWHEG, it is possible to investigate the difference between the generators at the particle level. The 'particle level' yields for gluon jets for PYTHIA and POWHEG are shown in table 5.7. The table shows that the parton yields at the 'particle level' for PYTHIA and POWHEG are largely in agreement, with the largest difference coming from the antiparticle contribution of anti-up and anti-down at approximately 1.4%.

Table 5.7: The table shows the normalised parton jet yields extracted at the 'particle level' for POWHEG and PYTHIA as a fraction of the total number of jets.

Parton	POWHEG Yields	PYTHIA Yields
Up	0.0729 ± 0.0002	0.0718 ± 0.0004
Down	0.0522 ± 0.0002	0.0563 ± 0.0004
Gluon	0.6996 ± 0.0006	0.6728 ± 0.0011
Anti-Up	0.0303 ± 0.0001	0.0447 ± 0.0003
Anti-Down	0.0308 ± 0.0001	0.0426 ± 0.0003
Strange	0.0218 ± 0.0001	0.0287 ± 0.0003
Anti-Strange	0.0220 ± 0.0001	0.0278 ± 0.0003
Charm	0.0170 ± 0.0001	0.0198 ± 0.0002
Anti-Charm	0.0169 ± 0.0001	0.0188 ± 0.0002
Bottom	0.0185 ± 0.0001	0.0086 ± 0.0001
Anti - Bottom	0.0178 ± 0.0001	0.0084 ± 0.0001

In addition, figure 5.20 shows the ratio between the gluon templates for both POWHEG and PYTHIA8 generators. While these differences do not translate directly into the gluon yields, it is interesting to note in what way the generator choice affects the templates.

5.5.3 Unfolding statistics

The unfolding software uses a Bayesian method. This method requires the user to specify a regulation parameter in the software. In this case, it is the number of iterations in the Bayesian method. The ideal number of iterations can be determined by comparing the results in a closure test. The ideal number is found when the size difference iterations are smaller than the error on that value. The RooUnfold creators recommend using a small value greater than zero. Using more iterations can be counterproductive because of the increased computational power needed. The increasing number of iterations also follows with an increasing error in the output. As mentioned earlier in section 4.3, the ideal number of iterations found to be used in this analysis is 2.

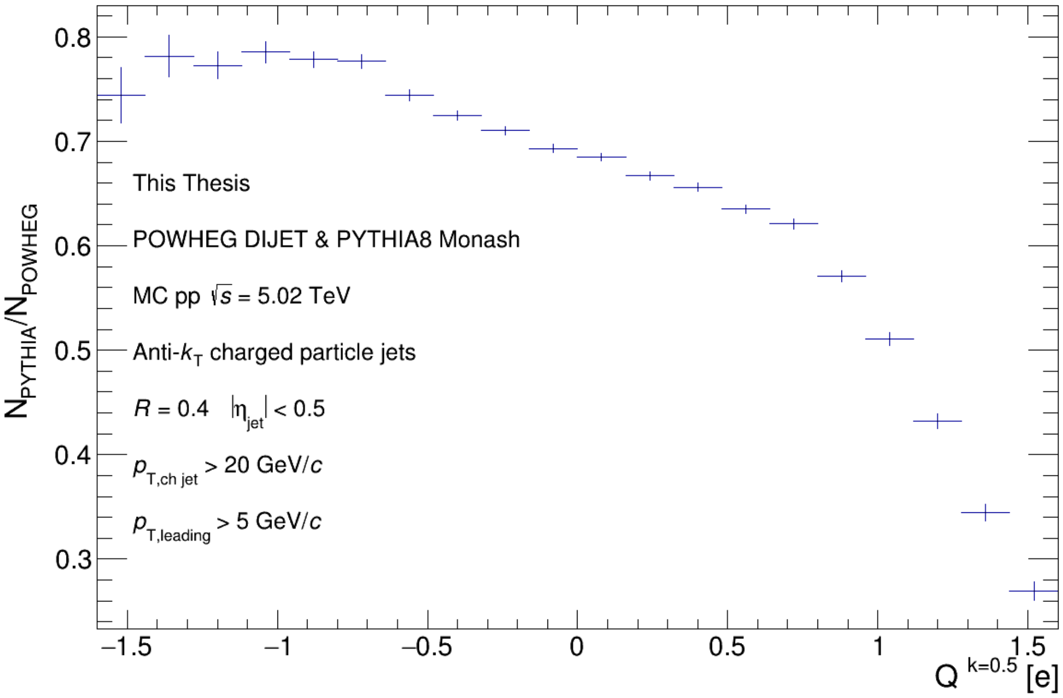

Figure 5.20: The figure shows the ratio between the gluon templates for the POWHEG Dijet generator and the PYTHIA8 Monash generator. It is possible to see that these templates are similar for most of the range, except for the POWHEG template having larger overall gluon yields. The main discrepancy, though, happens at a high positive jet charge, which suggests that the PYTHIA8 distribution has a positive tail not seen in the POWHEG.

When equipped with this knowledge, measuring the systematic error associated with the unfolding procedure becomes possible. This measurement is done by performing the fitting of the jet charge templates twice, once with the standard regulation parameter and the second using a single iteration. The difference between these results can then be used as a systematic error.

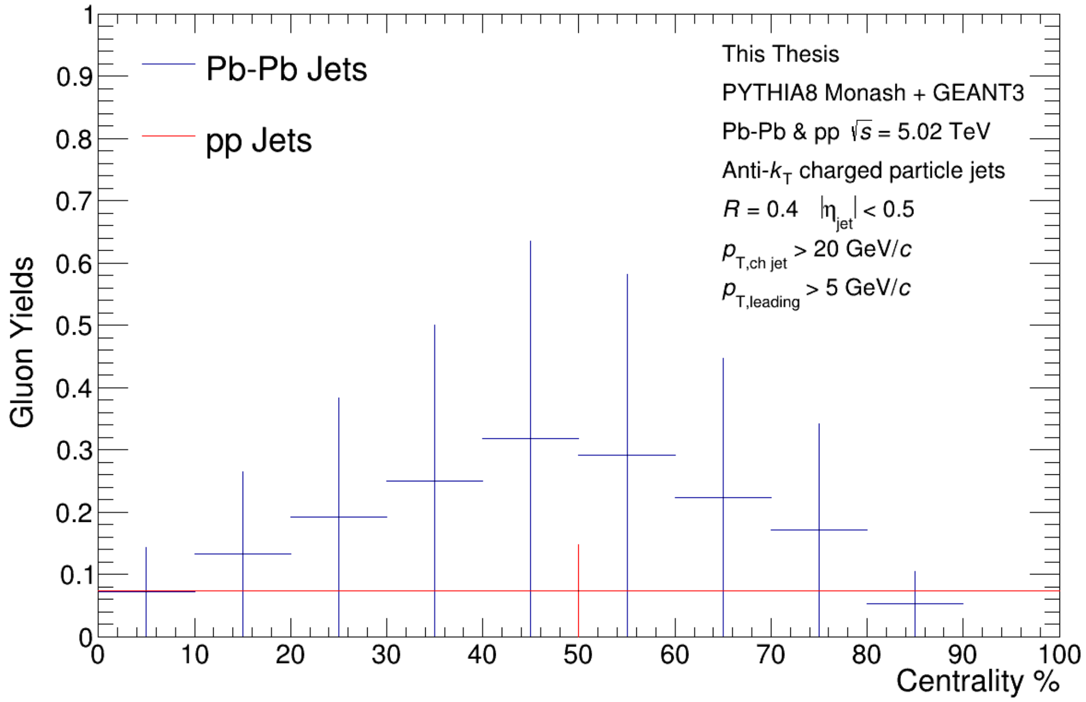

Figure 5.21: The figure shows the systematic error from the unfolding selection. This error is shown as a ratio between the ideal number of unfolding iterations and a single iteration.

It can be seen in figure 5.21 that the systematic errors for unfolding are significantly higher than those seen from the choice of MC generator and the tracking efficiency. It is also seen that these errors increase in the mid-centrality range.

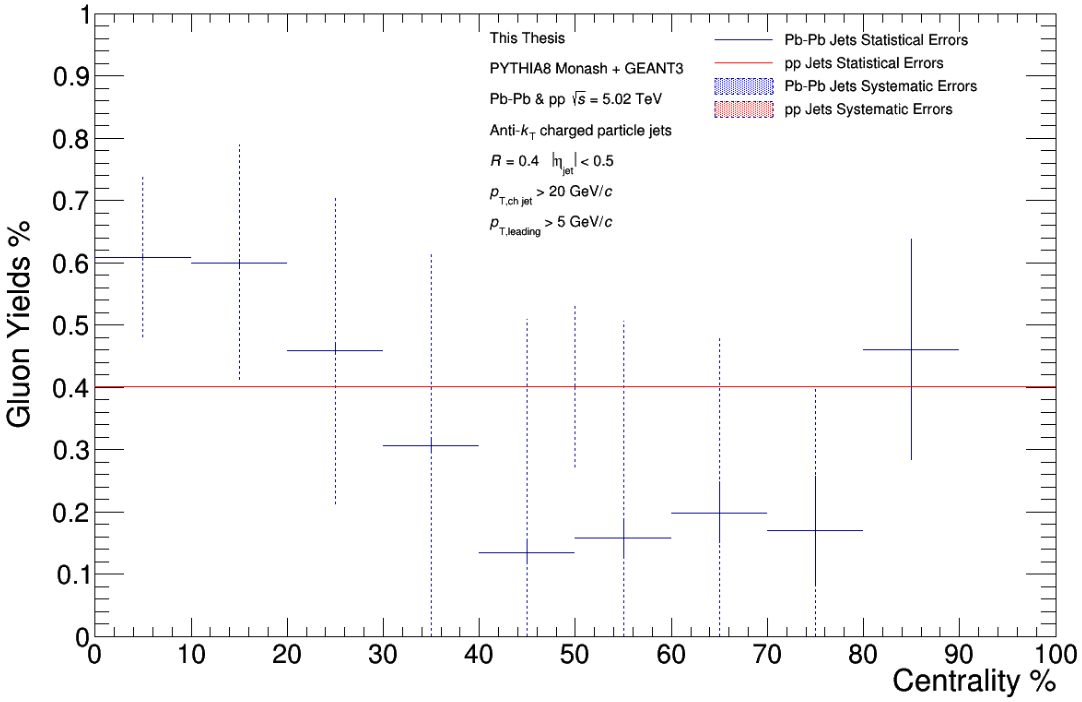

Figure 5.22: The figure shows the fitted gluon yields for a given centrality in Pb-Pb collisions as well as for all pp collisions. Unlike figure 5.18, this figure includes the contribution of the systematic uncertainties brought about by track efficiency, choice of MC generator and unfolding parameter. It is clear from this figure that these dominate over the statistical errors.

5.5.4 Systematic Error Summary

As seen by comparing figures 5.22 and 5.18, the systematic error from unfolding dominates over the statistical errors. The systematic errors' effects are sufficient enough that were they to shift the templates towards reduced gluon yields, this would suggest that pp and Pb-Pb do line up in the most and the least central collisions. Alternatively, if the systematic suggests an increased gluon yield from what is seen, that would mask all effects of the Pb-Pb collisions on the jet charge in the $30-80\%$ centrality ranges. This effect is a testament to the difficulty of using these templates to perform these fits, as even in their most refined state, the systematic errors dominate over any changes seen from the fitting. These systematic errors do not invalidate the possibility that the data show a gluon-like jet suppression from the QGP. However, it is clear that, similar to dealing with the background effects, as much as possible needs to be done to minimise these systematic errors.

5.6 Discussion and Conclusion

There are three main sections of this analysis to be discussed. First is how the templates themselves are generated, the methods used and how it compares to what has been previously seen. Second is the effectiveness of using these techniques in Pb-Pb collisions and what effects the background has on these techniques. Finally, examining the yields that result from the fitting and how these yields differ in pp and Pb-Pb collisions.

The template generation itself, in particular the technique for identifying the progenitor parton, provides an interesting avenue of discussion. It is clear that, like jets, the templates are constructed objects that depend on the choice of parameters. It is because of this nature that it is not a simple matter of finding the "correct" jet charge template. Instead, it is a question of finding the ideal set of parameters for the goals of the analysis.

However, there are still comparisons to be made to ensure that the templates are of good quality. Compared to the templates produced by CMS's analysis shown in section 1.4.1 on the jet charge then, the templates seem promising. Similar to the templates found from CMS, the gluon yields dominate the sample, followed by up quark contributions and then heavier quark contribution. The mean values found for templates using the structure technique are significantly lower than those found by CMS by around a factor of five. This can be mitigated by increasing the minimum transfer momentum of a jet to bring it closer to the means shown by CMS, but this becomes unnecessary when considering the momentum-based templates. The means of the momentum-based templates are larger than those found by CMS (with the exception of gluons), showing that the significantly larger momentum acceptance of CMS is not required to show significant separation between up quark jet charge and down quark jet charge. CMS reports approximately $55 - 58\%$ gluon-like jet fraction depending on the track p_T cut used. This is above the 48.5% found in this analysis by fitting the templates at the particle level. Many of the differences between the templates found in this analysis compared to those found in CMS are likely to be a result of the differing acceptance range of the detectors. The majority of the data presented in this analysis have been for jets with a transverse momentum larger than 20 GeV/c. This is significantly smaller than the CMS analysis, which considers jets with greater than 80 GeV/c; depending on the technique used to find the progenitor partons that CMS uses, the resulting templates could be significantly affected. Additionally, CMS has a significantly higher track p_T cut of > 1 GeV/c. This higher track p_T cut is significantly larger than the 0.15 GeV/c track p_T cut of the ALICE detector. This will result in a significant number of low-momentum tracks being lost by the CMS detector. This could result in some of the charge information from the progenitor parton being lost in low momentum particles. This could explain the larger means found using the momentum-based method when compared to CMS.

The extraction of jet charge templates in Pb-Pb collisions has been largely successful.

Jet charge templates have been extracted for $0 - 90\%$ centrality. For the most central collisions, the effects of the background become more significant. This background influence is observed in the reduced ratio of jets from valence-up quarks to valence-down quarks in the most central Pb-Pb collisions when compared to the less central collisions. Fine tuning the background subtraction technique to minimise the background effects in these most central collisions could be one avenue to improving the extraction of yields in the most central collisions.

Demonstrating the suppression of gluon-like jets by the QGP remains elusive. Many of the results shown align with what would be expected from CMS's earlier experimentation. The exception to this is this analysis's demonstration of evidence of suppression of gluon-like jets in mid-centrality collisions. These mid-centrality collisions provide the best conditions for the techniques used. This is because the minimum centrality bin, $80-90\%$, has low statistics, and the most central collisions likely contend with the increased background associated with central collisions. As discussed previously, the effects of the increased background would be that more particles which were not from the progenitor parton of the jet are clustered into the jet, and similarly, more particles that were from the progenitor parton are lost. The effect of this would be to "dilute" the influence of the progenitor parton. This dilution would cause the shifts from the electrical charge of the progenitor quarks to be less significant. The effect of this would be making quark-like jets appear closer to gluon-like jets when the jet charge is measured. This could result in the increased gluon jet yields extracted from the most central collisions. It is possible that the background effects are being significantly mitigated, and instead that the observed measurement is the result of the predictions for gluon suppression by the QGP being incorrect. In this case the observed results will point to an unexplained part of physics. However, to demonstrate this more work would need to be done to ensure that that background effects were being sufficiently mitigated.

Overcoming these limitations poses a significant challenge for future work to develop on. The key would be to find a way to maintain the progenitor parton information from the jet charge in the most central collisions. This could potentially be done with enough time to adjust the parameters to minimise the background effects. These would include testing a higher $p_{T,jet}$ cut to increase the jet separation from the background and a higher track p_T cut to minimise the number of low momentum particles. However, this has the consequence of reducing the unique parameter space the ALICE detector can explore. By increasing the track p_T cut, low momentum particles from the progenitor parton will also be lost, and thus, the particle's effect on the jet charge is also lost. Run 3 could provide some possibility for an expansion of this work. The order of magnitude increase in statistics will make a jet momentum cut of 80 GeV/c possible without becoming statistics limited.

In conclusion, the challenge of showing gluon-like jet suppression by the QGP remains a challenge for a reason. This analysis shows some evidence of suppression of gluon-like jets in mid-centrality ranges in Pb-Pb collisions at 5.02 TeV, but measurements in the most and least central collisions remain a challenge to overcome.

References

[1] Wikipedia contributors. *Standard Model — Wikipedia, The Free Encyclopedia.* [Online; accessed 7-August-2023]. 2023. URL: https://en.wikipedia.org/w/index.php?title=Standard_Model&oldid=1166898021.

[2] Murray Gell-Mann. “A Schematic Model of Baryons and Mesons”. In: *Phys. Lett.* 8 (1964), pp. 214–215. DOI: 10.1016/S0031-9163(64)92001-3.

[3] G. Zweig. “An SU(3) model for strong interaction symmetry and its breaking. Version 2”. In: *DEVELOPMENTS IN THE QUARK THEORY OF HADRONS. VOL. 1. 1964 - 1978.* Ed. by D.B. Lichtenberg and Simon Peter Rosen. Feb. 1964, pp. 22–101.

[4] Sheldon L. Glashow. “Partial-symmetries of weak interactions”. In: *Nuclear Physics* 22.4 (1961), pp. 579–588. ISSN: 0029-5582. DOI: https://doi.org/10.1016/0029-5582(61)90469-2. URL: https://www.sciencedirect.com/science/article/pii/0029558261904692.

[5] Steven Weinberg. “A Model of Leptons”. In: *Phys. Rev. Lett.* 19 (21 Nov. 1967), pp. 1264–1266. DOI: 10.1103/PhysRevLett.19.1264. URL: https://link.aps.org/doi/10.1103/PhysRevLett.19.1264.

[6] Abdus Salam. “Weak and Electromagnetic Interactions”. In: *Conf. Proc. C* 680519 (1968), pp. 367–377. DOI: 10.1142/9789812795915_0034.

[7] D. J. Gross and Frank Wilczek. “Asymptotically Free Gauge Theories - I”. In: *Phys. Rev. D* 8 (1973), pp. 3633–3652. DOI: 10.1103/PhysRevD.8.3633.

[8] Steven Weinberg. “Non-Abelian Gauge Theories of the Strong Interactions”. In: *Phys. Rev. Lett.* 31 (7 Sept. 1973), pp. 494–497. DOI: 10.1103/PhysRevLett.31.494. URL: https://link.aps.org/doi/10.1103/PhysRevLett.31.494.

[9] H. Fritzsch, Murray Gell-Mann, and H. Leutwyler. “Advantages of the Color Octet Gluon Picture”. In: *Phys. Lett. B* 47 (1973), pp. 365–368. DOI: 10.1016/0370-2693(73)90625-4.

[10] R. L. Workman et al. “Review of Particle Physics”. In: *PTEP* 2022 (2022), p. 083C01. DOI: 10.1093/ptep/ptac097.

[11] Harald Fritzsch. “Light Cone Current Algebra”. In: *Murray Gell-Mann and the Physics of Quarks*. Cham: Springer International Publishing, 2018, pp. 53–87. ISBN: 978-3-319-92195-2. DOI: 10.1007/978-3-319-92195-2_6. URL: https://doi.org/10.1007/978-3-319-92195-2_6.

[12] E. Eichten et al. “The Spectrum of Charmonium”. In: *Phys. Rev. Lett.* 34 (1975). [Erratum: Phys.Rev.Lett. 36, 1276 (1976)], pp. 369–372. DOI: 10.1103/PhysRevLett.34.369.

[13] Nora Brambilla et al. “Potential NRQCD: an effective theory for heavy quarkonium”. In: *Nuclear Physics B* 566.1-2 (Jan. 2000), pp. 275–310. DOI: 10.1016/s0550-3213(99)00693-8. URL: https://doi.org/10.1016%5C%2Fs0550-3213%5C%2899%5C%2900693-8.

[14] Gunnar S. Bali, Nora Brambilla, and Antonio Vairo. “A lattice determination of QCD field strength correlators”. In: *Physics Letters B* 421.1-4 (Mar. 1998), pp. 265–272. DOI: 10.1016/s0370-2693(97)01583-9. URL: https://doi.org/10.1016%5C%2Fs0370-2693%5C%2897%5C%2901583-9.

[15] Vardan Khachatryan and Helen Heath. “Measurement of the inclusive 3-jet production differential cross section in proton–proton collisions at 7 TeV and determination of the strong coupling constant in the TeV range”. In: *European Physical Journal C: Particles and Fields* C75.5 (2015), p. 186. ISSN: 1434-6044. DOI: 10.1140/epjc/s10052-015-3376-y.

[16] Bogdan Malaescu and Pavel Starovoitov. “Evaluation of the Strong Coupling Constant α_s Using the ATLAS Inclusive Jet Cross-Section Data”. In: *Eur. Phys. J. C* 72 (2012), p. 2041. DOI: 10.1140/epjc/s10052-012-2041-y. arXiv: 1203.5416 `[hep-ph]`.

[17] David J. Gross and Frank Wilczek. “Ultraviolet Behavior of Nonabelian Gauge Theories”. In: *Phys. Rev. Lett.* 30 (1973). Ed. by J. C. Taylor, pp. 1343–1346. DOI: 10.1103/PhysRevLett.30.1343.

[18] Mingshen Gao. “Debye screening in the QCD gluonic plasma”. In: *Phys. Rev. D* 41 (2 Jan. 1990), pp. 626–633. DOI: 10.1103/PhysRevD.41.626. URL: https://link.aps.org/doi/10.1103/PhysRevD.41.626.

[19] Frithjof Karsch, Edwin Laermann, and A Peikert. “Quark mass and flavour dependence of the QCD phase transition”. In: *Nuclear Physics B* 605.1-3 (2001), pp. 579–599.

[20] A Ali Khan et al. “Phase structure and critical temperature of two-flavor QCD with a renormalization group improved gauge action and clover improved Wilson quark action”. In: *Physical review D* 63.3 (2000), p. 034502.

[21] Johann Rafelski and Berndt Müller. “Strangeness production in the quark-gluon plasma”. In: *Physical Review Letters* 48.16 (1982), p. 1066.

[22] Tetsuo Matsui and Helmut Satz. “J/ψ suppression by quark-gluon plasma formation”. In: *Physics Letters B* 178.4 (1986), pp. 416–422.

[23] B.B Back et al. “The PHOBOS detector at RHIC”. In: *Nuclear Instruments and Methods in Physics Research Section A: Accelerators, Spectrometers, Detectors and Associated Equipment* 499.2 (2003). The Relativistic Heavy Ion Collider Project: RHIC and its Detectors, pp. 603–623. ISSN: 0168-9002. DOI: https://doi.org/10.1016/S0168-9002(02)01959-9. URL: http://www.sciencedirect.com/science/article/pii/S0168900202019599.

[24] M Adamczyk et al. “The BRAHMS experiment at RHIC”. In: *Nuclear Instruments and Methods in Physics Research Section A: Accelerators, Spectrometers, Detectors and Associated Equipment* 499 (Mar. 2003), pp. 437–468. DOI: 10.1016/S0168-9002(02)01949-6.

[25] L. Greiner et al. “Experience from the construction and operation of the STAR PXL detector”. In: *Journal of Instrumentation* 10.04 (Apr. 2015), pp. C04014–C04014. DOI: 10.1088/1748-0221/10/04/c04014. URL: https://doi.org/10.1088%5C%2F1748-0221%5C%2F10%5C%2F04%5C%2Fc04014.

[26] R Ichimiya et al. “Status and overview of development of the silicon pixel detector for the PHENIX experiment at the BNL RHIC”. In: *Journal of Instrumentation* 4.05 (May 2009), P05001–P05001. DOI: 10.1088/1748-0221/4/05/p05001. URL: https://doi.org/10.1088%5C%2F1748-0221%5C%2F4%5C%2F05%5C%2Fp05001.

[27] Khea Ackermann et al. “Elliptic Flow in Au+Au Collisions at $\sqrt{s_{NN}} = 130$ GeV”. In: *Physical Review Letters* 86.3 (2001), p. 402.

[28] K Adcox et al. “Suppression of Hadrons with Large Transverse Momentum in Central Au+Au Collisions at $\sqrt{s_{NN}}= 130$ GeV”. In: *Physical Review Letters* 88.2 (2001), p. 022301.

[29] C. Adler et al. “Centrality Dependence of High-p_T Hadron Suppression in Au+Au Collisions at $\sqrt{s_{NN}} = 130$ GeV”. In: *Phys. Rev. Lett.* 89 (20 Oct. 2002), p. 202301.

DOI: 10.1103/PhysRevLett.89.202301. URL: https://link.aps.org/doi/10.1103/PhysRevLett.89.202301.

[30] STAR collaboration et al. "Transverse-Momentum and Collision-Energy Dependence of High-p_T Hadron Suppression in Au+Au Collisions at Ultrarelativistic Energies". In: *Physical Review Letters* 91.17 (2003), pp. 1723021–1723026.

[31] Stephen Scott Adler et al. "High-p_T charged hadron suppression in Au+Au collisions at $\sqrt{s_{NN}} = 200$ GeV". In: *Physical Review C* 69.3 (2004), p. 034910.

[32] John Adams et al. "Evidence from d+Au Measurements for Final-State Suppression of High- p_T Hadrons in Au+Au Collisions at RHIC". In: *Physical Review Letters* 91.7 (2003), p. 072304.

[33] The ALICE Collaboration et al. "The ALICE experiment at the CERN LHC". In: *Journal of Instrumentation* 3.08 (Sept. 2008), S08002–S08002. DOI: 10.1088/1748-0221/3/08/s08002. URL: https://doi.org/10.1088%5C%2F1748-0221%5C%2F3%5C%2F08%5C%2Fs08002.

[34] Reinhard Stock. "7 Relativistic Nucleus-Nucleus Collisions and the QCD Matter Phase Diagram". In: *Theory and Experiments*. Springer Berlin Heidelberg, 2008, pp. 225–315. DOI: 10.1007/978-3-540-74203-6_7. URL: https://doi.org/10.1007%5C%2F978-3-540-74203-6_7.

[35] Megan Connors et al. "Jet measurements in heavy ion physics". In: *Reviews of Modern Physics* 90.2 (2018), p. 025005.

[36] K. Aamodt et al. "Two-pion Bose–Einstein correlations in central Pb–Pb collisions at $\sqrt{s_{NN}} = 2.76$ TeV". In: *Physics Letters B* 696.4 (Feb. 2011), pp. 328–337. ISSN: 0370-2693. DOI: 10.1016/j.physletb.2010.12.053. URL: http://dx.doi.org/10.1016/j.physletb.2010.12.053.

[37] Wojciech Broniowski and Wojciech Florkowski. “Geometric relation between centrality and the impact parameter in relativistic heavy-ion collisions”. In: *Physical Review C* 65.2 (Jan. 2002). DOI: 10.1103/physrevc.65.024905. URL: https://doi.org/10.1103%5C%2Fphysrevc.65.024905.

[38] K. Aamodt et al. “Suppression of charged particle production at large transverse momentum in central Pb-Pb collisions at $\sqrt{s_{NN}} = 2.76$ TeV”. In: *Physics Letters B* 696.1-2 (Jan. 2011), pp. 30–39. DOI: 10.1016/j.physletb.2010.12.020. URL: https://doi.org/10.1016%5C%2Fj.physletb.2010.12.020.

[39] Yen-Jie Lee and. “Nuclear modification factors from the CMS experiment”. In: *Journal of Physics G: Nuclear and Particle Physics* 38.12 (Nov. 2011), p. 124015. DOI: 10.1088/0954-3899/38/12/124015. URL: https://doi.org/10.1088%5C%2F0954-3899%5C%2F38%5C%2F12%5C%2F124015.

[40] J. Adams et al. “Transverse-Momentum and Collision-Energy Dependence of High-p_T Hadron Suppression in Au+Au Collisions at Ultrarelativistic Energies”. In: *Physical Review Letters* 91.17 (Oct. 2003). DOI: 10.1103/physrevlett.91.172302. URL: https://doi.org/10.1103%5C%2Fphysrevlett.91.172302.

[41] S. S. Adler et al. “High-p_T charged hadron suppression in Au+Au collisions at $\sqrt{s_{NN}}$=200GeV”. In: *Physical Review C* 69.3 (Mar. 2004). DOI: 10.1103/physrevc.69.034910. URL: https://doi.org/10.1103%5C%2Fphysrevc.69.034910.

[42] Jacek Otwinowski and. “Charged particle production at large transverse momentum in Pb–Pb collisions at $\sqrt{s_{NN}} = 2.76$ TeV measured with ALICE at the LHC”. In: *Journal of Physics G: Nuclear and Particle Physics* 38.12 (Nov. 2011), p. 124112. DOI: 10.1088/0954-3899/38/12/124112. URL: https://doi.org/10.1088%5C%2F0954-3899%5C%2F38%5C2F12%5C%2F124112.

[43] and S. Acharya et al. “Transverse momentum spectra and nuclear modification factors of charged particles in pp, p-Pb and Pb-Pb collisions at the LHC”. In: *Journal of High

Energy Physics 2018.11 (Nov. 2018). DOI: 10.1007/jhep11(2018)013. URL: https://doi.org/10.1007%5C%2Fjhep11%5C%282018%5C%29013.

[44] Wouter J Waalewijn. “Calculating the charge of a jet”. In: *Physical Review D* 86.9 (2012), p. 094030.

[45] RD Field and Richard Phillips Feynman. “A parametrization of the properties of quark jets”. In: *Nuclear Physics B* 136.1 (1978), pp. 1–76.

[46] J.P. Berge et al. “Quark jets from antineutrino interactions (I). Net charge and factorization in the quark jets”. In: *Nuclear Physics B* 184 (1981), pp. 13–30. ISSN: 0550-3213. DOI: https://doi.org/10.1016/0550-3213(81)90207-8. URL: https://www.sciencedirect.com/science/article/pii/0550321381902078.

[47] J.P. Berge et al. “Net charge in deep inelastic antineutrino-nucleon scattering”. In: *Physics Letters B* 91.2 (1980), pp. 311–313. ISSN: 0370-2693. DOI: https://doi.org/10.1016/0370-2693(80)90456-6. URL: https://www.sciencedirect.com/science/article/pii/0370269380904566.

[48] P Allen et al. “Multiplicity distributions in neutrino-hydrogen interactions”. In: *Nucl. Phys. B* 181 (1981), pp. 385–402. DOI: 10.1016/0550-3213(81)90532-0. URL: https://cds.cern.ch/record/134175.

[49] P. Allen et al. “Charge Properties of the Hadronic System in Neutrino p and Antineutrino p Interactions”. In: *Phys. Lett. B* 112 (1982), p. 88. DOI: 10.1016/0370-2693(82)90912-1.

[50] J.P. Albanese et al. “Quark charge retention in final state hadrons from deep inelastic muon scattering”. In: *Physics Letters B* 144.3 (1984), pp. 302–308. ISSN: 0370-2693. DOI: https://doi.org/10.1016/0370-2693(84)91825-2. URL: https://www.sciencedirect.com/science/article/pii/0370269384918252.

[51] S. Barlag et al. "Charged Hadron Multiplicities in High-energy Anti-muon Neutrino n and Anti-muon Neutrino p Interactions". In: *Z. Phys. C* 11 (1982). [Erratum: Z.Phys.C 14, 281 (1982)], p. 283. DOI: 10.1007/BF01578279.

[52] R. Erickson et al. "Charge Retention in Deep-Inelastic Electroproduction". In: *Phys. Rev. Lett.* 42 (13 Mar. 1979), pp. 822–825. DOI: 10.1103/PhysRevLett.42.822. URL: https://link.aps.org/doi/10.1103/PhysRevLett.42.822.

[53] S. Acharya et al. "Exploration of jet substructure using iterative declustering in pp and Pb-Pb collisions at LHC energies". In: *Physics Letters B* 802 (Mar. 2020), p. 135227. DOI: 10.1016/j.physletb.2020.135227. URL: https://doi.org/10.1016%5C%2Fj.physletb.2020.135227.

[54] Martin Spousta and Brian Cole. "Interpreting single jet measurements in Pb+Pb collisions at the LHC". In: *The European Physical Journal C* 76.2 (Jan. 2016). DOI: 10.1140/epjc/s10052-016-3896-0. URL: https://doi.org/10.1140%5C%2Fepjc%5C%2Fs10052-016-3896-0.

[55] Shi-Yong Chen, Ben-Wei Zhang, and Enke Wang. "Jet charge in high-energy nuclear collisions". In: *Chinese Physics C* 44.2 (Jan. 2020), p. 024103. ISSN: 2058-6132. DOI: 10.1088/1674-1137/44/2/024103. URL: http://dx.doi.org/10.1088/1674-1137/44/2/024103.

[56] *Study of quark- and gluon-like jet fractions using jet charge in PbPb and pp collisions at 5.02 TeV*. Tech. rep. CMS-PAS-HIN-18-018. Geneva: CERN, 2019. URL: https://cds.cern.ch/record/2698959.

[57] Albert M Sirunyan et al. "Measurements of jet charge with dijet events in pp collisions at $\sqrt{s} = 8$ TeV. Measurements of jet charge with dijet events in pp collisions at $\sqrt{s} = 8$ TeV". In: *JHEP* 10 (2017). Replaced with the published version. Added the journal reference and DOI. All the figures and tables can be found at http://cms-results.web.cern.ch/cms-results/public-results/publications/SMP-15-003 (CMS pub-

lic pages), p. 131. DOI: 10.1007/JHEP10(2017)131. arXiv: 1706.05868. URL: https://cds.cern.ch/record/2270416.

[58] Wouter J. Waalewijn. “Calculating the charge of a jet”. In: *Physical Review D* 86.9 (Nov. 2012). DOI: 10.1103/physrevd.86.094030. URL: https://doi.org/10.1103%5C%2Fphysrevd.86.094030.

[59] Hai Tao Li and Ivan Vitev. “Jet charge modification in finite QCD matter”. In: *Physical Review D* 101.7 (Apr. 2020). DOI: 10.1103/physrevd.101.076020. URL: https://doi.org/10.1103%5C%2Fphysrevd.101.076020.

[60] Matteo Cacciari and Gavin P Salam. “Dispelling the N3 myth for the kt jet-finder”. In: *Physics Letters B* 641.1 (2006), pp. 57–61.

[61] Matteo Cacciari, Gavin P Salam, and Gregory Soyez. “The anti-kt jet clustering algorithm”. In: *Journal of High Energy Physics* 2008.04 (2008), p. 063.

[62] Stephen D Ellis and Davison E Soper. “Successive combination jet algorithm for hadron collisions”. In: *Physical Review D* 48.7 (1993), p. 3160.

[63] Yu L Dokshitzer et al. “Better jet clustering algorithms”. In: *Journal of High Energy Physics* 1997.08 (1997), p. 001.

[64] S. D. Ellis, J. Huston, and M. Toennesmann. *On Building Better Cone Jet Algorithms*. 2001. arXiv: hep-ph/0111434 `[hep-ph]`.

[65] R. Akers et al. “QCD studies using a cone based jet finding algorithm for e^+e^- collisions at LEP”. In: *Z. Phys. C* 63 (1994), pp. 197–212. DOI: 10.1007/BF01411011.

[66] Matteo Cacciari, Gavin P. Salam, and Gregory Soyez. “FastJet user manual”. In: *The European Physical Journal C* 72.3 (Mar. 2012). ISSN: 1434-6052. DOI: 10.1140/epjc/s10052-012-1896-2. URL: http://dx.doi.org/10.1140/epjc/s10052-012-1896-2.

[67] James D Bjorken. *Energy loss of energetic partons in quark-gluon plasma: possible extinction of high p_T jets in hadron-hadron collisions*. Tech. rep. FERMILAB-PUB-82-59-THY. Batavia, IL: FERMILAB, Sept. 1982. URL: http://cds.cern.ch/record/141477.

[68] David d'Enterria. "6.4 Jet quenching". In: *Landolt-Börnstein - Group I Elementary Particles, Nuclei and Atoms* (2010), pp. 471–520. ISSN: 1616-9522. DOI: 10.1007/978-3-642-01539-7_16. URL: http://dx.doi.org/10.1007/978-3-642-01539-7_16.

[69] Peter Berta et al. "Particle-level pileup subtraction for jets and jet shapes". In: *Journal of High Energy Physics* 2014.6 (2014), p. 92.

[70] *LEP design report*. Report. Copies shelved as reports in LEP, PS and SPS libraries. Geneva: CERN, 1984. URL: https://cds.cern.ch/record/102083.

[71] Stephen Myers. *The LEP Collider, from design to approval and commissioning*. John Adams' memorial lecture. Delivered at CERN, 26 Nov 1990. Geneva: CERN, 1991. DOI: 10.5170/CERN-1991-008. URL: http://cds.cern.ch/record/226776.

[72] R Alemany-Fernandez et al. "Operation and Configuration of the LHC in Run 1". In: (2013). URL: https://cds.cern.ch/record/1631030.

[73] J. T. Boyd. "LHC Run-2 and future prospects". In: *CERN Yellow Rep. School Proc.* 5 (2022). Ed. by C. Duhr and M. Mulders, p. 247. DOI: 10.23730/CYRSP-2021-005.247. arXiv: 2001.04370 `[hep-ex]`.

[74] G. Apollinari et al. "Chapter 1: High Luminosity Large Hadron Collider HL-LHC. High Luminosity Large Hadron Collider HL-LHC". In: *CERN Yellow Report* 5 (2015). 21 pages, chapter in High-Luminosity Large Hadron Collider (HL-LHC) : Preliminary Design Report, pp. 1–19. DOI: 10.5170/CERN-2015-005.1. arXiv: 1705.08830. URL: https://cds.cern.ch/record/2120673.

[75] URL: https://home.cern/science/accelerators/accelerator-complex.

[76] K. H. Reich. “The CERN Proton Synchrotron Booster”. In: *IEEE Trans. Nucl. Sci.* 16 (1969), pp. 959–961. DOI: 10.1109/TNS.1969.4325414.

[77] M Chanel. “LEIR: The low energy ion ring at CERN”. In: *Nucl. Instrum. Methods Phys. Res., A* 532 (2004), pp. 137–143. URL: https://cds.cern.ch/record/557588.

[78] “The Proton Synchrotron”. In: (2012). URL: https://cds.cern.ch/record/1997189.

[79] Geoffrey T J Arnison et al. “Experimental observation of isolated large transverse energy electrons with associated missing energy at $\sqrt{s} = 540$ GeV”. In: *Phys. Lett. B* 122 (1983), pp. 103–116. DOI: 10.5170/CERN-1983-004.123. URL: https://cds.cern.ch/record/142059.

[80] “The Super Proton Synchrotron”. In: (2012). URL: https://cds.cern.ch/record/1997188.

[81] “Radiofrequency cavities”. In: (2012). URL: https://cds.cern.ch/record/1997424.

[82] G. P. Willering et al. “Performance of CERN LHC Main Dipole Magnets on the Test Bench From 2008 to 2016”. In: *IEEE Trans. Appl. Supercond.* 27.4 (2017), p. 4002705. DOI: 10.1109/TASC.2016.2633423.

[83] The ATLAS Collaboration et al. “The ATLAS Experiment at the CERN Large Hadron Collider”. In: *Journal of Instrumentation* 3.08 (Aug. 2008), S08003–S08003. DOI: 10.1088/1748-0221/3/08/s08003. URL: https://doi.org/10.1088%5C%2F1748-0221%5C%2F3%5C%2F08%5C%2Fs08003.

[84] The CMS Collaboration et al. “The CMS experiment at the CERN LHC”. In: *Journal of Instrumentation* 3.08 (Aug. 2008), S08004–S08004. DOI: 10.1088/1748-0221/3/08/s08004. URL: https://doi.org/10.1088%5C%2F1748-0221%5C%2F3%5C%2F08%5C%2Fs08004.

[85] Georges Aad et al. “Observation of a new particle in the search for the Standard Model Higgs boson with the ATLAS detector at the LHC”. In: *Phys. Lett. B* 716 (2012), pp. 1–29. DOI: 10.1016/j.physletb.2012.08.020. arXiv: 1207.7214 `[hep-ex]`.

[86] Serguei Chatrchyan et al. “Observation of a New Boson at a Mass of 125 GeV with the CMS Experiment at the LHC”. In: *Phys. Lett. B* 716 (2012), pp. 30–61. DOI: 10.1016/j.physletb.2012.08.021. arXiv: 1207.7235 `[hep-ex]`.

[87] The LHCb Collaboration et al. “The LHCb Detector at the LHC”. In: *Journal of Instrumentation* 3.08 (Aug. 2008), S08005–S08005. DOI: 10.1088/1748-0221/3/08/s08005. URL: https://doi.org/10.1088%5C%2F1748-0221%5C%2F3%5C%2F08%5C%2Fs08005.

[88] K. Aamodt et al. “The ALICE experiment at the CERN LHC”. In: *JINST* 3 (2008), S08002. DOI: 10.1088/1748-0221/3/08/S08002.

[89] J. Alme et al. “The ALICE TPC, a large 3-dimensional tracking device with fast readout for ultra-high multiplicity events”. In: *Nuclear Instruments and Methods in Physics Research Section A: Accelerators, Spectrometers, Detectors and Associated Equipment* 622.1 (2010), pp. 316–367. ISSN: 0168-9002. DOI: https://doi.org/10.1016/j.nima.2010.04.042. URL: https://www.sciencedirect.com/science/article/pii/S0168900210008910.

[90] Antonin Maire and David Dobrigkeit Chinellato. “ALICE sub-detectors highlighted (LHC runs 1+2 // runs 3+4)”. General Photo. 2017. URL: https://cds.cern.ch/record/2302924.

[91] *ALICE Inner Tracking System (ITS): Technical Design Report*. Technical design report. ALICE. Geneva: CERN, 1999. URL: https://cds.cern.ch/record/391175.

[92] “Upgrade of the ALICE inner tracking system: Construction and commissioning”. In: (2020). URL: https://iopscience.iop.org/article/10.1088/1402-4896/aba0f7/pdf.

[93] F. Meddi. “The ALICE silicon pixel detector (SPD)”. In: *Nuclear Instruments and Methods in Physics Research Section A: Accelerators, Spectrometers, Detectors and Associated Equipment* 465.1 (2001). SPD2000, pp. 40–45. ISSN: 0168-9002. DOI: https://doi.org/10.1016/S0168-9002(01)00344-8. URL: https://www.sciencedirect.com/science/article/pii/S0168900201003448.

[94] J. Alme et al. “The ALICE TPC, a large 3-dimensional tracking device with fast readout for ultra-high multiplicity events”. In: *Nucl. Instrum. Meth. A* 622 (2010), pp. 316–367. DOI: 10.1016/j.nima.2010.04.042. arXiv: 1001.1950 `[physics.ins-det]`.

[95] G. Dellacasa et al. “ALICE: Technical design report of the time projection chamber”. In: (Jan. 2000).

[96] “The ALICE Transition Radiation Detector: Construction, operation, and performance”. In: *Nuclear Instruments and Methods in Physics Research Section A: Accelerators, Spectrometers, Detectors and Associated Equipment* 881 (2018), pp. 88–127. ISSN: 0168-9002. DOI: https://doi.org/10.1016/j.nima.2017.09.028. URL: https://www.sciencedirect.com/science/article/pii/S0168900217309981.

[97] *ALICE Time-Of-Flight system (TOF): Technical Design Report*. Technical design report. ALICE. Geneva: CERN, 2000. URL: http://cds.cern.ch/record/430132.

[98] F. Carnesecchi. “Performance of the ALICE Time-Of-Flight detector at the LHC”. In: *Journal of Instrumentation* 14.06 (June 2019), pp. C06023–C06023. DOI: 10.1088/1748-0221/14/06/c06023. URL: https://doi.org/10.1088%5C%2F1748-0221%5C%2F14%5C%2F06%5C%2Fc06023.

[99] Nicolò Jacazio. *PID performance of the ALICE-TOF detector in Run 2*. 2018. arXiv: 1809.00574 `[physics.ins-det]`.

[100] Giacomo Volpe. “The High Momentum Particle IDentification (HMPID) detector PID performance and its contribution to the ALICE physics program”. In: *Nuclear*

Instruments and Methods in Physics Research Section A: Accelerators, Spectrometers, Detectors and Associated Equipment 876 (2017). The 9th international workshop on Ring Imaging Cherenkov Detectors (RICH2016), pp. 133–136. ISSN: 0168-9002. DOI: https://doi.org/10.1016/j.nima.2017.02.037. URL: https://www.sciencedirect.com/science/article/pii/S016890021730222X.

[101] D. C. Zhou. "PHOS, the ALICE-PHOton Spectrometer". In: *J. Phys. G* 34 (2007). Ed. by Yu-Gang Ma et al., S719–S723. DOI: 10.1088/0954-3899/34/8/S81.

[102] S Evdokimov et al. "The ALICE CPV Detector". In: *KnE Energ. Phys.* 3 (2018), pp. 260–267. DOI: 10.18502/ken.v3i1.1752. URL: https://cds.cern.ch/record/2658138.

[103] A. Fantoni. "The ALICE Electromagnetic Calorimeter: EMCAL". In: *J. Phys. Conf. Ser.* 293 (2011). Ed. by Yifang Wang, p. 012043. DOI: 10.1088/1742-6596/293/1/012043.

[104] J Allen et al. *ALICE DCal: An Addendum to the EMCal Technical Design Report Di-Jet and Hadron-Jet correlation measurements in ALICE*. Tech. rep. 2010. URL: https://cds.cern.ch/record/1272952.

[105] A. Fernández et al. "ACORDE a Cosmic Ray Detector for ALICE". In: *Nucl. Instrum. Meth. A* 572 (2007). Ed. by Franco Cervelli et al., pp. 102–103. DOI: 10.1016/j.nima.2006.10.336. arXiv: physics/0606051.

[106] The ALICE collaboration. "Performance of the ALICE VZERO system". In: *Journal of Instrumentation* 8.10 (Oct. 2013), P10016. DOI: 10.1088/1748-0221/8/10/P10016. URL: https://dx.doi.org/10.1088/1748-0221/8/10/P10016.

[107] Abraham Villatoro Tello. "AD, the ALICE diffractive detector". In: *AIP Conf. Proc.* 1819.1 (2017). Ed. by Marcella Capua et al., p. 040020. DOI: 10.1063/1.4977150.

[108] C. Finck. “The muon spectrometer of the ALICE”. In: *J. Phys. Conf. Ser.* 50 (2006). Ed. by B. Sinha, J. Alam, and T. K. Nayak, pp. 397–401. DOI: 10.1088/1742-6596/50/1/056.

[109] Christian Holm Christensen et al. “The ALICE Forward Multiplicity Detector”. In: *Int. J. Mod. Phys. E* 16 (2007). Ed. by Yu-Gang Ma et al., pp. 2432–2437. DOI: 10.1142/S0218301307008057. arXiv: 0712.1117 `[nucl-ex]`.

[110] M. M. Aggarwal et al. “Characteristics of Photon Multiplicity Detector Modules in the ALICE Experiment”. In: *DAE Symp. Nucl. Phys.* 55 (2010). Ed. by R. K. Choudhury, D. C. Biswas, and K. Mahata, pp. 696–697.

[111] G. Dellacasa et al. “ALICE technical design report of the zero degree calorimeter (ZDC)”. In: (Mar. 1999).

[112] *ALICE dimuon forward spectrometer: Technical Design Report*. Technical design report. ALICE. Geneva: CERN, 1999. URL: http://cds.cern.ch/record/401974.

[113] URL: https://twiki.cern.ch/twiki/bin/viewauth/ALICE/MuonTracking.

[114] Ginés Martinez. “The Muon Spectrometer of the ALICE experiment”. In: *Nuclear Physics A* 749 (Mar. 2005), pp. 313–319. DOI: 10.1016/j.nuclphysa.2004.12.059. URL: https://doi.org/10.1016%5C%2Fj.nuclphysa.2004.12.059.

[115] Christian Finck and (forAlice Muon Spectrometer collaboration). “The Muon Spectrometer of the ALICE”. In: *Journal of Physics: Conference Series* 50.1 (Nov. 2006), p. 397. DOI: 10.1088/1742-6596/50/1/056. URL: https://dx.doi.org/10.1088/1742-6596/50/1/056.

[116] M. Krivda et al. “The ALICE Central Trigger Processor (CTP) upgrade”. In: *JINST* 11.03 (2016), p. C03051. DOI: 10.1088/1748-0221/11/03/C03051.

[117] M Krivda et al. “The ALICE trigger electronics”. In: (2007). DOI: 10.5170/CERN-2007-007.259. URL: https://cds.cern.ch/record/1091450.

[118] Christian Bierlich et al. "A comprehensive guide to the physics and usage of PYTHIA 8.3". In: (Mar. 2022). DOI: 10.21468/SciPostPhysCodeb.8. arXiv: 2203.11601 `[hep-ph]`.

[119] C. Oleari. "The POWHEG BOX". In: *Nuclear Physics B - Proceedings Supplements* 205-206 (Sept. 2010), pp. 36–41. DOI: 10.1016/j.nuclphysbps.2010.08.016. URL: https://doi.org/10.1016%5C%2Fj.nuclphysbps.2010.08.016.

[120] R Brun et al. *GEANT 3: user's guide Geant 3.10, Geant 3.11; rev. version.* Geneva: CERN, 1987. URL: https://cds.cern.ch/record/1119728.

[121] Pietro Antonioli. "Soft QCD, minimum bias and diffraction: results from ALICE". In: *EPJ Web of Conferences* 28 (2012), p. 02004. DOI: 10.1051/epjconf/20122802004. URL: https://doi.org/10.1051%5C%2Fepjconf%5C%2F20122802004.

[122] Tim Adye. "Unfolding algorithms and tests using RooUnfold". In: (2011). DOI: 10.48550/ARXIV.1105.1160. URL: https://arxiv.org/abs/1105.1160.

[123] RooUnfold Development Team. *User Guide of RooUnfold.* 2022. URL: https://gitlab.cern.ch/RooUnfold/documentation/-/blob/master/RooUnfold_user_guide.pdf.

[124] Serguei Chatrchyan et al. "Measurement of jet fragmentation in PbPb and pp collisions at $\sqrt{s_{NN}} = 2.76$ TeV". In: *Phys. Rev. C* 90 (2014). Replaced with published version. Added journal reference and DOI, p. 024908. DOI: 10.1103/PhysRevC.90.024908. arXiv: 1406.0932. URL: https://cds.cern.ch/record/1706263.

[125] R.D. Field and R.P. Feynman. "A parametrization of the properties of quark jets". In: *Nuclear Physics B* 136.1 (1978), pp. 1–76. ISSN: 0550-3213. DOI: https://doi.org/10.1016/0550-3213(78)90015-9. URL: https://www.sciencedirect.com/science/article/pii/0550321378900159.

[126] Cush MissMJ. *Diagram of the particles in the standard model.* URL: https://commons.wikimedia.org/wiki/File:Standard_Model_of_Elementary_Particles.svg.